UNIVERSITETET
I OSLO

Masteroppgave

# Mapping Flood Inundation Using Sentinel 1 and Sentinel 2 Data and the Google Earth Engine Cloud Processing Platform

**Mikael Raunig**

Geohazards and Geomechanics
60 Credits

Department of Geosciences
Faculty of Mathematics and Natural Sciences

Mikael Raunig[1]

2023

Mapping Flood Inundation Using Sentinel 1 and Sentinel 2 Data and the Google Earth Engine Cloud Processing Platform

Andreas Kääb[2]

http://www.duo.uio.no/

Trykk: Reprosentralen, Universitetet i Oslo

## Abstract

The S1 (Sentinel 1) and S2 (Sentinel 2) missions use high-resolution satellite imagery to map the land surface over large swaths. With a minimum 5-day and 6-day repeat time, imagery over earths land can be quickly obtained in S1 synthetic aperture radar imagery and S2 optical imagery. Used for a wide range of studies, the S1 and S2 missions have recently been applied to flood inundation mapping. With a global presence and high degree damage potential of a flood, studies on satellite flood mapping are important to investigate. Based on this, the thesis proposes a flood mapping method on the powerful cloud processing platform Google Earth Engine (GEE). Methodology for the thesis is presented on two cases in Norway: a rain flood in Stjørdalen and a snowmelt flood in Sunndal. The third case study was a monsoon flood in Layyah, Pakistan. Gathered data products of S1 and S2 were initially filtered to enhance and improve quality, then visualized in different polarizations in S1 and calculated in indices in S2, before a flood masking map finally was created. Additional data were gathered from a DSM (Digital Surface Model) where misclassifications from terrain could be corrected. Each study area experienced problems. Clouds were present in Stjørdalen and Layyah, concealing flooded areas in S2 imagery. Snow cover could lead to flood misclassification in Stjørdalen. Different concentrations of suspended sediments found in the floodwaters of Layyah made detection of flood difficult in some areas. Sunndal proved small scale changes in flood could be hard to detect in S1 imagery due to speckle filtering options. Despite the challenges, this study found that implementing reference stacks, pixel and elevation masking and detection type comparisons significantly improved flood detection using S1 and S2 data. The results suggest that optical and SAR-based flood inundation mapping can provide valuable support in detailing flooded areas.

## Acknowledgements

After two years of studies at UIO and the Geoscience department, I have finally reached the end of my journey here. I have met new friends in the university, and outside of school. I have learned new and interesting science from teachers and students.

First and foremost, I would like to thank my supervisor Professor Andreas Kääb. You have given me solid advice and help throughout this year. Thank you for pointing me towards the fascinating world of remote sensing.

I would also thank my family who have always encouraged and cheered for me along the way. If I ever need help with something, I know I can count on you guys.

## Acronyms

- AW3D: ALOS World 3D
- BOA: Bottom-of-atmosphere
- dB: Decibel
- EM: Electromagnetic
- EW: Extra Wide Swath
- GEE: Google Earth Engine
- IW: Interferometric Wide Swath
- L8: Landsat 8
- MSI: Multispectral Imagery
- MW: Microwave
- NIR: Near Infrared Spectrum
- NDWI: Normalized Difference Water Index
- Nm: Nanometre
- OLI: Operational Land Imager
- RCP: Representative Concentration Pathway
- SM: Strip Map
- SAR: Synthetic Aperture Radar
- SA1: Study Site 1
- SA2: Study Site 2
- SA3: Study Site 3
- SEM: Slope and Elevation Mask
- SRTM: Shuttle Radar Topography Mission
- S1: Sentinel 1
- S2: Sentinel 2
- TIR: Thermal Infrared
- TOA: Top-of-atmosphere
- WV: Wave Mode

# Contents

## List of Figures

## List of Tables

## 1. Introduction: Floods

Caused by overflowing of rivers, lakes or coastal waters, floods can cover vast areas and inflict damage to infrastructure and loss of life. Flooding is a widespread disaster type, occurring in both cold polar and warm tropical regions. Between 2000 and 2019, the most occurring natural disaster was flooding (Mizutori et al. 2020). With a reported 3254 events and affecting 1.6 billion people, flooding amounts to 44 % of all disaster events in the last two decades. Caused by a variety of events, such as snowmelt, rain, coastal flooding, ice jams and dam breaks, flooding varies in both size and duration (Roald, 2021).

In Norway, floods occur in rivers seasonally. During spring, floods caused by snowmelt are prominent in the mountainous and inner parts of Norway (Roald, 2021). Snowmelt could initiate from rain, solar radiation or warm winds where the change in temperature could happen over a small or large area. Not all floods occur seasonally, such as rain floods for example, and these are more difficult to predict. Rain floods are a common flood type. They are often categorized based on duration and intensity. While some rain floods last for weeks, the shortest floods occur over a one-day period. Caused by high-intensity precipitation, the most intense short duration floods are referred to as flash floods (Merz et al. 2003). Long rain floods can be caused by low intensity precipitation, but occurs over several days to weeks. A long rain flood can cover a large area and it will often saturate the catchment and cause serious high-cost damages. This was seen in Southern Norway in 2017, when a long rain flood caused 500 million NOK in damages (Langsholt et al. 2017). In some instances, floods are caused by both rainfall and snowmelt, a destructive combination which can lead to large floods. In Norway, large historical floods, such as Storflaumen in 1860 and Vesleofsen in 1995, were generated by rain and snowmelt. This resulted in some of the highest flood levels ever recorded in the Lågen and Glomma River (Bogen et al. 2016).

Some of the most intensive and spatially extensive floods in the world are caused by monsoons. Found in tropical regions, monsoons are seasonal weather patterns where winds and precipitation persist for a long period, during which the landscape changes completely. Regions affected by monsoons will usually have a dry season, followed by a wet season where average rainfall varies from year-to-year and could lead to large scale floods (Goswami et al. 2007). Two of the deadliest floods in the last decade were a result of heavy monsoon rains. Occurring

in Pakistan in 2010 and North India in 2013, the floods led to a death toll of 1985- and 6054 people, respectively (Mizutori et al. 2020).

Future predictions of the global hydrological cycle reveal a likely wetter and more flood prone world (Hanssen-Bauer et al. 2017). Stemming from an increase in global average temperature, the severity and frequency of future floods vary globally, based on the coming changes in greenhouse gas over the next 100 years (Alfieri et al. 2017). In Norway, future changes in flood magnitude varies regionally, with Western Norway being prone to increased flood magnitude. Eastern and Northern Norway will likely experience a decrease (Figure 1) (Hanssen-Bauer et al, 2017). These changes are based on medium (RCP 4.5) and worst case (RCP 8.5) scenarios for global average temperature increase.

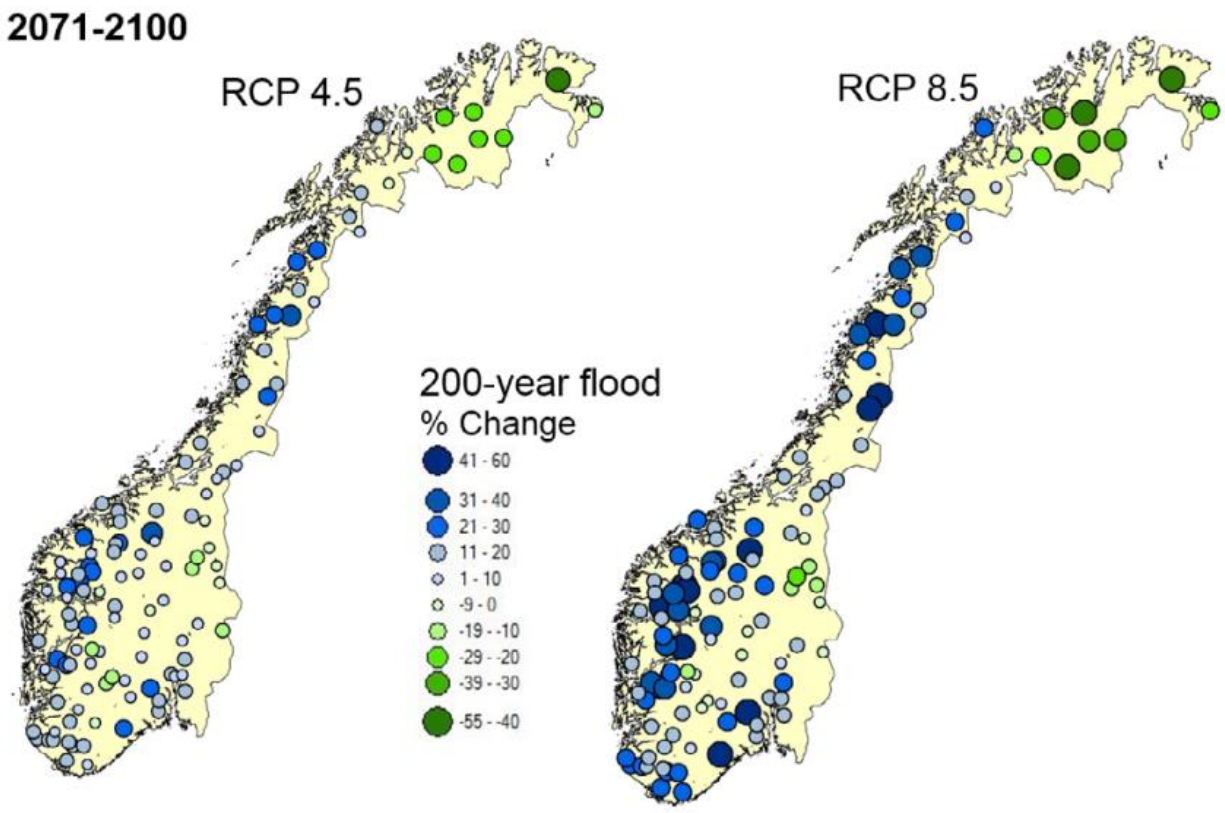


*Figure 1: Percentage change of 200- year floods in Norway for RCP 4.5 and RCP 8.5. Blue colour shows increase in flood magnitude and green colour shows a reduction. Source: Hanssen-Bauer et al, 2017.*

## 1.1 Motivation: Flood Emergency Response

Although dangerous, flooding is not described as a hazard, unless it involves loss of human lives, economic damages or other losses. Floods are most commonly hazardous around rivers and on floodplains. In China, the Yangtze River is populated by 75 million people and in Bangladesh, over 110 million people live on floodplains (Smith, 2013). In such areas, built in mitigation such as levees, drainage systems and reinforced buildings are ways to mitigate damages and loss of lives. However, mitigations are only effective to a maximum flood size, and in the event of a larger flood, the measures would lose its effect and impact on reducing hazard. Furthermore, in countries lacking financial resources, high quality mitigations are too costly. This leads to either no mitigation or poorly regulated construction practices (Smith, 2013).

Adaption is a second tool to reduce loss of life. Adaptation can be forecasting, land use planning and prepared response systems. One of the newest technologies developed for flood response, is spaceborne earth observations with satellite sensors. Satellites has worldwide coverage, and allow for aid in rescue operations by e.g., finding open roads and mapping affected infrastructure. While some of the satellites monitor the atmosphere or ocean, others such as Landsat 8 (L8), Sentinel 1 (S1), and Sentinel 2 (S2), map the land surface, making useful tools in flood monitoring. S1 is equipped with a Synthetic Aperture Radar (SAR), which is a detection system used to examine earth's surface using antennas that transmit and receive light and electromagnetic (EM) signals. The S1 radar can penetrate cloud cover and map the underlying ground. Since clouds often covers inundated land during a flood, the cloud penetrating capability of S1 makes it a great tool in flood detection. S2 and L8 on the other hand does not penetrate cloud cover, but instead rely on optic sensing. This method allows for different detection methods in visible and near infrared wavelengths, where specific ground surface features can be enhanced by use of colour and wavelength comparisons and difference enhancements.

New methods for mapping floods with satellite imagery are steadily developed where old ways of capturing images are replaced with faster and more powerful tools. A state-of-the-art method in flood mapping have been used in the powerful cloud processing platform Google Earth Engine (GEE). GEE is an open access cloud platform used to process satellite data where features, trends and changes on earth's surface and atmosphere are analysed (Gorelick et al. 2017). Being one of the world's largest archives of satellite data, GEE offers a way of quickly processing large datasets, with petabytes of data from the last forty years available.

## 1.2 Research Question

Satellite systems bring a great potential in detecting floods, and with ongoing improvements and advances in flood monitoring, this thesis investigates the effectiveness of flood detection using both S1 SAR and optical S2 images. Processing of data was done in GEE. Generated SAR and optical images of flooded areas were then compared with each other. Flooded areas were visualised and automatically detected by use of automatic flood mask method. Flood masks were produced and optimized by use of different methods, which include, digital surface model (DSM) masking, image stacks, normalized difference water index, and ratio. The visualization and detection of floods, were tested on three different study areas affected by different flood types. The study areas included a mountainous region in Norway, a valley area in Norway, and a flood prone plain in Pakistan, each with distinct terrain features and flood types that posed unique challenges to flood detection. The following research questions were asked:

1. How do different terrain features and flood types affect the accuracy of flood detection using SAR and optical images?
2. What are the strengths and limitations of flood detection using SAR and optical images in each study area?
3. How can the flood mask and optimization techniques be used to improve the accuracy of flood detection in different terrain types?

# 2. Study Areas

In this chapter, historical and descriptive background for each study area is presented. Two of the floods selected occurred in Norway; a snowmelt flood in Sunndalsføra, Møre og Romsdal and a rain flood in Stjørdalen, Trøndelag. The third flood occurred in Pakistan: a monsoon in Layyah, Punjab. Land cover descriptions in the following study areas details a 100m spatial resolution global land cover map from Copernicus, included for each study area (Buchhorn et al. 2020).

## 2.1 Study Area 1: The 2022 Gyda Flood in Stjørdal

From January 12th - 14th, 2022, parts of the Norwegian counties Innlandet, Vestland, Møre og Romsdal, and Trøndelag were affected by a devastating weather event known as Gyda. Caused by warm and moist air transported from the Norwegian sea, the event brought record-breaking rainfall to the four counties, resulting in flooding over large areas. Using the international standard for weather warning, CAP (Common Alerting Protocol), the Norwegian meteorological institute sent out yellow and orange warnings days in advance. However, on the 11th of January, the warning level was increased to the highest, red, indicating extreme weather (Skjerdal et al. 2022). The weather was then given the nickname "Gyda". During the event, a total of 27 research stations broke the previous record for 1-day precipitation and Møre og Romsdal broke the county record with 153,1mm that was held since 1907 (Skjerdal et al. 2022). The event resulted in flooding, snow avalanches, and rock and soil slides. The insurance company Gjensidige estimated the damages to be around 100 million NOK (Roaldseth, 2022). As water levels increased, streets and buildings became overflooded. In some areas, people were unable to escape by car and had to be rescued by helicopter or boat. Over 70 roads were

closed or destroyed by the water. Stjørdalen was one of the areas greatly affected by the flooding (figure 2).

*Figure 2: Gyda flood. A flooded road in Stjørdalen. Source: Hofstad, (2022)*

SA1 (Study Site 1) Stjørdal, is a municipality in Trøndelag (Figures 3A-B). Surrounded by forest and agricultural land (Figure 3C), the Stjørdal river runs through the Stjørdal Valley with a city situated on the west side of the valley next to the river outlet by the Trondheim Fjord (NVE Atlas, 2022). According to Dagbladet, a total of 50 people were evacuated in Stjørdal due to the flood (Dalen et al. 2022). One couple had to be rescued by boat, as the river surrounded their house. Reported by NRK, the 55km long river had buildings and cars floating downstream (Svendsen, 2022).

After January 14$^{th}$, rainfall ended, and the Norwegian Nature Damage Agency had over 2000 reports of damages related to the flooding. In the aftermath of the event, flooding was considered the main cause of the damages, accounting for 60 % (Pettersen, 2022). Meteorologists concluded that the rainfall was caused by an atmospheric river from the Atlantic

Ocean that brought warm and moist air (Skjerdal et al, 2022). Also known as a moisture conveyor belt, an atmospheric river can bring extreme precipitation in mountainous areas such as Norway (Stohl et al. 2008). Rainfall in Western Norway usually form from orographic precipitation. However, in winter, the air is cold enough that some of the precipitation is in the form of snow. Temperatures on Jan 12$^{th}$ were too warm and therefore led to precipitation in the form of rainfall. Atmospheric rivers are connected to 79 % of extreme precipitation events in South-Western Norway and similar events are possible in the future (Michel et al. 2021). Considering the damages this flood caused, mitigation for extreme rainfall events in the future is important.

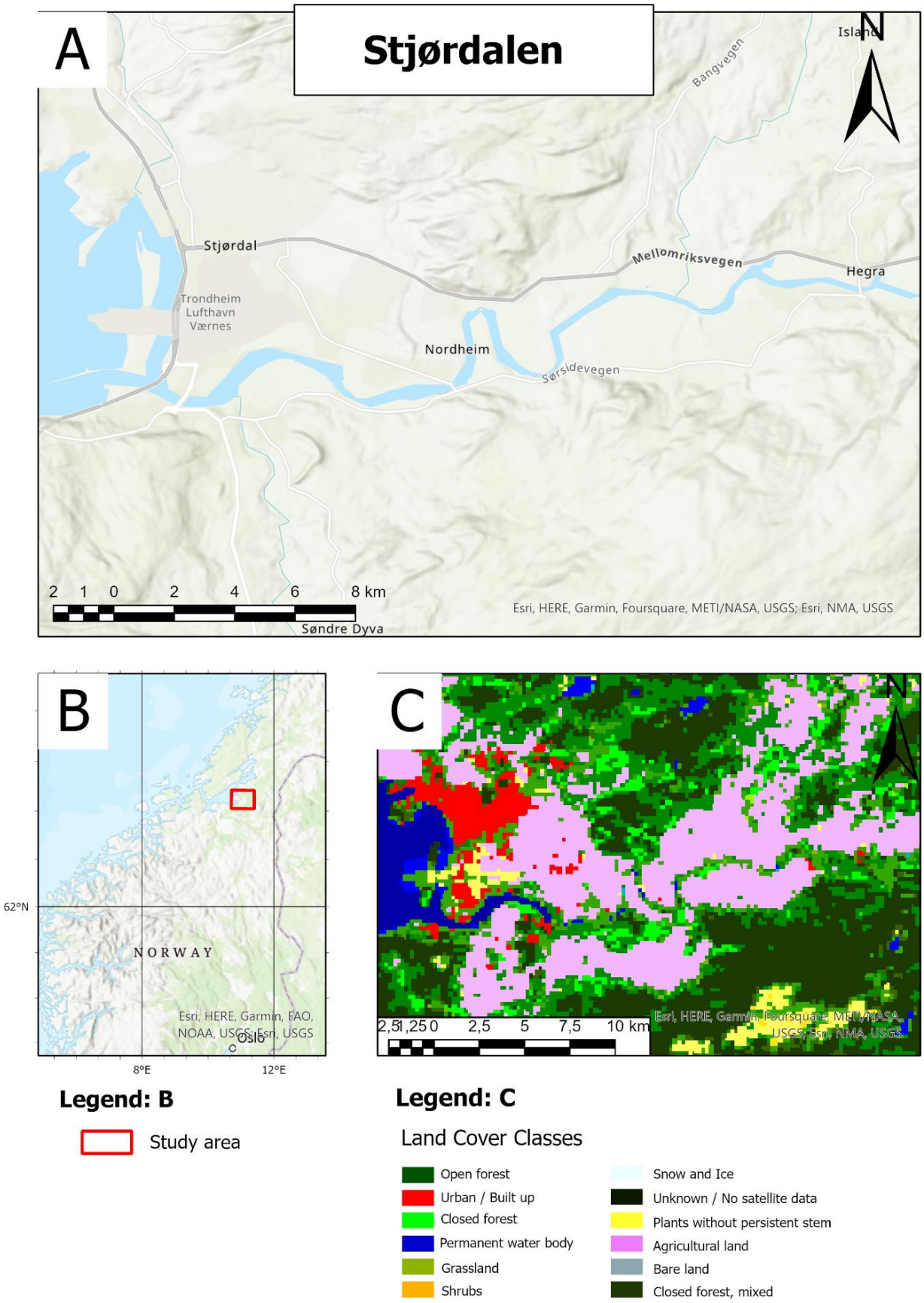


*Figure 3. Study area 1: Stjørdalen. A: 1:150 000 projection of the study area. B: The red square indicates location of study area. C: Land Cover Map by Copernicus Global Land Cover Data with 1:250 000 projection.*

## 2.2 Study Area 2: Snowmelt Flood in Sunndal, June 2022.

Taking place between June 25th and July 1st, 2022, in an intense heatwave spanning over parts of Western, Southern, and inland Norway, rivers and streams in mountainous areas experienced high discharge levels. As a result of melting snow, this flood occurred first in mountain streams, before it caused further flooding downstream into large rivers. Some of the rivers affected were Rauma, Driva, and Stryneelva (Varsom, 2022). The result of this event was erosion in streams and rivers, and flooding in smaller urban areas, However it was at a much smaller scale than initially expected due to low amounts of rain over the melting period.

Initially, flood warnings were sent out at red level. However, this was readjusted to orange level on June 28th for several areas, including Sunndal. Flooding was predicted already on June 10th by Varsom, as snow in Northern and North Western Norway had not melted yet (Stavang et al. 2022) (Figure 4).

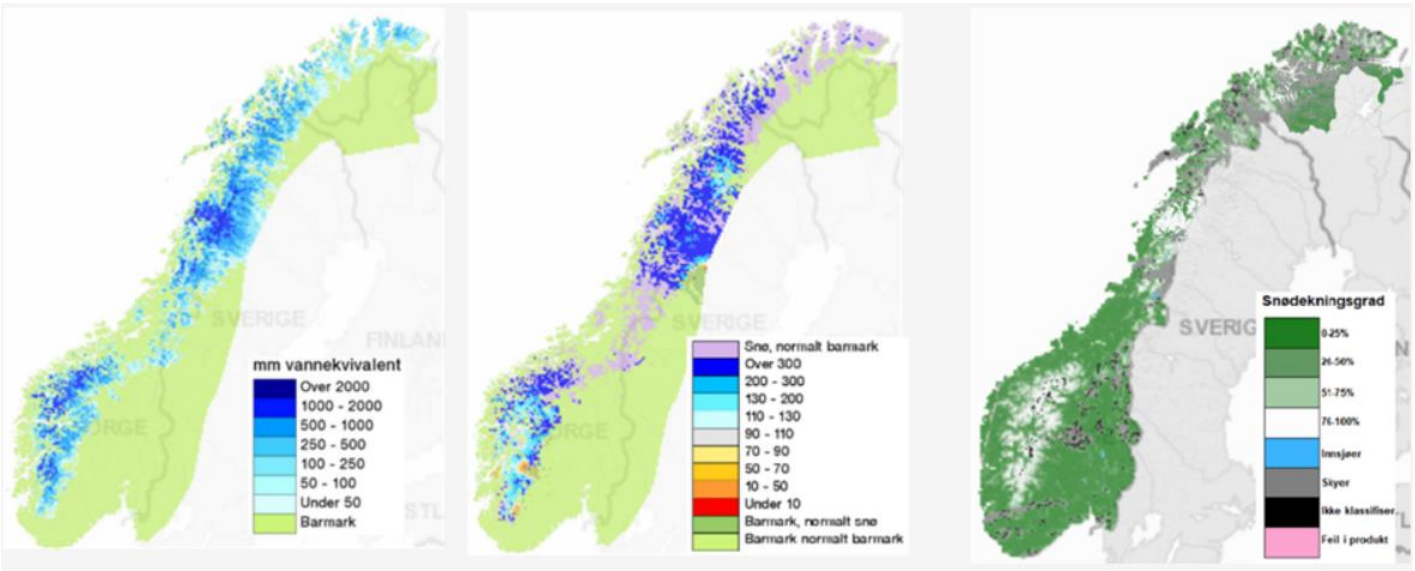


*Figure 4:* Remaining June snowpack. *From left to right: (left) remaining snow in mm water equivalent, (middle) percentage of normal snow mm and (right) satellite pictures June 6th and 8th showing degree of snow cover. Source: Stavang et al, 2022*

Situated in Sunndal, Møre and Romsdal county, SA2 (Study Area 2) resulted in flooding due to the snowmelt (Figure 5). Sunndal is recognized by its steep and long valley. With a total length of 137,8km, the Driva river runs through the valley (NVE Atlas, 2022). The area is enveloped by high mountaintops reaching a height of 1880 m.a.s.l. on the Storkalkinn

mountaintop south of the river, and Hofsnebba at 1554 m.a.s.l north of the river. The terrain at the highest peaks is covered in snow during winter and melts in the summer months.

Locals in Sunndalsøra were warned beforehand and prepared by moving valuable goods such as haybales, cars, and furniture to safe areas. The municipality checked that critical points of the river such as smaller streams and culverts, were open. They also tested drainage pumps (Bondhus, 2022).

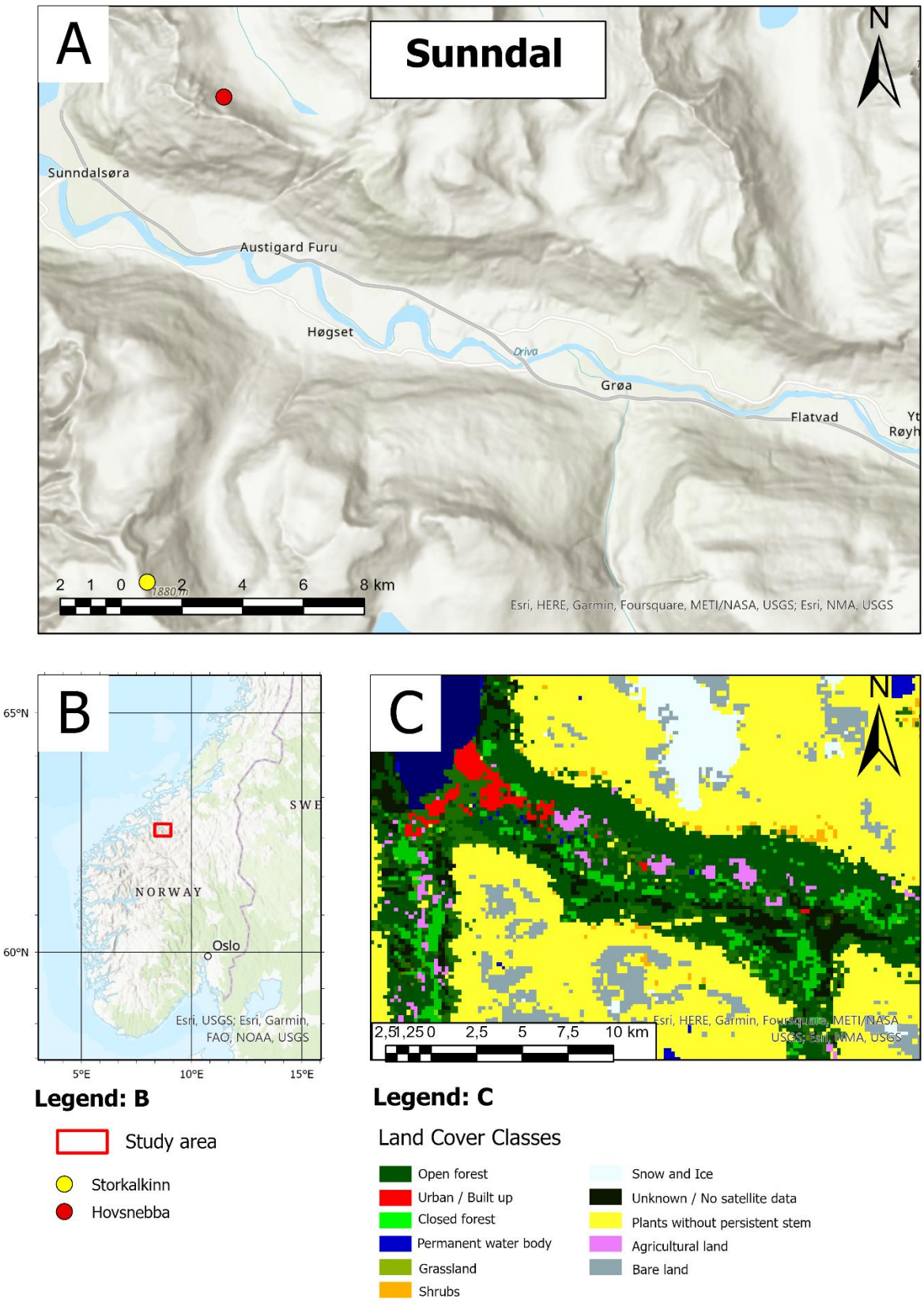


*Figure 5. Study area 2, Sunndal: A: 1:150 000 projection of the study area. B: The red square indicates location of study area. C: Land Cover Map by Copernicus Global Land Cover Data.*

## 2.3 Study Area 3: Layyah, Pakistan

Described as the worst flood in the country's history, the 2022 Pakistan flood was the world's deadliest flood since the 2020 South Asia flood. Taking place between June and October 2022, the flooding was caused by the yearly monsoon rainfall and melting glaciers from the Himalayan mountains. While the monsoon rainfall is a yearly occurrence in the country, some areas received more than 784 % above the average rainfall, and national rainfall was 243 % of the average (PMD, 2022). In addition to the water received from meltwater, the result of the flood was more than 3.2 trillion Rs or 14.9 billion USD in total damages and a death toll of over 1600 people (USAID, 2022). Major river systems increased in size, extending into cities, farmlands, and lakes (Figure 6). Roads, bridges, and houses were destroyed by erosion and floating debris, causing difficulties for rescue operators to mobilize. In the aftermath of the flood, contaminated and stagnant water lead to lack of drinking water and caused a spread of diseases, including malaria and dengue.

*Figure 6: Aerial flood photo. The 2022 Pakistan flood in the province of Balochistan showing inundated houses and roads. Photo: Fida Hussain, (Guardian, 2022).*

Although around 160 million USD was allocated to the flood victims by Pakistan's social safety net BISP, the rescue operations conducted by the government were described as poor (AFP, 2022). With pledges of food and shelter, help was received too late and in small scope.

Government officials were reported to hoard aid for themselves, and trucks carrying supplies for flood victims were looted.

Countries, organizations, banks and companies helped by donating money, assistance packages, relief materials, and air bridges. The immediate aid reached approximately 500 million USD, provided by the World Bank, the World Food Programme, the Asian Development Bank, and UKAid. Federal cabinet members in Pakistan also donated a 1-month salary each in aid. In a statement from the Prime Minister of Pakistan, the flooding was referred to as a "climate catastrophe", and "Pakistan has to face the consequences of other countries emissions" (Tan, 2022) (Baloch et al. 2022). The UN secretary and Prime Minister of Fiji gave their concerns regarding climate change and the future of Pakistan (AA, 2022; Clarke et al. 2022).

A particularly affected area from the flood was SA3 (Study *A*rea 3) in Layyah, Pakistan, located in the south end of the province Punjab (Figure 7). In SA3, the Indus River extends on the west-side of the city, and *it* flows from *N*orth Pakistan to *S*outh, where it eventually ends up in the Arabian Sea at the Indus River delta. The 3180 km long river has its source in western Tibet where it is fed from mountain springs and glaciers, before it flows through the plains of Pakistan (Shreshta et al. 2015). On the west side of the study site lies Tiyar mountain, 798 m.a.sl with little or no vegetation in the surrounding areas. Despite being arid land, the study site is covered in agricultural land (*F*igure 7 C), where crops are fed by the southwest monsoon period (Ahmed et al. 2018). During the flood, the Indus River extended over agricultural and urban land with some areas reported by the local newspaper to have extended across 80 km (Hussain, 2022).

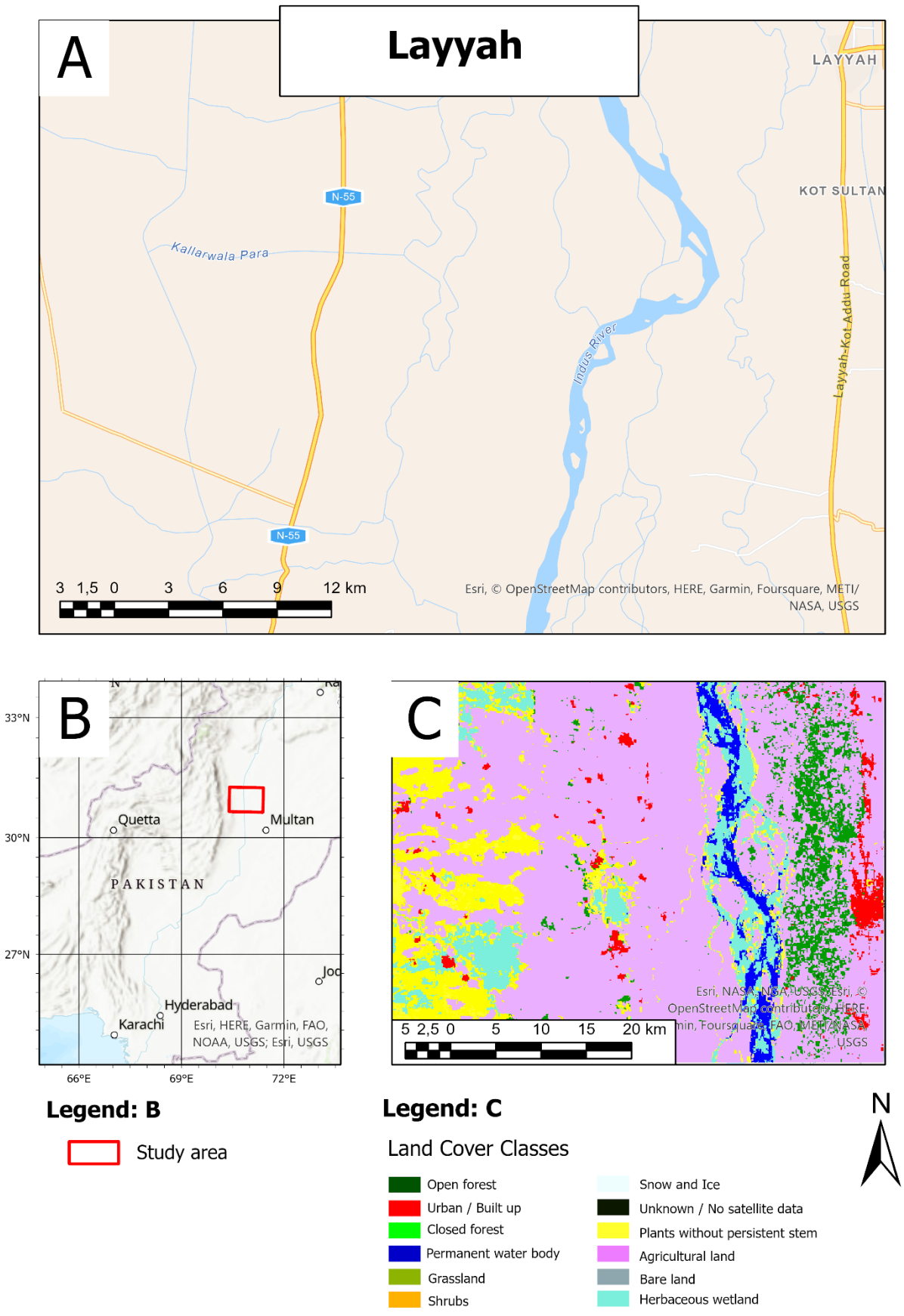


*Figure 7. Study area 3: Layyah. A: 1:250 000 projection of the study area. B: The red square indicates location of study area. C: Land Cover Map by Copernicus Global Land Cover Data with 1:500 000 projection.*

## 3. Theoretical Backgrounds

Previous studies on the detection of floods and water bodies with GEE have been done with different approaches. Liu et al. (2018) developed an emergency response system for floods, where different stages of a flood could be presented. Data from each flood stage was gathered from weather and forecasting data, disaster alerts, reservoir stations, high resolution UAV photos, and optical and SAR imagery. Moharrami et al. (2021) provided a flood mapping method by the use of SAR imagery time series with a computed threshold using an algorithm named Otsu. Some studies have analysed inundation over larger areas, such as monsoon floods in Bangladesh and Kerala, India (Singha et al. 2020; Tiwari et al. 2020). In this paper, two methods for flood detection in GEE are presented: Flood detection with SAR and flood detection with optical imagery.

### 3.1 Synthetic Aperture Radar

Mounted on a moving platform, the Synthetic Aperture Radar gets its name from creating a virtual aperture or synthetic aperture by moving and simultaneously focusing its sensor over a target area (Moreira et al. 2013). With this method, high resolution images over large areas can be created without relying on a large antenna (Liang et al. 2021). The antennas can be mounted on airplanes (airborne) or satellites (spaceborne), moving over terrain while scanning the ground. Image width varies from up to 20 km on airplanes to 500 km for satellite sensors. The radar antenna is side-looking, with a set altitude and viewing geometry. Figure 8 shows the standard viewing geometry of SAR as the platform is moving over the ground. The flight path direction is called azimuth, and perpendicular to the azimuth is the slant range (Moreira et al. 2013). The swath width gives the width or length in the perpendicular direction (slant range) of the azimuth (Liang et al. 2021). With a defined length given by the data take time, in addition to the swath width, one image is captured. The nadir track follows the azimuth directly underneath the sensor. While scanning the ground, the platform is moving at a near constant velocity (Fouad et al. 2022).

SAR is an active radar, which means that it produces and transmits its own EM energy, where the signal is sent and reflected from a surface (Moser et al. 2018). The wavelength range of SAR signal is in the microwave spectrum (MW) (Figure 9). Ranging from <1 cm to 1 m, the wavelength of the MW spectrum can be divided into different bands. A band is defined as a wavelength segment or range withing the EM spectrum (Wasser, 2017). MW is invisible to the eye and grants some advantages in comparison to optical remote sensing, such as: cloud cover penetration and night-time ground detection (Moharrami et al. 2021; Kääb, 2004). Some bands

are within ranges where the signal can penetrate tree canopies. Consequently, a wide range of bands are used in different SAR sensors. Each sensor expresses good quality in sensing where its band is proven useful. Band K, X, C, S and L is used by different SAR sensors, where the shortest wavelength is within band K with a wavelength range of 0.75 to 2.4 cm and the longest wavelengths are found in band P with 30-100 cm (du Preez et al. 2016; Lucas et al. 2007). A study by Chiu et al. (2000) found that low frequency SAR bands, such as L band or lower can penetrate the canopy of short branching vegetation. This study focused on backscatter effects on soybean plants. Higher frequency bands such as the C band, were found to scatter at the canopy. Similar results were found in a study by Landuyt et al. (2020). In this study, it was possible to map flooding under sparsely vegetated areas using C band.

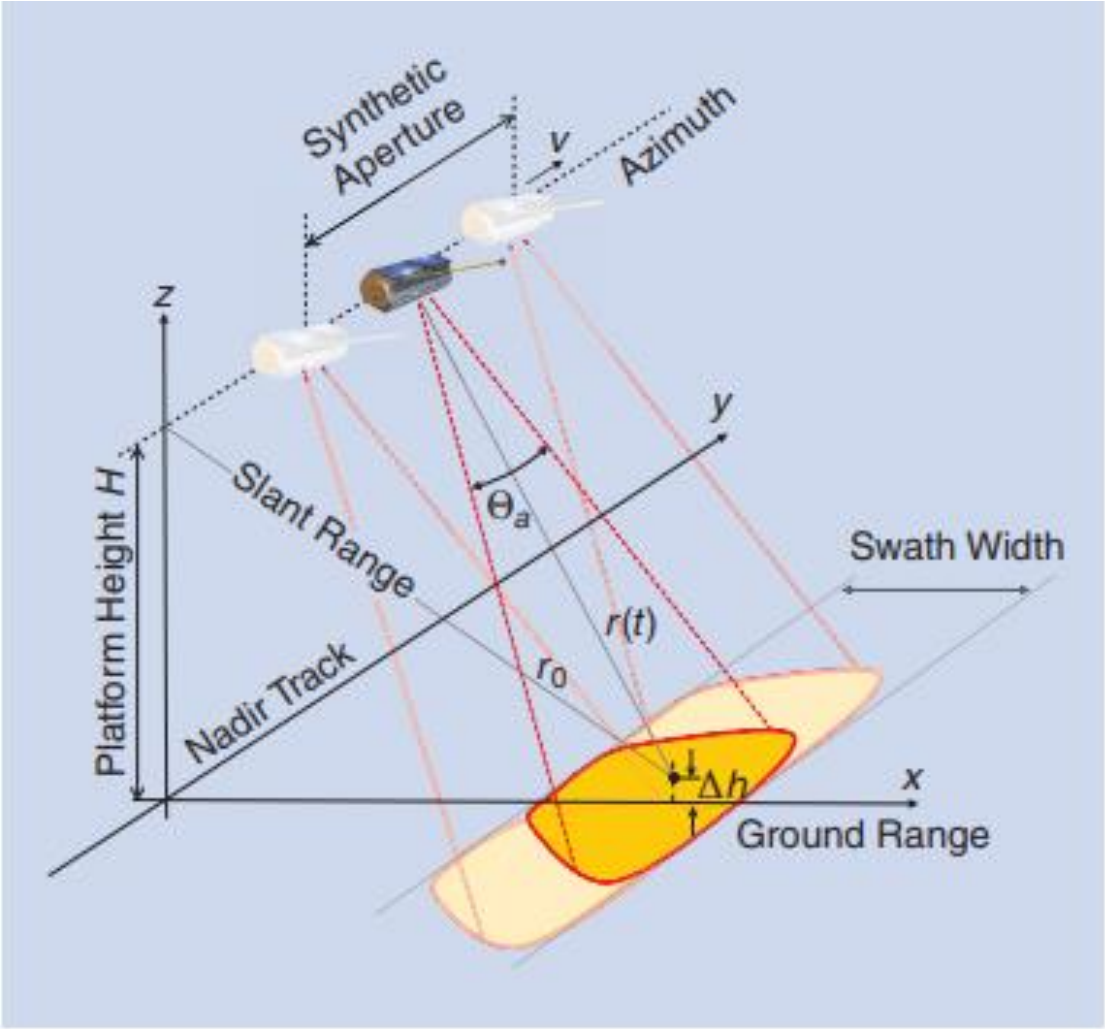


*Figure 8: SAR imaging geometry. Common imaging geometry of a SAR sensor on a moving platform. Source: (Moreira et al. 2013).*

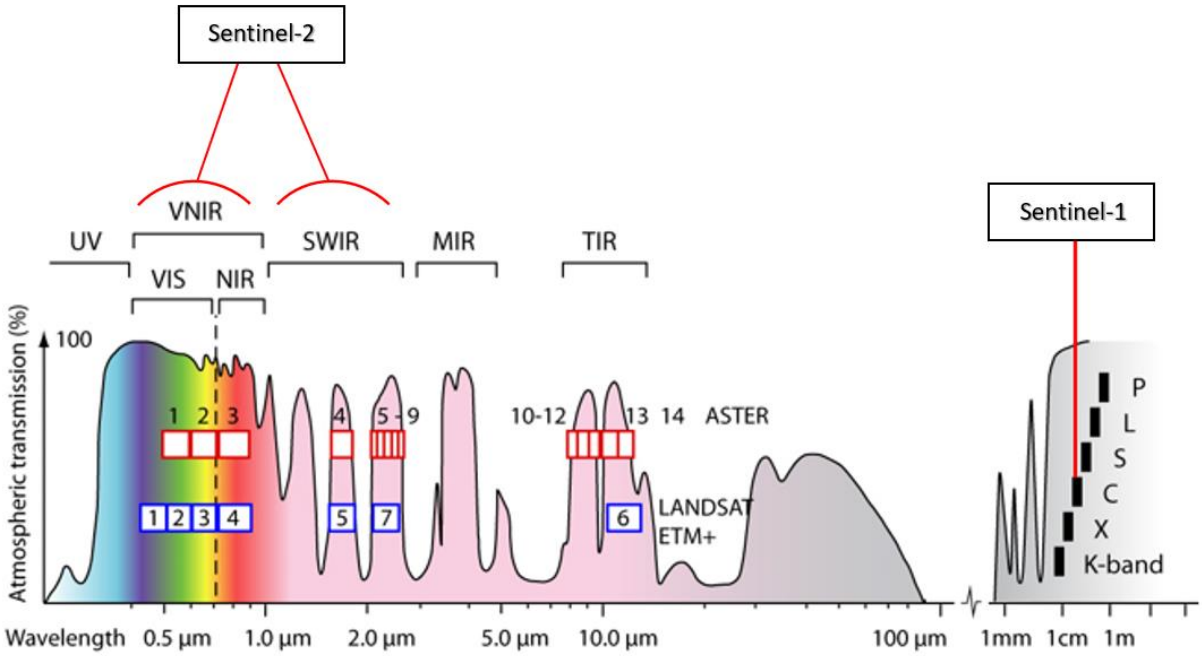


*Figure 9: Wavelengths of the EM Spectrum: From left to right: The Ultraviolet, Visible, Near and Shortwave Infrared, TIR and MW spectrum. Blue, red and dark squares show different bands used in different sensors. Source: (Kääb et al. 2002).*

When a signal is sent from the antenna, the transmitted signal is scattered from the ground, and some energy is reflected back to the receiver. Known as backscatter, the intensity will vary based on the roughness and permittivity of the reflected ground object in addition to the wavelength of the signal (Ferro-Famil, 2016). Features such as trees, cornfields, buildings, water, and mountains have different geometry from each other. They will therefore reflect different amounts of backscatter when exposed to an EM signal. A water body and other flat objects result in low backscatter while rougher surface will scatter more of the signal (Tarpanelli et al. 2022). Consequently, the variation of backscatter on the land surface is used to interpret and differentiate features on land and water.

The strength of backscatter is measured in $\sigma^{\circ}$(sigma-nought), and backscatter per unit area is measured in decibels dB (Hall, 1996). Backscatter intensity can be visualized with a brightness/darkness map, where light areas show high backscatter and dark areas show low backscatter. In addition to wavelength and terrain type, $\sigma^{\circ}$ will vary based on incidence angle, acquisition date and polarization (Manjusree et al. 2012), where polarization is defined as the orientation of the transmitted and received signal. It is divided into two parts: vertical and horizontal signal paths. Polarization of the signal can be classified into four parts:

1. VV: Vertical transmission and vertical reception
2. HH: Horizontal transmission and horizontal reception
3. VH: Vertical transmission and horizontal reception
4. HV: Horizontal transmission and vertical reception

Cross polarization is a channel type where the transmitter and receiver have different polarizations. VH and HV are referred to as cross-polarized (Strzelczyk et al. 2021). Co-polarizations are thus the opposite, where both the transmitting and receiving signal have the same orientation. VV and HH are referred to as co-polarized. Since σ˚ varies with polarization, imagery will vary based on the polarization chosen for detection. Colour composites can be created from SAR data by choosing a combination of polarizations.

Problems arise with SAR imagery when the signals sent from the satellite sensor meets tall structures, such as mountains. As the sensor with side-looking geometry sends out signals at an angle relative to the ground, mountain slopes facing away from the signal will not receive it and appear as shadows (Bayanudin et al. 2016). The front facing side of the mountain experiences a different problem, where the top and bottom parts receive signals at different intervals. The resulting effect is known as foreshortening, and it causes a distortion in the imagery, where slopes appear as compressed and bright regions. In some cases, the signals on the top part of the mountain are received before the bottom part. This effect is called layover and the mountain top appears to change position (Bayanudin et al. 2016).

### 3.2 Flood Detection With SAR

Interactions between signal and ground structures can be described by the backscatter intensity it produces and the path the signal takes because of the interaction (Figure 10). Signals bouncing off a target one time is called single bounce or single-polarization (Bai et al. 2017). Single bounce can vary in backscatter strength, depending on the angle of the ground structure and signal. If the terrain is perpendicular to the signal path, it will induce a strong signal. Also known as direct backscatter, this mechanism is commonly found on flat surfaces such as mountain slopes that are oriented perpendicular to the signal path. Water bodies and roads are also flat, but they are oriented at an angle where most of the signal is reflected away from the sensor. This mechanism is called forward scattering, and it results in a weak signal, where little to no signal is reflected at the sensor (Strzelczyk et al. 2021). Diffuse scattering occurs when the signal hits rough terrain, causing a scatter in multiple directions. Parts of the signal is reflected to the sensor, and part is reflected away (Figures 10 G-H). Diffuse scattering gives a stronger signal than forward scattering and a weaker signal than direct scattering. A signal can

also bounce on multiple objects, such as ground to tree or ground to building. This mechanism is called double bounce and results in a strong return signal (Figure 10C). Volume scattering happens if a radar signal hits a tree canopy, where branches and twigs causes the signal to scatter in multiple directions (Figure 10B) (Moghaddam et al. 1995).

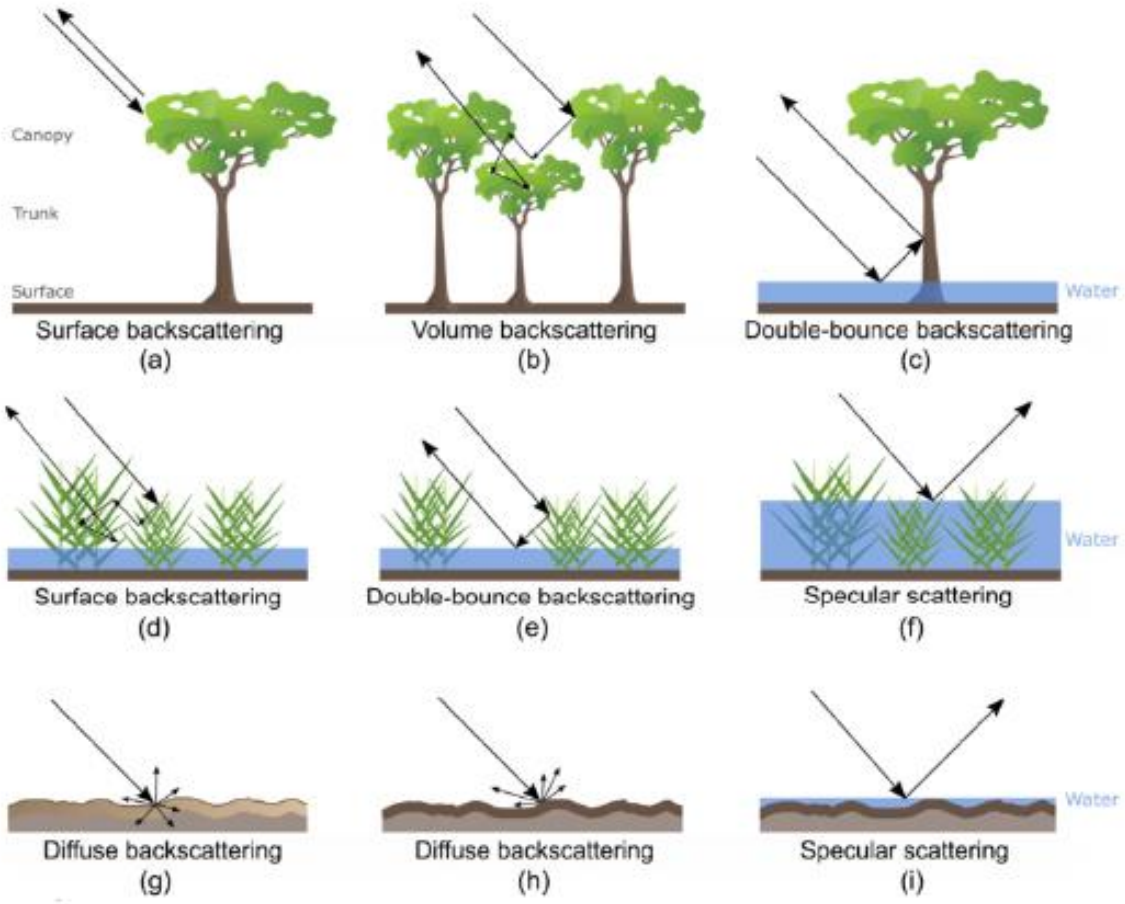


*Figure 10: Backscatter mechanism of different surfaces. Source: Ottinger et al, 2020*

Even though the theoretical background for backscatter-ground interactions is recognized, mapping correct surface features using backscatter values is not easy. It requires advanced models with many input parameters (Freeman et al. 1998). Studies have shown that factors such as tree branch size, stem size and height could determine if a signal would successfully create a double bounce backscatter (Moghaddam et al. 1995). In areas where water surfaces occur under and around vegetation, backscatter in different bands (X, C, L etc.) would generally increase (Huang et al. 2022). Changes in water level could also change the backscatter mechanism (Figures 10D, E, F and I).

Turbidity and wind could be determining factors in the backscatter value for open water features (Wangchuk et al. 2022; Meena et al. 2021). As more waves and stirred water gives rougher

surfaces than calmer water, similar backscatter changes as seen between Figures 10H and 10I could occur. Meena et al. (2021) found that as water gets more turbulent, waves created in rivers results in higher backscatter return signals. The study also found that sediments and other rough surfaces in the water attributed to higher return signals.

In a study on mountain snow sensing with MW, backscatter effects on snow varied depending on incidence angle of the satellite, polarization, and on snowpack conditions, such as snow water content, permeability, and snow depth (Floricioiu et al. 2001). Surface scattering between ground surface and dry snow are the main contributing factor of backscatter in V, L, and C band. In X band however, at higher incidence angles, volume scattering is the main backscatter factor. In C band, snow-ground surface backscatter is the main contributor, but decrease if incidence angle increases and volume scattering increase (Floricioiu et al. 2001).

These effects would also vary based on homogeneity and depth of the snowpack, as snowpack layers would reflect part of the signal. As the dry snowpack depth increased, the signal would experience attenuation and volume scattering. When the snowpack got wetter, it experienced less volume scattering and more surface scattering at the boundary between the top layer and the air. The study also found that as the incidence angle increased the main contributor for backscatter changed. In C band, the main contributing backscatter mechanism was ground surface – snow, but as the incidence angle increased, this mechanism decreased while volume scattering increased.

### 3.3 Passive Multispectral Instrument

Consisting of bands commonly in the visible and near infrared, passive MSI (multispectral optical imagery) is obtained by using a sensor that relies on the reflectivity of the sun light on the land surface to detect features on the ground (Nicolis et al. 2021). Some MSI sensors, such as Landsat 8 includes other bands, such as SWIR (short wave infrared) and TIR (thermal infrared) (Acharya et al. 2015). Passive sensors can be problematic, as this detection method can only get images in daytime and clear sky conditions. S2 is unable to view land underneath cloud cover. Despite these limitations, some passive sensors, such as S2 has good image quality and high swath widths up to 290 km (Spoto et al. 2012). Sometimes confused with Hyperspectral Imaging, MSI measures spaced bands instead of continuous bands (Hagen et al. 2013). A well-known MSI visualization is the RGB colour composite, which is often used in

digital work, graphic design, and conventional photography. The RGB uses the red, green, and blue bands in the visible spectrum (Nicolis et al. 2021). With a RGB colour image, one can separate simple landforms and features from each other, such as water, forests, agriculture and buildings. To get more detailed or specifically highlight certain features in the terrain, indexes or formulas can be used such as band ratio, band difference, or normalized difference index.

### 3.4 Flood Detection With MSI

Normalized Difference Water Index (NDWI) is an index used with MSI imagery, where the goal is to visualise water surfaces. The formula for NDWI was derived by McFeeters. (1996), where green wavelength of the visible spectrum and near infrared spectrum (NIR) is used to highlight water surfaces on the ground:

$$(Green - NIR)/(Green + NIR) \qquad \textit{Formula 1.}$$

This formula considers the reflectance changes on water molecules interacting with sunlight. It is used to set a threshold where water surfaces and flood water surfaces can be highlighted (Gao, 1996; Tarpanelli et al. 2022). Several indexes exist that highlight different features of the surface such as:

- Normalized Difference Turbidity Index (NDTI) which highlights turbid water
- Normalized Difference Snow Index (NDSI) which highlights snow
- Normalized Difference Vegetation Index (NDVI) which highlights green area density (Hofmeister et al. 2022; Schinasi et al. 2018).

A newer version of the NDWI was suggested by (Xu, 2006), where the NIR spectral band is changed with the mid infrared band (MIR). Named the “modified NDWI” or “MNDWI”, this version is better suited for distinguishing built up land among water features.

Landuyt et al. (2020) investigated floods in vegetated areas with S1 and S2 optical imagery. By using a combination of visible, near infrared, and short-wave infrared bands, the study tried to differentiate between dry land, permanent water, open flooding, and flooded vegetation. The study struggled to detect floods under dense vegetation, but detection in less vegetated areas were possible. In addition to dense vegetation, water quality also affects detection methods of floods. NDWI detects water bodies as values usually over 0 and dry land as negative values. However, in rivers with muddy water, values could change considerably and be detected as negative values (Xu, 2006).

Similarly to SAR, turbidity would alter visualization and detection of water, and experience problems, such as reflection changes, due to suspended sediments. Based on concentrations and turbulence in the water, suspended sediments in water vary and give rivers a wide variety of reflective values (Figure 11) (Meena et al. 2021). A combination of clay, silt, and sand, in addition to organic matter changes the water colour (Klemas et al. 2014). Studies have also found that shallow water can be challenging in flood detection (Singh et al. 2007; Jain et al. 2020). Water mapping methods, such as the NDWI proposed by McFeeters. (1996), can misclassify shallow water as soil or land surface (Jain et al, 2020). Examples of changing river colours is seen in deltas, rivers, and tidal flats. Figure 11 shows changing water colour in two different areas; 11A and 11C display Bay of Fundy, 11B and 11D display Bermuda. The high-water level difference in Bay of Fundy causes water to go from dark blue deep water to shallow purple water (NASA, 2006). Figures 11B and 11D shows changing colour in the water, due to suspended sediments from Hurricane Gonzalo.

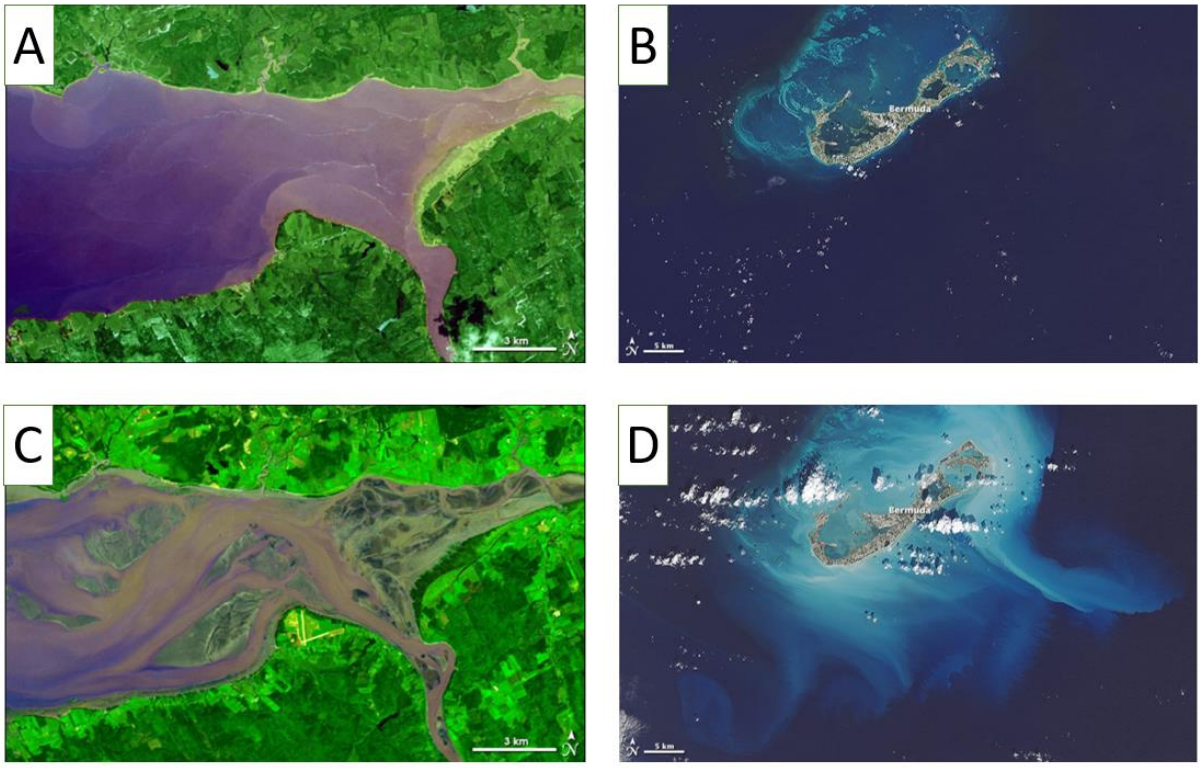


*Figure 11: Imagery of different sediment-filled waters. A and C display Bay of Fundy captured with Advanced Spaceborne Thermal Emission and Reflection Radiometer (ASTER). B and D display Bermuda captured with L8 imagery. Source: (NASA, 2006) and (NASA, 2014).*

Rivers that experience monsoon flood are often turbulent. As the monsoon increases the discharge, a peak discharge is reached within a timeframe and subsequently decrease after peak is reached. When the discharge of the river changes, grain transport rate also changes. As the

suspended sediment concentration changes throughout the river, so does the reflective values of the river (Singh et al. 2007). If reflective values change considerably, setting a standard threshold value for NDWI or other detection methods could be difficult.

Bazilova et al. (2022) takes on the difficulty of mapping glacial lakes. The study proposed a method for detecting water bodies in snow covered areas. Since similarities between water and snow cover could affect the quality of the water mapping, approaches were taken to enhance the differences between snow and water in optic imagery. This was done in two ways: using band ratio imagery instead of NDWI imagery, and by using minimum and maximum reflection values of a stacked annual time series. The study found that using ratio increased the difference between classes, but it increased the noise of the imagery. Reference stacks helped remove seasonal snow cover and ice on lakes, but they reduced temporal resolution. The band ratio proposed by Bazilova et al. (2022) was as follows:

$$R_{water} = \frac{green}{nir} \qquad \textit{Formula 2.}$$

# 4. Data Access

This chapter presents the different datasets and API used to investigate and further calculate flood detection of each subarea.

## 4.1 Google Earth Engine

In this paper, processing, creation and visualisation of satellite data was done in GEE. Processing the public data was done in this study with JavaScript API. Coding in the JavaScript environment allows the user to calculate, filter, and display different parts of the data, such as images or entire image collections. The calculations are done over Google Earth Engine servers, which allows the user to avoid time consuming computations (Gorelick et al. 2017). After the images were processed, they were downloaded to Google Drive. The layout for each image was then created in ArcGIS Pro, where legend, north arrow, reference grid, and scale bar could be added.

## 4.2 Copernicus Mission: Sentinel 1

The first mission was called Sentinel 1 (S1), and it launched in 2014 with the intent to monitor earths land, sea ice, rivers, lakes and emergency management (Fletcher, 2012). Since the launch of S1, the sentinel fleet has upgraded to several satellites, including: Sentinel 1, 2, 3, 4, 5p, 5, and 6. Further missions are being prepared for the future. Each mission concentrates on a specific part of earth's environment and use a minimum of two satellites each.

In this study, SAR imagery is obtained from S1 data on GEE. S1 consists of two satellites: the currently working S1a, and S1b which decommissioned in 2022. Each satellite has a 12-day orbit time around earth, but imagery of areas can be further reduced to 6 days with the combination of both satellite sensors. The Synthetic Aperture Radar mounted on S1 transmits and receives its own C-band signal to detect surface changes (Fletcher, 2012). The C-band has a wavelength range of 4 to 8 cm, making up part of the MW range (Peebles et al. 1998). The S1 C-band has different polarization modes. Either single polarization (VV or HH) or dual polarization (VV+VH or HH+HV), with the main mode in (VV and VH) (Table 1) (Torres et al. 2012). Thus, S1 imagery can be acquired in either co-polarized or cross-polarized mode.

| Name | Description | Resolution pixel size | Units dB (decibel) |
|---|---|---|---|
| VV | Co-polarization. Vertical transmission, vertical receiver | 10 m | dB |
| VH | Cross polarization. Vertical transmission, horizontal receiver | 10 m | dB |
| HH | Co-polarization. Horizontal transmission, horizontal receiver | 10 m | dB |
| HV | Cross- polarization. Horizontal transmission, vertical receiver | 10 m | dB |

*Table 1: Polarizations of S1: The different names and descriptions of each polarization available for S1.*

S1 uses four different acquisition modes: Interferometric Wide Swath (IW), Extra Wide Swath (EW), Stripmap (SM), and Wave (WV). The acquisition modes have different resolutions, swath widths, incidence angles, and polarization options. The most applied acquisition over land is IW, which has a swath width of 250km, spatial resolution of 5x2 0m and dual (HH+HV, VV+VH) polarizations (Prats-Iraola et al. 2015; Mullissa et al. 2021). Land surface scanned in IW uses a technique named Terrain Observation with Progressive Scans SAR (TOPSAR). With TOPSAR processing, the antenna is rotating forwards and backwards along track, and images are acquired with three sub-swaths (Figure 12) (De Zan et al. 2006). With this technique, problems such as scalloping or changes in sensitivity for different distances, are reduced. This allows for a harmonized performance along track and a homogenous image quality.

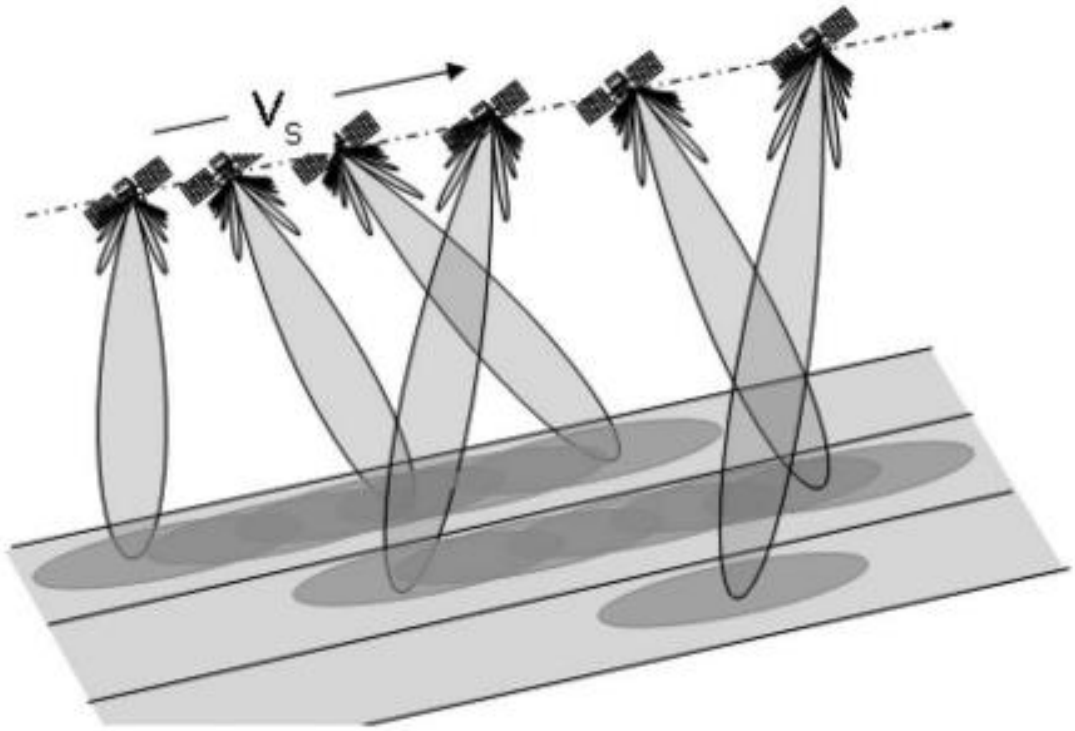


*Figure 12: TOPSAR acquisition: Orientation of signal sent by antenna along track. The three sub swaths along track with sensor velocity $V_s$. Source: (De Zan et al. 2006).*

## 4.3 Copernicus Mission: Sentinel 2

Optical imagery used in this study is captured from S2. S2 is a mission composed of two polar-orbiting satellites with an attached optical MSI sensor (Spoto et al. 2012; Chen et al. 2018). Being a multispectral instrument, S2 can detect wavelengths in the range of visible, NIR (Near Infrared) and SWIR spectrum or 442.3 nm to 2202.4 nm (Meena et al. 2021). Ranges are divided into a total of 13 bands (Table 2).

| Name | Description | Resolution pixel size | Wavelength |
|---|---|---|---|
| B1 | Aerosols | 60 m | 442,3 – 443,9nm |
| B2 | Blue | 10 m | 492,1 – 496,6nm |
| B3 | Green | 10 m | 559 – 560nm |
| B4 | Red | 10 m | 664,5 – 665nm |
| B5 | Red Edge 1 | 20 m | 703,8 – 703,9nm |
| B6 | Red Edge 2 | 20 m | 739,1 – 740,2nm |
| B7 | Red Edge 3 | 20 m | 779,7 – 782,5nm |
| B8 | NIR | 10 m | 833 – 835,1nm |
| B8A | Red Edge 4 | 20 m | 864 – 864,8nm |
| B9 | Water vapour | 60 m | 943,2 – 945nm |
| B10 | Cirrus | 60 m | 1373,5 – 1376,9nm |

| | | | |
|---|---|---|---|
| B11 | SWIR 1 | 20 m | 1610,4 - 1613,7nm |
| B12 | SWIR 2 | 20 m | 2202,4 - 2185,7nm |

*Table 2: Bands of S2: Band name, description and wavelength values for S2. Copernicus Sentinel data (Dataset Availability: 2015.06.23 -).*

S2 MSI is similar to the MSI of the optical satellite in NASA's Landsat missions. Their newest additions, L8 (Landsat 8) launched in 2013 and L9 (Landsat 9) launched in 2021, includes a TIR sensor and an operational land imager (OLI). With only 9 bands in the visible and short-wave infrared, OLI does not include the red edge bands (Song et al. 2021). OLI has also a lower resolution than S2 and a revisit time of 16 days. S2 has a 5-day revisit time, excluding overlap of lateral swaths (Spoto et al, 2012), (Li et al 2020). Repeat time for one S2 satellite is 10 days, but similarly to S1, S2 is composed of two satellites, which reduces the repeat time in half. The S2 red edge has been proved advantageous in crop mapping. With higher spatial resolution it could be more efficient in accurately delineating flood edges (Song et al. 2021; Tulbure et al. 2022). However, the Landsat mission has been in operation with multi-spectral scanners since the first mission launched in 1972 with Landsat 1. The long timeframe is useful in studies in long term changes of the land surface.

### 4.4 Digital Surface Model: JAXA ALOS DSM

ALOS World 3D Surface Model or AW3D is a global DSM with a spatial resolution of 30 m. Commissioned by the Japanese Aerospace Exploration Agency (JAXA), the Advanced Land Observing Satellite (ALOS) was in use between 2006 and 2011 for disaster monitoring. The archive of ALOS was later used in 2014 to create the world DSM from the PRISM or Panoramic Remote Sensing-Instrument for Stereo Mapping, which measures land elevation (Tadono et al. 2014). Corrections to the dataset includes a void filling method called Delta Surface Fill (DSF), which adjusts void values resulting from rugged topography and cloud cover (Takaku et al. 2014). One of the latest updates to the dataset was in version 3.2, where pixel spacing and sea masking was improved in areas above 60 degrees north (Takaku et al. 2020). This makes AW3D one of the few global DSM in GEE with decent quality in the northern latitudes. For this study, version 3.2 of the AW3D30 is used as a tool to specify terrain elevation and slope gradient.

### 4.5 Datasets Summary

Table 3 shows the summarized metadata of the different datasets captured for each study area. Images were further used to visualize and detect floods by different approaches described in

the method chapter. Orbit track referrers to the track the satellite follows as it orbits the earth. The orbit number refers to a specific orbit track.

| Study Area | Dataset | Date | Orbit track | Orbit Number | Use | Nr of Images |
|---|---|---|---|---|---|---|
| **SA1 Stjørdal** | Sentinel 1 | 13.01.2022 | Ascending | 73 | Flood | 1 |
| | Sentinel 1 | 10.08.2021-27.10.2021 | Ascending | 73 | Reference | 15 |
| | Sentinel 2 | 15.01.2022-22.01.2022 | Descending | 8, 51, 94 | Flood | 3 |
| | Sentinel 2 | 06.06.2022-01.09.2022 | Ascending and descending | 8, 51, 94 | Reference | 14 |
| **SA2 Sunndal** | Sentinel 1 | 28.06.2022 | Ascending | 44 | Flood | 1 |
| | Sentinel 1 | 20.05.2022-30.07.2022 | Ascending | 44 | Reference | 10 |
| | Sentinel 2 | 29.06.2022 | Ascending | 51 | Flood | 1 |
| | Sentinel 2 | 20.05.2022-30.07.2022 | Ascending and descending | 51, 94, 137 | Reference | 10 |
| **SA3 Layyah** | Sentinel 1 | 02.03.2022 | Ascending | 71 | Flood | 1 |
| | Sentinel 1 | 02.03.2022-25.05.2022 | Ascending | 71 | Reference | 8 |
| | Sentinel 2 | 31.08.2022 | Descending | 91 | Flood | 1 |
| | Sentinel 2 | 01.03.2022-30.05.2022 | Ascending and descending | 48, 91 | Reference | 33 |
| **SA1, SA2, SA3** | Alos DSM 3D | 2006-2011 | Ascending and descending | | | |

*Table 3: Satellite sensor datasets of SA1, SA2 and SA3.*

## 5. Method

In this section, processing, analysing, visualizing and detecting features in the landscape is explained. Excluding visualizing results in ArcGIS Pro, all processing steps of satellite data to the final product were acquired in GEE. A flowchart of each step taken is shown in Figure 13, and further explanations of each process is explained in the underlying chapters 5.1 to 5.6. The methods in this study were tested on the three different case studies: 1) SA1, The 2022 Gyda rain flood in Stjørdalen; 2) SA2, the 2022 snowmelt flood in Sunndal; 3) SA3, the 2022 monsoon flood in Layyah, Pakistan.

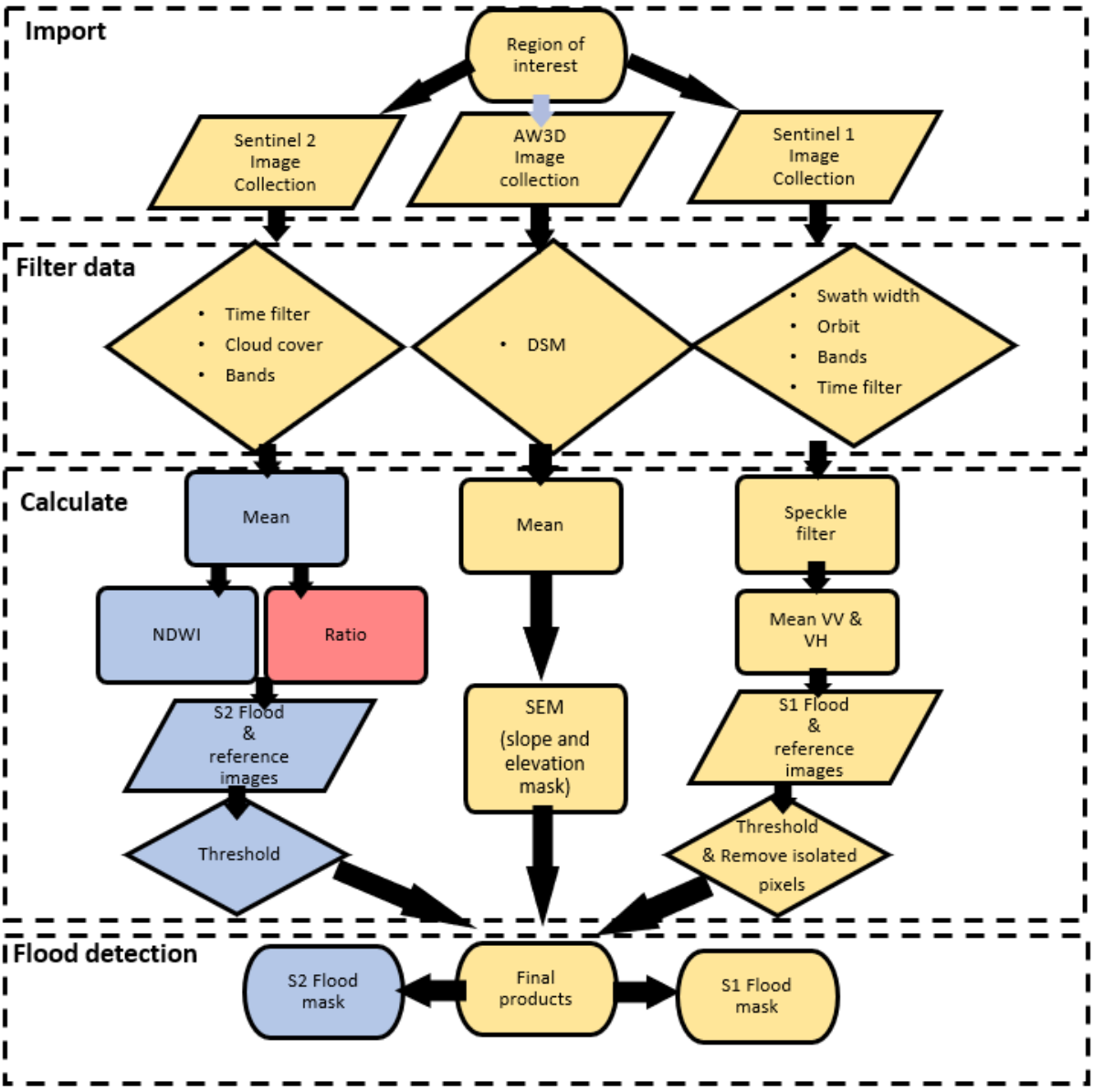


*Figure 13: Flowchart of processing steps for each study area. Yellow indicates all study areas included this processing step, red indicates only SA3 included this processing step and blue indicates SA2 and SA3 includes this processing step.*

## 5.1 Data Pre-processing and Filtering

In this study, VV co-polarized and VH cross-polarized images were captured with the C-band S1 synthetic aperture radar. S1 data is found in the GEE image collection: ee.ImageCollection("COPERNICUS/s1_GRD").

MSI S2 data includes the B3 band and B8 band, which is used in order to calculate NDWI. S2 data is found in the collection: ee.ImageCollection("COPERNICUS/S2_SR") in GEE.

The data provided by Copernicus S1 is pre-processed in GEE, where backscatter coefficient values have been changed from σ˚ to decibels dB. Negative values indicate most scatter is away from the sensor, and positive values indicate that most of the backscatter returns to the sensor.

Backscatter is visualized as pixels in GEE, where pixels have been adjusted for the incidence angle, topography, and variation in object-heights that could create distortions and worsen image quality. S1 data found on GEE is pre-processed and can be described in 5 steps: Terrain correction, apply orbit file, thermal noise removal, GRD (Ground Range Detected) border noise removal, and Application of radiometric calibration values (Bayanudin et al. 2016; ESA, 2022).

In addition to the pre-processing steps provided by Copernicus, the user can filter the data with the help of different metadata properties. For this paper, the S1 data is acquired in IW, which has an incidence angle that varies between 29.1˚ and 46˚. Additional settings and properties of S1 data helps users define the polarization, swath width, and including either one or both orbiting tracks. The interaction between viewing angles and the surface could result in image distortions (Section 3.1). To reduce these effects, similar orbit direction and orbit path were used for reference and flood images. Speckle, also known as "salt and pepper noise", can occur in S1 images and make it difficult to distinguish between different objects in the image (Belba et al. 2022). To reduce the speckle noise, a speckle filter created by Lemoine. (2018) was applied to the S1 imagery. This allows for better visualization of backscatter, but it could also potentially reduce or remove valuable details of land surface information.

S1 and S2 data is obtainable in different products: level -0, level 1, and level 2, where level 0 is the first product processed from the raw data. The S1 product used for this paper was the level 1 Ground Range Detected product. S2 products include level-1A, level-1B, level-1C and level-2A (Moskolai et al. 2022). Only level 1C and 2A is obtainable for users. In this paper, level 2A is used to calculate NDWI. Both level 1C and 2A follows the UTM/WGS84 projection, which divides land surface into multiple tiles, where each tile is 100x100 $km^2$. S2 1C is described as a TOA (Top-of-atmosphere) product and 2A is BOA (Bottom-of-atmosphere) product, which corrects for scattering and absorption effects of the atmosphere that TOA does not include (Chen et al. 2018).

### 5.2 Implementing algorithms for NDWI, Ratio and Backscatter

Band 3 and 8 from S2 level 2A were used to calculate NDWI (section 3.4), where band 3 represents GREEN, and band 8 represents NIR (Formula 1). Different scales exist for NDWI, but similarly to NDVI, the most used range is between -1 and 1 (Grover et al. 2015; Gao, 1996). To visualize different surface conditions, each pixel was given a value between -1 and 1. Table 4 shows colours and corresponding hex colour codes for values between -1 and 1, representing different amounts of water on the land surface. Ranges from -1 to -0.3 is described as drought, dry, or no water surfaces. Ranges from -0.3 to 0 is described as moderate drought with dry or

no water surfaces. Ranges from 0 to 0.2 is described as humid or flooding and 0.2 to 1 is described as water surfaces (EOS, 2021). Adjusting these values could help detect floods in different terrain by supressing noise or increasing contrasts in e.g., built-up land, lakes, rivers, or coastal areas (Xu, 2006). These values work as a baseline for the flood thresholding with NDWI. However, each value is not exact and they will vary based on terrain and locations (Gu et al. 2008). Consequently, reference RGB images of each area were used to verify if flood masking was accurate or needed correction.

| Colour | HEX | Value NDWI | Value Ratio |
|---|---|---|---|
| Red | FF0000 | -1 to -0.66 | 0 to 0.33 |
| Orange | FFA500 | -0.66 to -0.33 | 0.33 to 0.66 |
| Yellow | FFFF00 | -0.33 to 0 | 0.66 to 1 |
| Light blue | ADD8E6 | 0 to 0.33 | 1 to 1.33 |
| Blue | 0BA4D6 | 0.33 to 0.66 | 1.33 to 1.66 |
| Dark blue | 00008B | 0.66 to 1 | 1.66 to 2 |

*Table 4: NDWI Colour table: Different colours and their corresponding hex value and ndwi value*

S1 imagery was visualized with a brightness/darkness map, in addition to an RGB image of the ratio between VV and VH. S1 reference and flood image had identical orbits to avoid including shadow effects in the flood thresholding. Backscatter on inundated areas vary based on different inundation scenarios, such as terrain type, incidence angle and flood duration (Huang et al. 2022). A study by Manjusree et al. (2012) found an optimal range for flood detection in VV and VH to be -6 to -15dB and -15 to -24dB (with 20˚ to 49˚ incidence angles). These ranges were used as a baseline to create a flood threshold of the S1 imagery. In addition to this range, optical imagery was compared for further accuracy.

In SA3, flood detection with band ratio (Formula 2) were included in addition to NDWI. Similarly, to the NDWI formula, ratio were calculated by the use of band 3 and 8 from S2 level 2A. Ratio visualized different surface conditions in a range from 0 to 2, where comparisons to RGB flood imagery were used to find the flood threshold value. Ratio imagery used identical colour coding as table 4, but with a range from 0 to 2 instead of -1 to 1.

### 5.3 Temporal Image Stack

A synthetic reference image was used for each study area in addition to the flood image. By using a reference image, thresholds can be made that highlight only the flooded surfaces in the landscape. This can be done by comparing one singular image to another and detecting the change between them. However, singular images can be a problem as terrain can change in the span of a year, due to seasonal changes in the landscape. A reference image from a period of drought, snowfall, vegetation growth, or built-up areas, could leave out areas that usually

contain water. Conversely, rainfall and other floods could give an indication of more water in commonly dry areas. From these scenarios, the reference image could give over- or underestimations of inundation during flood.

Image stacks over longer time periods have been used in different studies to remove or reduce outliers, such as dry days, wet days, or snow cover (Bazilova et al. 2022). This process is known as image or data fusion, where multiple images are combined to refine the quality of the data (Pohl et al. 1998). In this paper, an image stack was acquired over a 3-month time-period. The stacked image could then be reduced to an average of the stack. The average was calculated for each reference image by the use of the .mean() function in GEE. This calculation reduces an image collection to one synthetic image where each of the matching pixels across the stack is given its average value (Earth Engine, 2022). For SAR, this value was a mean backscatter coefficient, and for optical imagery it was a mean NDWI value. The synthetic reference image was further used in the thresholding of NDWI and backscatter images.

"CLOUDY_PIXEL_PERCENTAGE" is a property that can be obtained in the S2 level 2A product. This property filters imagery based on the percentage of clouds found on the image, and is generated from the level 1C product (Braaten, 2023). It is recommended to use low cloud pixel percentage in flood detection, as the clouds would interfere and obstruct flooded pixels (Fisher, 2015). In this study, a cloud percentage of 30 % was set to the S2 reference stack to reduce misleading flood mapping results. It is important to note that the images could contain some amount of cloud pixels, and therefore visual inspections were also important.

While the reference image was computed from a stack of multiple images, capturing several S1 or S2 images during a flood proved to be challenging. Flooding in SA1 lasted for only 3 days, 5 days in SA2 and 4-5 months in SA3. The short flood periods for SA1 and SA2 were shorter than the repeat orbit time for S1 which has a 6 day-orbit time, and S2, which has a 5 day-orbit time. Therefore, only one image was captured for each area during the flood.

### 5.4 SEM - Slope and Elevation Mask

Slopes and elevated areas could pose a problem for flood mapping, as shadows or the terrain could falsely indicate flooded areas for both S1 and S2. Since water flows from high to low terrain and pools up in pits or flat terrain, flooding is unlikely in long and steep slopes. Consequently, in this paper, a slope and elevation-masking (SEM) procedure was completed to improve accuracy of flood masking. To perform the procedure, the base model AW3D was used to get terrain elevation data for each study area. Using a threshold of 5 degrees for slope

masking have proven high accuracy in flood detection (Lin et al. 2019; Wang et al. 2022). Consequently, a threshold was set where slopes over 5 degrees was masked. Elevation was also taken considered. Since rivers and small pools could fill up while also having 5-degree slopes, an elevation mask was set where areas above a specified limit would not include the slope mask. In large study areas, such as SA3, multiple DSM images covered the area and the .mosaic() method was used which merges overlapping images into a single image. The result was a SEM created with a 4-step method starting with a base DSM model captured from AW3D (Figure 14):

1. Acquire DSM of the study area
2. Mask out slopes >5 degrees
3. Mask out elevation above a set limit
4. Combine both slope and elevation mask

For SA1, the minimum elevation requirement was 30 m, for SA2 it was 60 m and for SA3 it was 250 m. These values were found by studying the terrain, where steep mountains and flat terrain and lakes were determining factors on where to set the limit. The slope mask was not applied to terrain below the elevation limit, whereas it was applied to terrain above the limit. The objective was to incorporate the SEM for mountainous areas, which are characterized by significant variations in elevation. The slope and elevation mask of each study area can be found in appendices I, II and III.

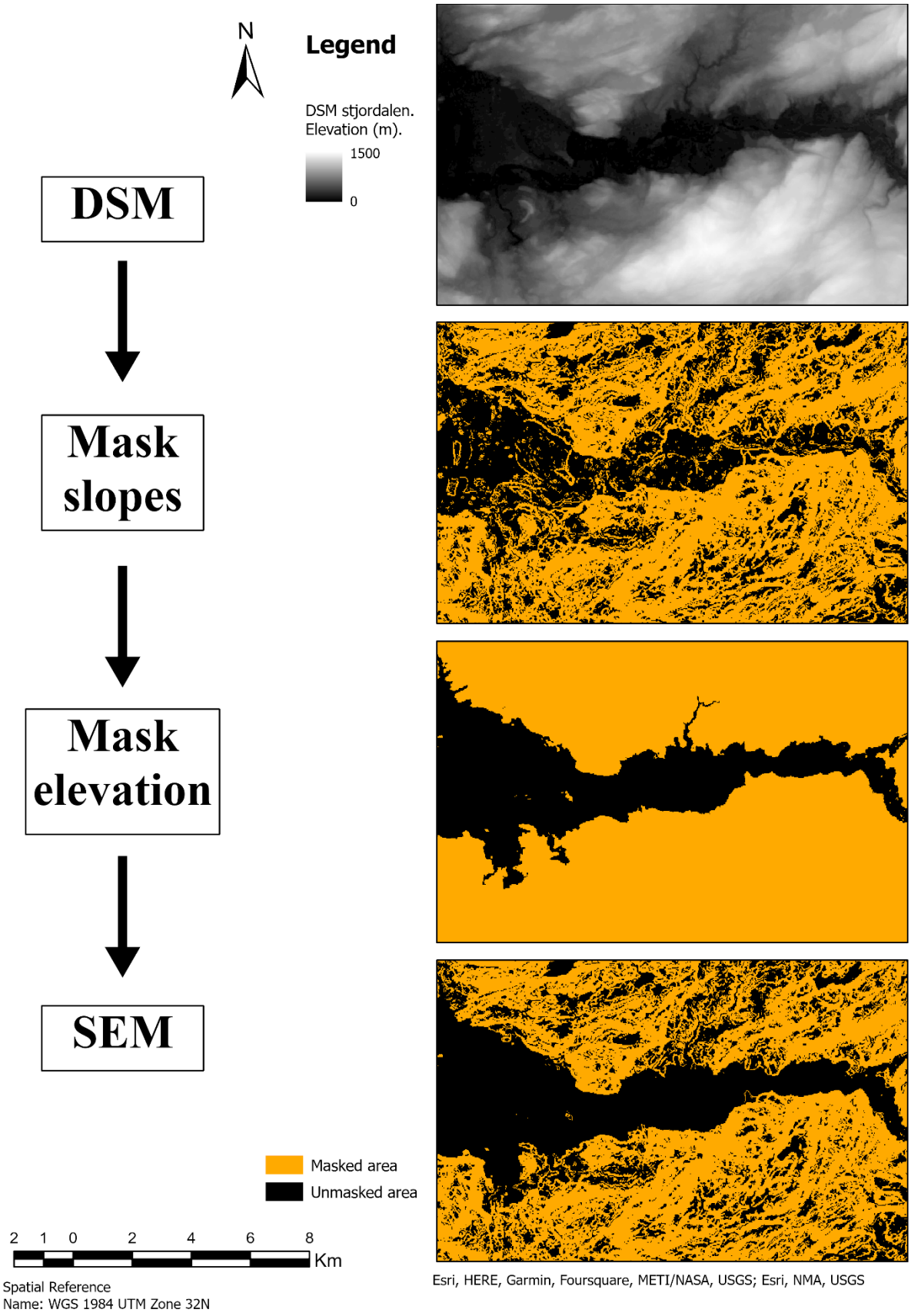


*Figure 14: SEM process steps: A flowchart and corresponding DSM calculation to calculate the SEM. This figure shows SA1.*

## 5.5 Separated Pixels

Pixel removal is a procedure to remove noise, and involves setting a threshold for specific number of connected pixels detected as flooded (Liang et al. 2020). In SAR images, backscatter intensity can vary significantly between adjacent structures. This can lead to different classifications between similar structures, such as water bodies, agricultural fields, grasslands etc. To reduce this effect on the flood detection, flooded areas were defined as areas with more than 8 connected pixels. Since both VV and VH flood imagery had a certain amount of noise, small areas could potentially be misclassified as flooded areas. If these areas were included in the flood masking, further processes, such as area calculations of each flood mask would also be overestimated. Removed pixels for SA1, SA2 and SA3 can be found in appendices I, II and III respectively.

## 5.6 Segmented Areas

Given the map scale of each study area, detailed study of each area needed closer inspection and therefore a higher exaggeration level. This was done by segmenting each study area into smaller parts. The aim for each part was to investigate different areas, where backscatter and NDWI mechanisms might differ. Surface features, such as forests, rivers, and agricultural land, could also be inspected closer.

# 6. Results

This section presents the results for S1 and S2 data in two chapters: Part 1: Visualization and Part 2: Automatic Thresholding. Each study area includes the S1 SAR imagery and AW3D slope and elevation model. S2 optical imagery and thresholding is included for SA2 and SA3, while SA1 only includes the reference S2 imagery. The flood image was obstructed by clouds. Thus, no thresholding for the NDWI was done for SA1.

## 6.1: Visualization of Inundated Areas

Before inundated areas were detected and masked, each study area was visualized with the different methods explained in section 5. Several components would lead to the availability of different maps for each study area. In SA1, due to clouds, S2 images were unavailable during the flood. SA2 had both S1 and S2 imagery of the flood. SA2 displays a small flood, and therefore, little difference was seen between the reference and flood image. SA3 had the largest flood, but also turbulent flood waters. Band ratio imagery was also included, in addition to NDWI and backscatter for SA3.

### *6.1.1 SA1 Stjørdalen*

Found roughly on latitude 63.450˚, longitude 10.940˚, SA1 lies in Trøndelag, Norway. The flood took place between January 12$^{th}$ -14$^{th}$, 2022, and the S1 flood images were captured on January 13$^{th}$, while S2 flood image were captured on January 15$^{th}$. In Stjørdalen during winter, the valley is snow-covered. Since backscatter mechanism on wet snowpacks could resemble water bodies, this was taken into consideration. Consequently, instead of using a stack between November and January, the S1 image stack was acquired during autumn, between August 10$^{th}$ and October 27$^{th}$, 2021. Between this period, a total of 15 images were acquired in orbit track 73 Ascending.

Figure 15 shows S2 RGB images before and during flooding. The images are visualized in GEE by using band b2, b3 and b4, representing blue, green, and red respectively. Reference image A was acquired with the ".mean()" function of 5 images acquired between August 28$^{th}$ and October 4$^{th}$, 2021. Each of the images had a 30% cloud cover filter. Figure 15B was acquired on January 15$^{th}$, 2022, one day after the flood ended. The figure displays clouds obscuring the land surface. Figure 15A displays the land use in Stjørdalen, where light green and brown agricultural land and grasslands dominate the valley floor, in contrast to the adjacent dark green and brown mountains.

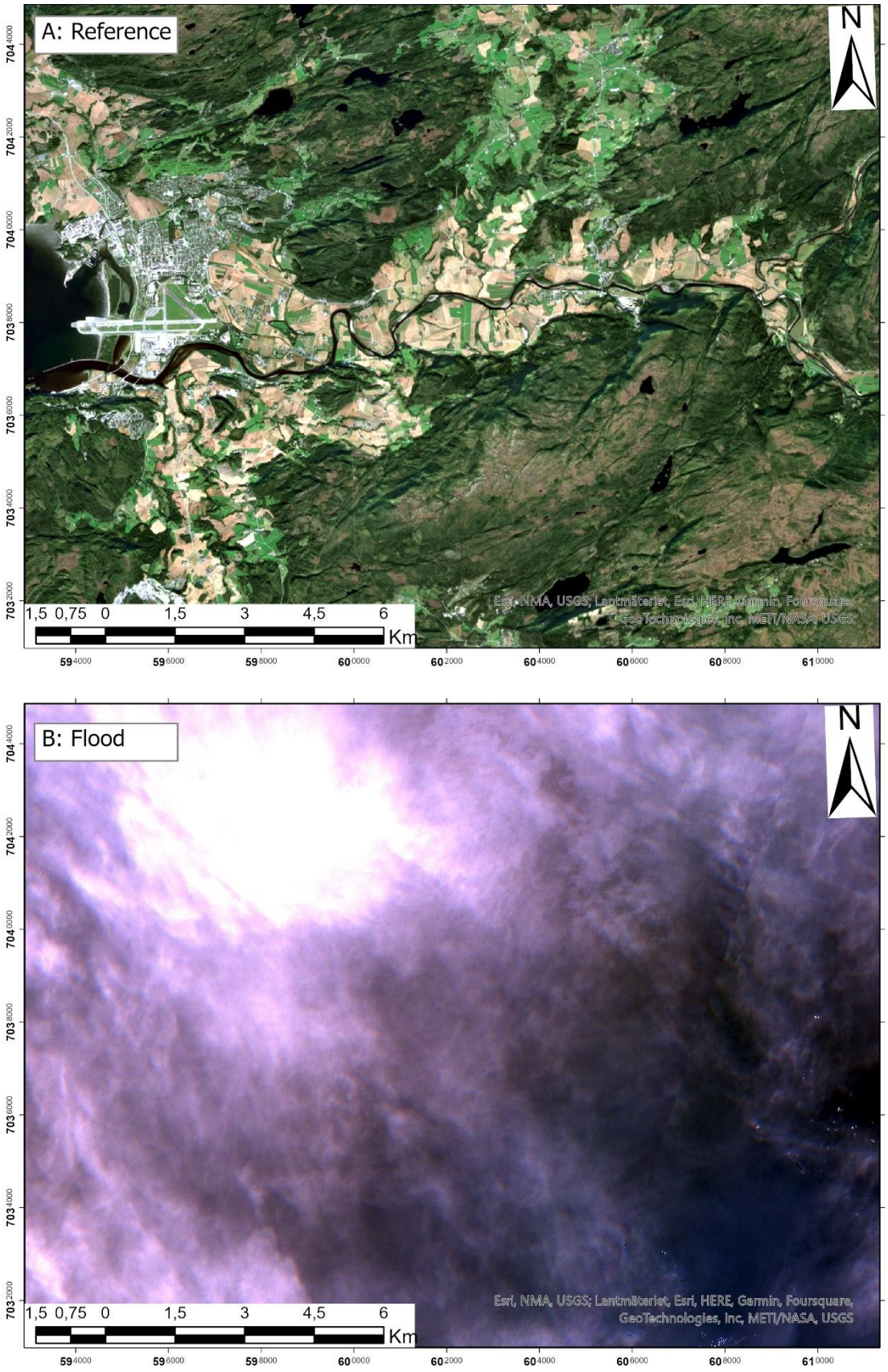


*Figure 15: RGB Reference and Flood image of SA1. A) Reference of SA1. B) Flood image of SA1.*

Figure 16 shows the S1 reference and flood image with the applied VV and VH backscatter polarizations. Bright pixels correspond to stronger backscatter signal, while darker pixels show lower backscatter values. Figure 16B shows high contrast between water bodies and land for VH polarization, while the VV polarization in 16D shows less contrast. Dark patches around and near the Stjørdal river shows potentially inundated areas. These areas range between -27 to -20 dB in VH and -21 to -9 dB in VV (16B and 16D). The biggest change in backscatter between reference and flood image occurred between 6 and 9 km upstream of the river outlet. This area consists of agricultural land, grassland and forests around the river, and a highway north of the river. S2 NDWI flood and reference images were excluded due to cloud cover obscuring view of the land surface.

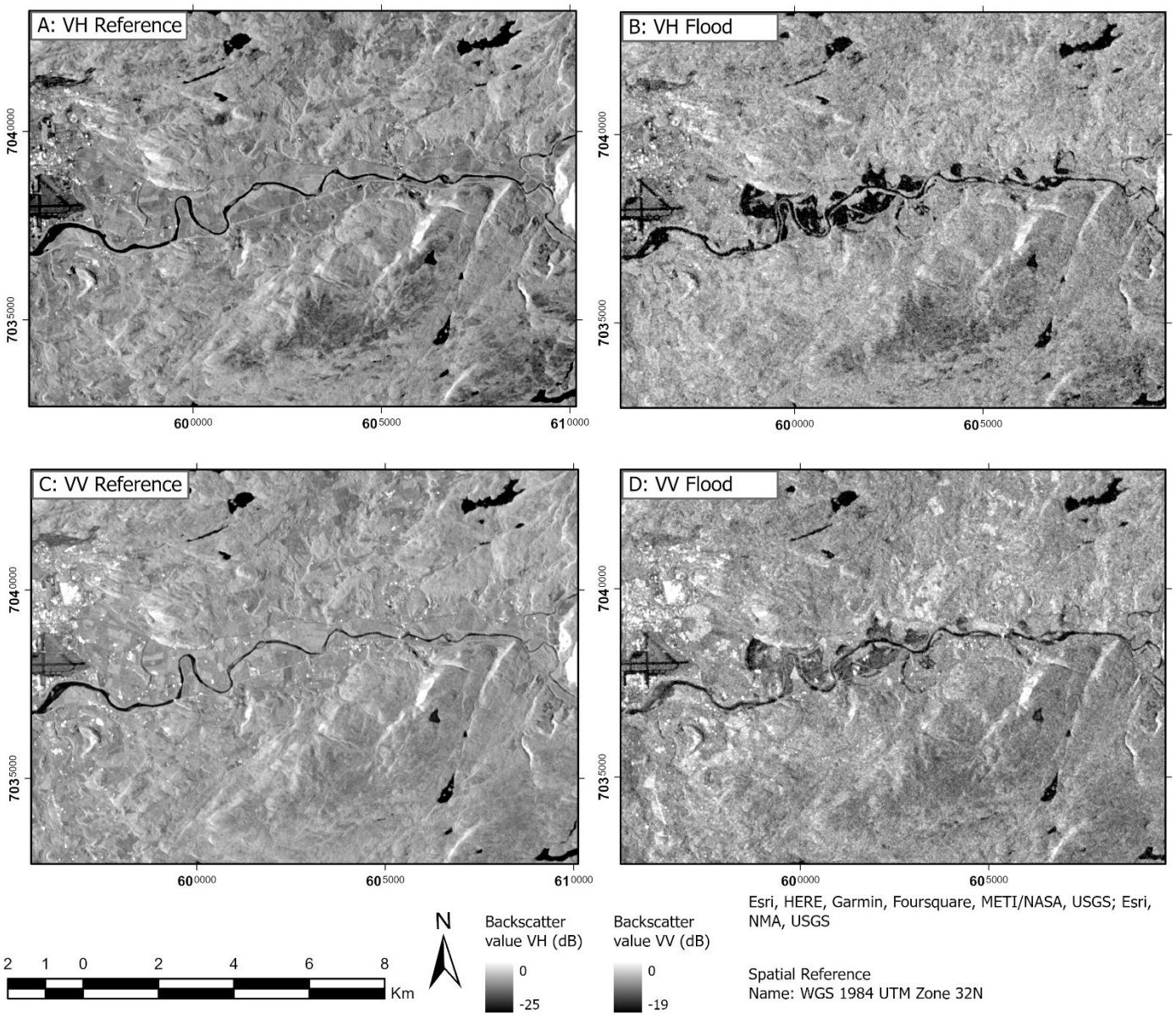


*Figure 16: SA1, Stjørdal Reference and Flood Images: A) Backscatter VH reference image where black and white shades correspond to high and low backscatter value respectively. B) Backscatter VH flood image. C) Backscatter VV reference image. D) Backscatter VV flood image.*

Figure 17 displays the updated image where the isolated pixels shown in red are removed. A connection of 8 pixels or less detected as flood is removed from the flood image. This procedure was done for each study area. It lessened overestimations of areas detected as inundated from the flood area calculations.

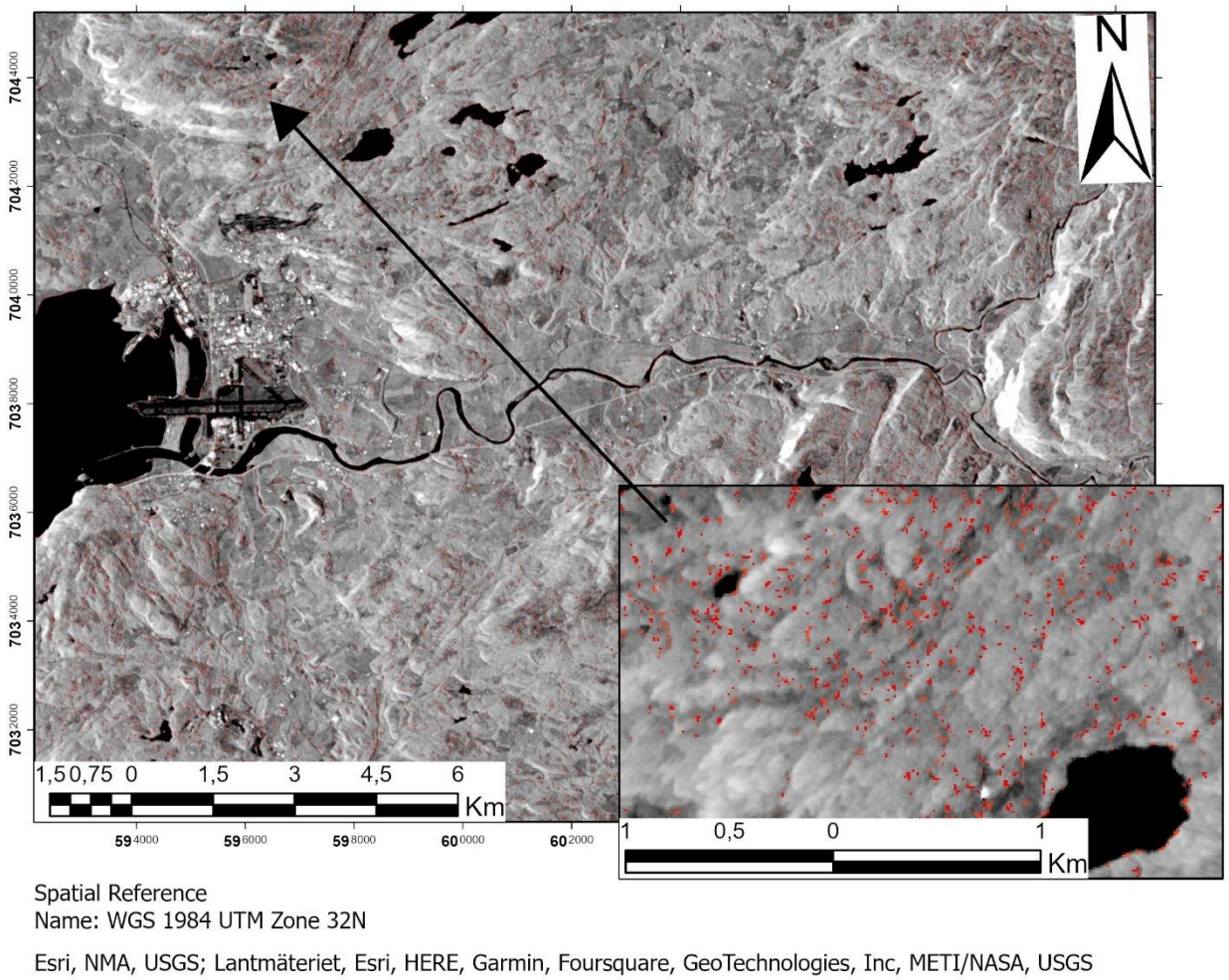


*Figure 17: Separated pixels detected as flood in SA1. The small red pixels seen on the image is pixels that were removed from the detection method.*

Figure 18 display SA1 VH reference images for two different time series. The reference image of each study area was initially proposed to contain images from the preceding months. However, reference stack of winter months contained snow which could lead to misclassifications. SA1 backscatter reference imagery had a proposed date range from November, 2021, to January, 2022. The final date range used for thresholding were between August, 2021 and November 2022. Figure 18 A shows the proposed date range in VH, while B shows the final range used in change detection. Potential accumulated snow is visible as darker areas in A, compared to B. Darker areas with similar backscatter values as the flood threshold could lead to misclassifications where the flood was detected as permanent water body. Consequently, reference image 18 B from earlier months were used, instead of A.

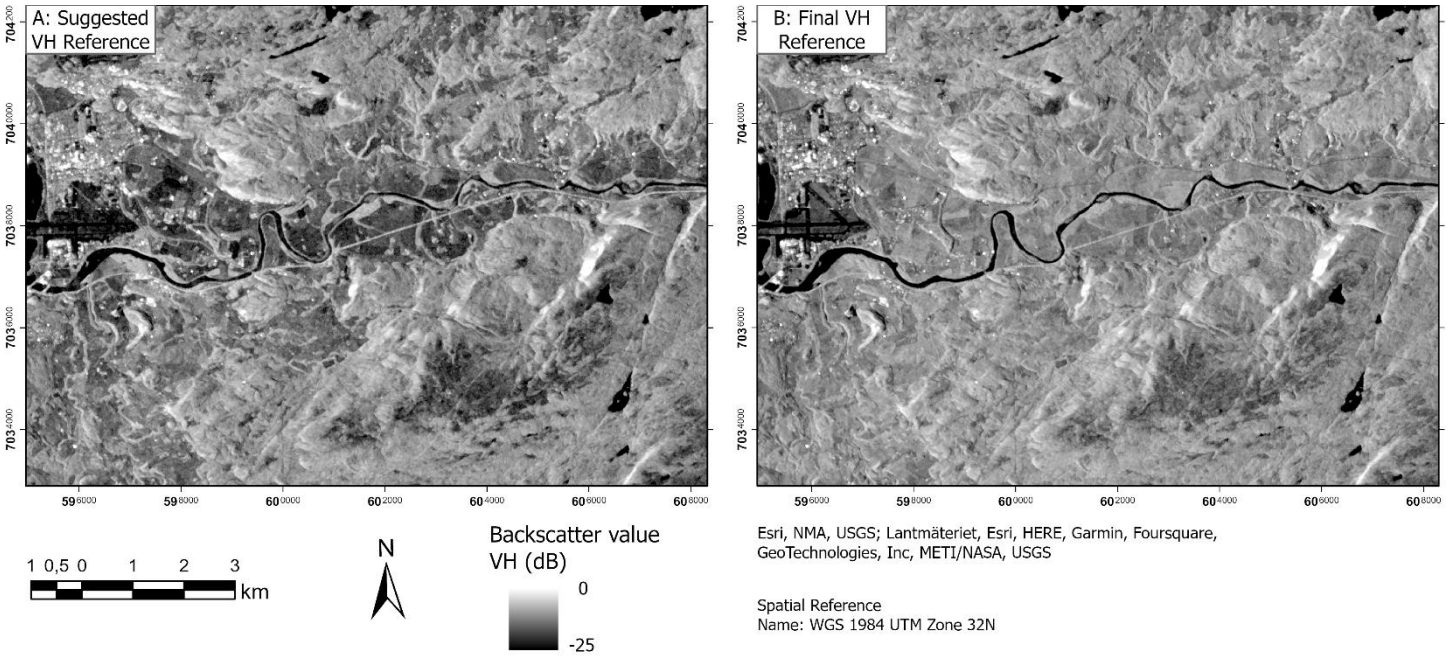


*Figure 18: Reference stack of SA1 in VH for two different time series. A and B: reference stack from November to January. B: reference stack from August to November.*

### *6.1.2 SA2 Sunndal*

SA2 is located roughly on latitude 62.670˚, longitude 8.600˚ near the Driva river outlet. Lasting between June 27th and July 1st, 2022, the S1 flood images were captured June 28th and the S2 flood image was captured June 29th. A total of 10 images, the reference stack for S2 was compiled from May 20th to July 30th with a <30 % cloud cover filter. The S1 image stack was sampled between April 29th and July 22nd, adding up to 10 images. Each image was in ascending orbit track 44.

Figure 19 displays S2 reference and flood RGB imagery of SA2. Although the smallest flood of the three study areas, a clear change occurs in the Driva river during flooding, as the colour of the river changes from a dark blue (Figure 19A) to light green (Figure 19B). Agricultural land, forests and houses can be found near the river. Agricultural land is also changing notably between 19A and 19B, where previously brown- and yellow fields changes into green fields. Mountains north and south of the river are snow-covered in both the reference and flood image. The slopes on the mountains south of the river show a white glow effect on the steepest parts (Figure 19b). The glow is a processing artifact in S2 level 2A caused by shadow and low

reflection in steep terrain hidden from the satellites line of sight. In SA2, only the north facing slopes experience this artifact.

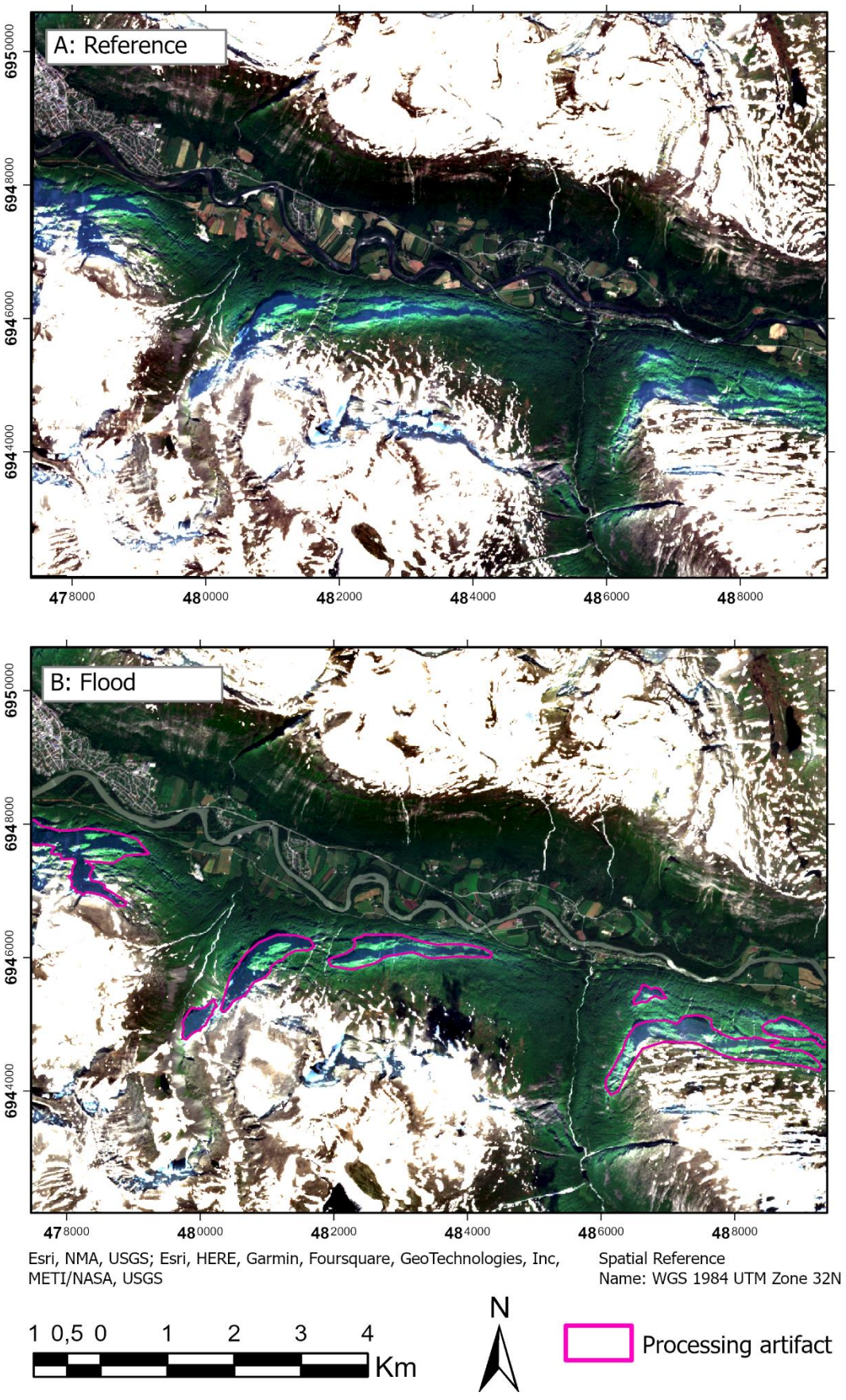


*Figure 19: RGB Reference and Flood image of SA2. A) Reference of SA2. B) Flood image of SA2. Processing artifacts is displayed in pink.*

Figures 20A-B shows the calculated NDWI for the reference and flood image. With a range between -1 to 1, water bodies, moist or wet surfaces are shown in blue, with values ranging from 0 to 1. Dry surfaces are shown as yellow to red with values ranging from -1 to 0. Flowing along the bottom of the valley, the Driva river is seen as dark in Figures 20C - F and dark blue in the NDWI imagery (Figures 20A - B). The bottom of the valley has a low NDWI value in comparison to the south and north mountain tops that contain snow. In the S1 imagery, the north and east sides of the mountains have low backscatter values, while the south and west facing sides have higher values (Figure 20C-F).

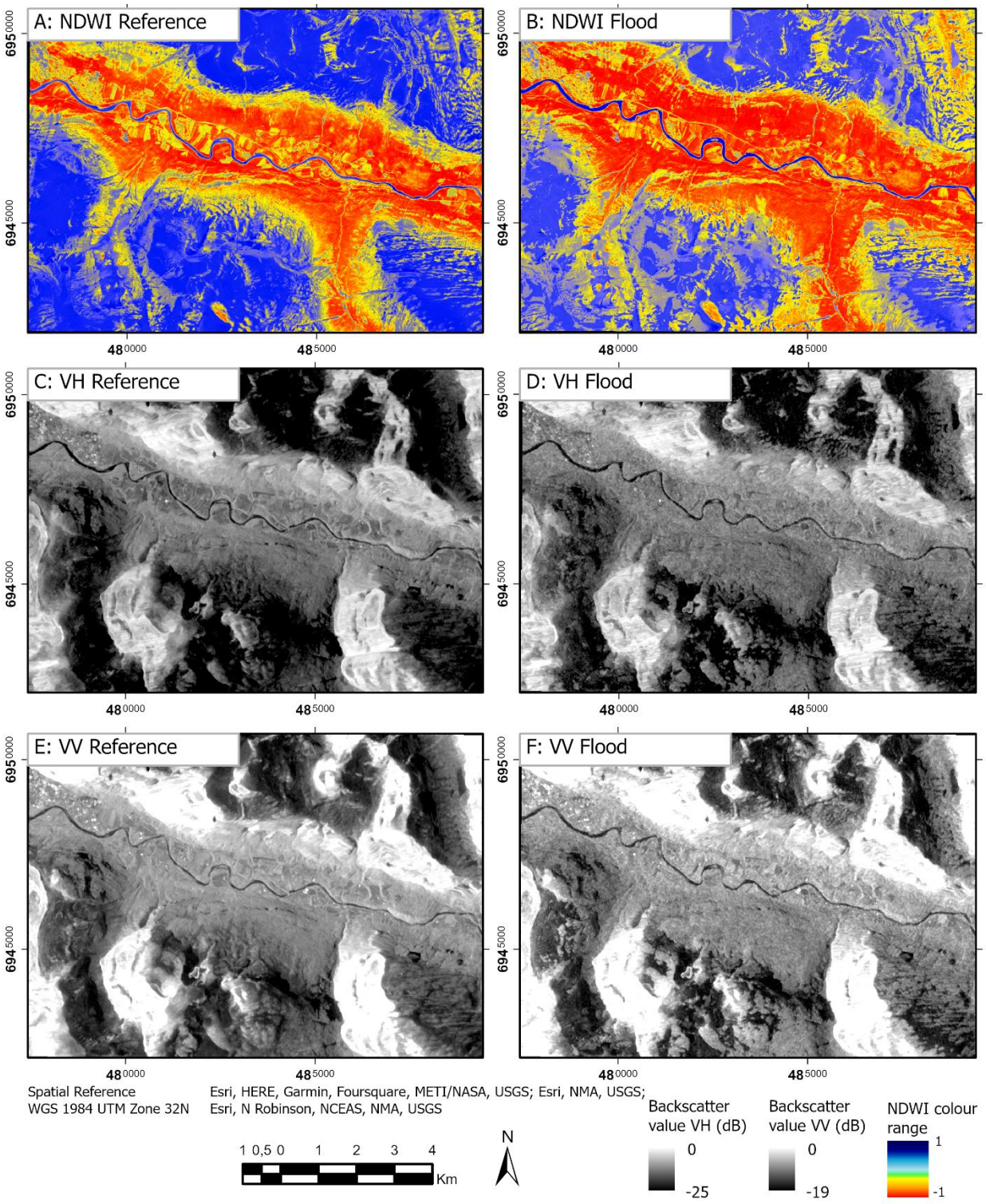


*Figure 20: SA2, Sunndal Reference and Flood Images: A) NDWI reference image with a scale from -1 to 1, where higher values appears as blue and lower values appears as red. B) NDWI flood image. C) Backscatter VH reference image. Black and white pixels correspond to the backscatter value from 0 to -25dB. D) Backscatter VH flood image. E) Backscatter VV reference image F) Backscatter VV flood image.*

The steep mountainsides of SA2 experience shadow, foreshortening and layover effects in flood and reference images (Figure 21). Both VV and VH imagery experienced these effects. Figure 21 displays mountains on the south-part of the Sunndal valley. Figures 21A and B display VH flood image. Shadows in shown on the east-facing mountain sides. The west-facing sides experienced layover, where the mountain top appeared to overlap the west-facing side. Foreshortening also appeared on west-facing sides, where pixels by the mountaintop appear as bright and compressed. Figure 21C is a slope map, showing inclination in the terrain. Several shadows are found on the east-sides of the steep mountain peaks. Figure 21D shows SEM and the VH flood mask, where some areas found within the shadow were misclassified as flooded.

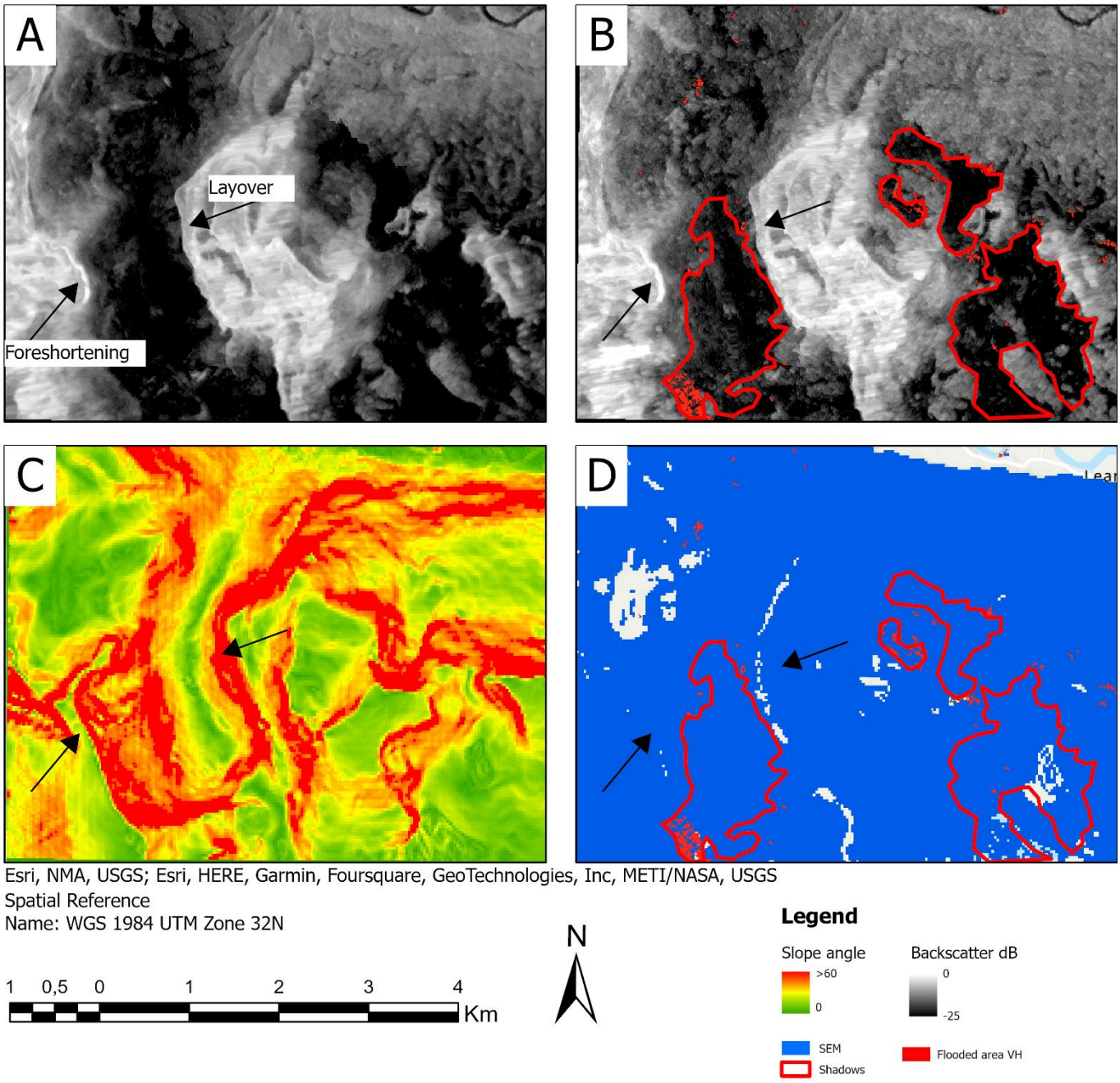


*Figure 21: SA2 Terrain distortions. A: VH flood image, B: VH flood image, VH flood mask and shadows, C: Slope map, D: SEM with shadow areas and VH flood mask.*

### *6.1.3 SA3 Layyah*

SA3 is found on latitude 30.770˚, longitude 70.720˚, capturing parts of the Indus River close to the city of Layyah. Flooding on the Kabul and Indus River peaked in late August (OCHA, 2022). S2 flood imagery were captured on August 31st, while S1 flood imagery were captured on August 29th. The reference stack for S2 contains 33 images between March 1st and June 1st 2022 and the reference stack for S1 contains 8 images between March 2nd and May 25th 2022. S1 images were in ascending orbit track 71. Both S1 and S2 maps were compared over the same area coordinates and within as similar of a timeframe as possible for reference and flood images. The difference of two days between the S1 and S2 flood images should be considered, and some differences between inundated areas of S1 and S2 are possible due to temporal differences.

Figure 22 shows reference and flood image of SA3. Displaying a change in the landscape, Figures 22 A and B shows a changing coloration from red and brown to green land. In comparison to the reference image, the Indus River increased in area and changed its colour from grey to a mud-brown colour. Clouds and cloud shadows covered the western parts of the study area (figure 22 B).

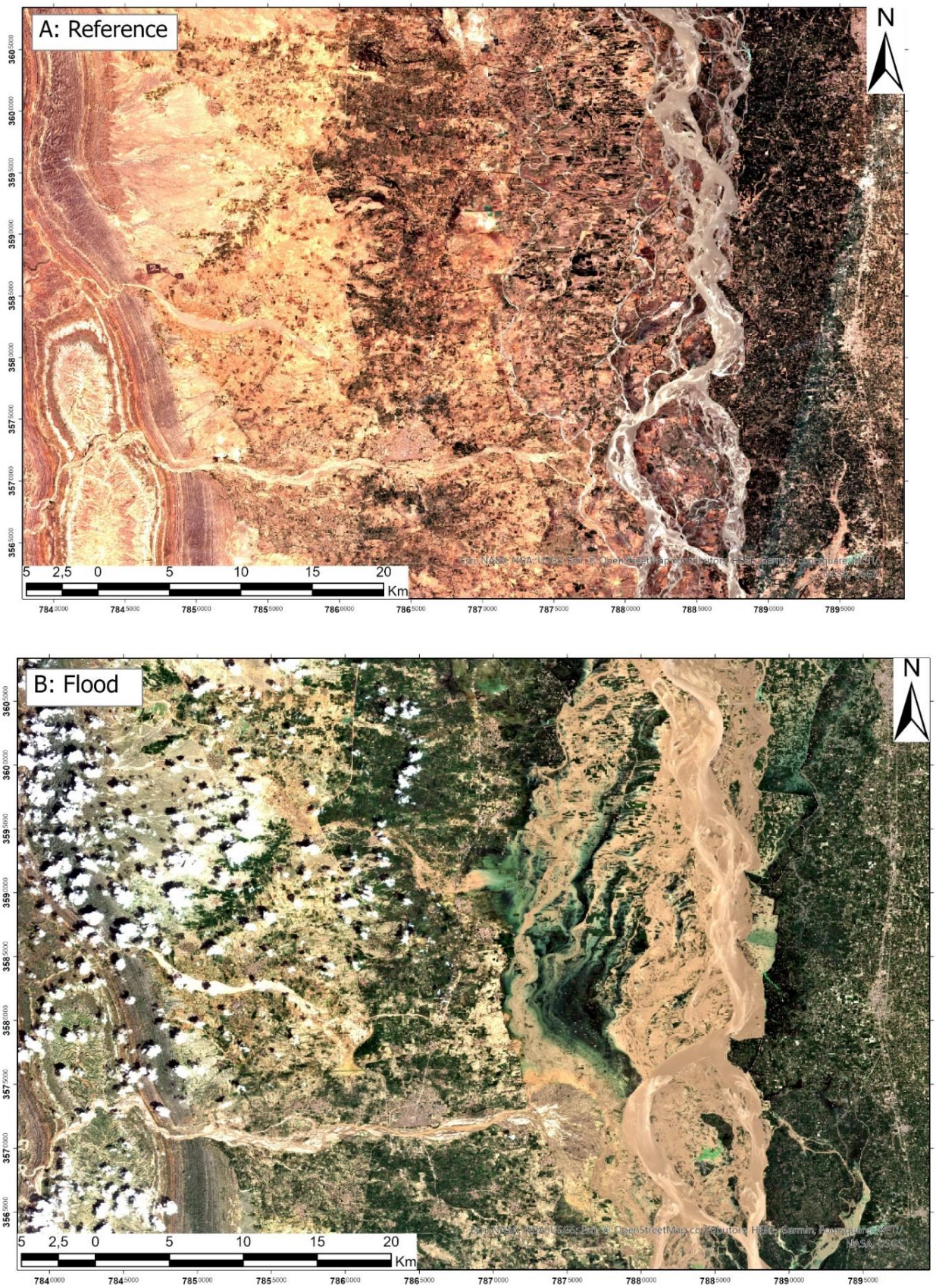


*Figure 22: RGB Reference and Flood image of Layyah. A) Reference image of SA3. B) Flood image of SA3.*

Floodwater flows in the Chasma right bank channel, until it changes course and follows a smaller channel flowing east of Kalarwala, thus overflowing the town of Nari Shumali and the Indus highway before it finally reaches the Indus (Figure 23A and 24C). As water level increases, features such as sand banks in the river disappear and roads acts as levees stopping the floodwater from reaching further inland (Figure 23B). Turbulent floodwater carries course sediments, changing the water colour to brown. The colour of the floodwater indicates a concentration of sediments in the water. Figure 24C shows a change in the water colour from mud brown to green, displaying a change from turbulent to calmer water. The Sanghar river flows from west into the Indus and during the flood, the river outlet forms a delta that extends over farmland (Figure 24D).

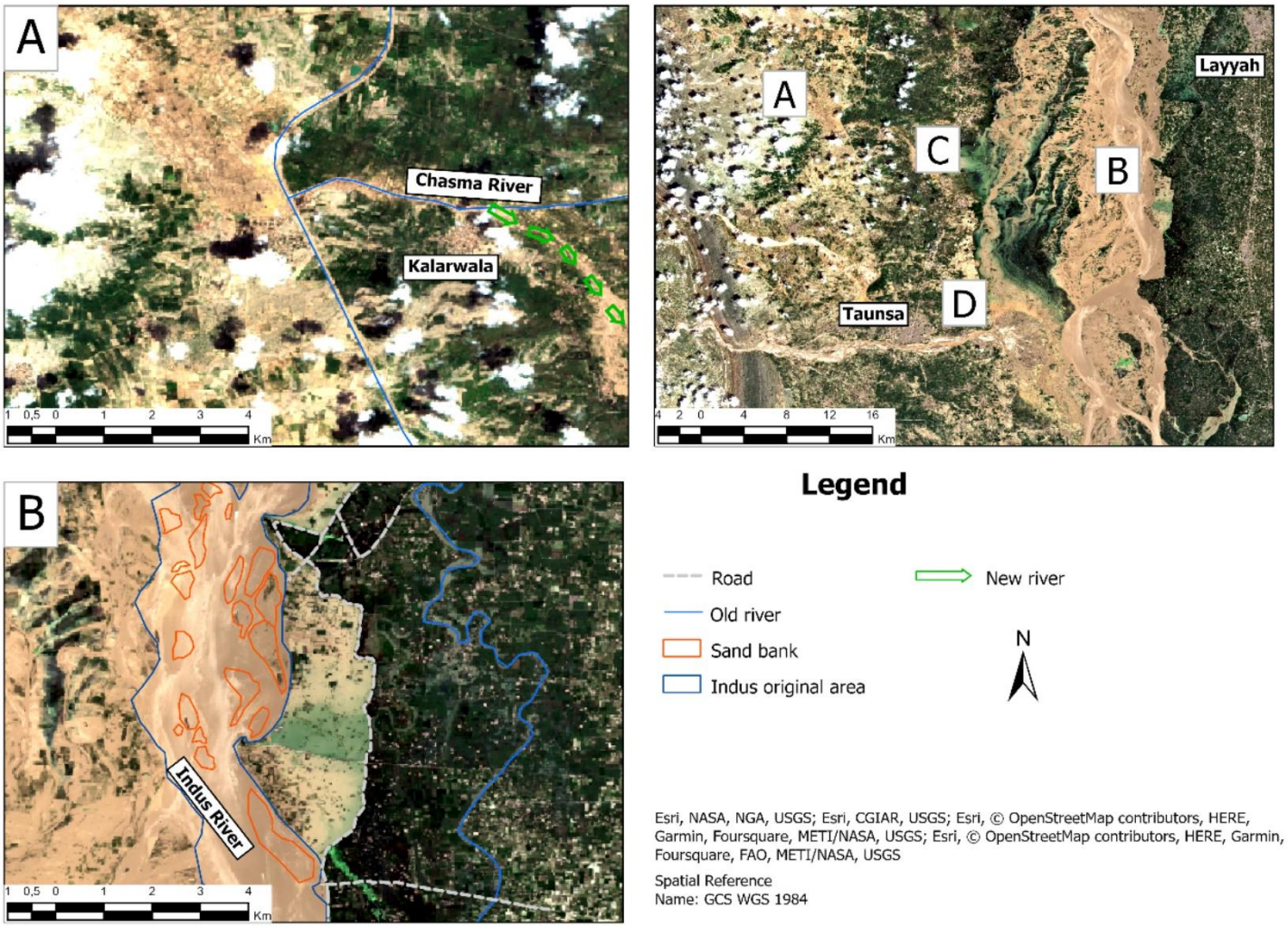


*Figure 23: Layyah RGB flood image, segments A and B. Each segment shows areas further investigated in S1 and S2 imagery results.*

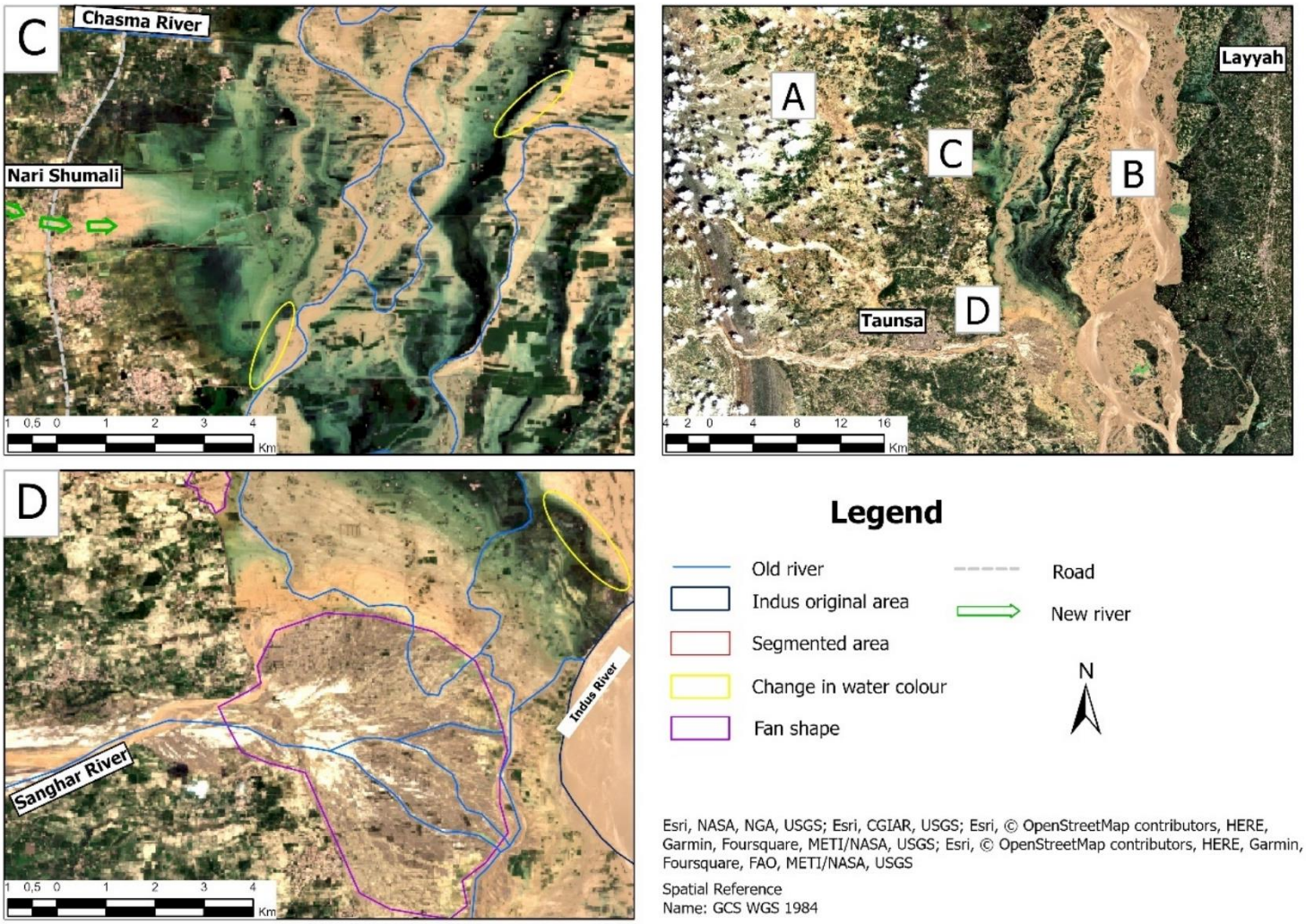


*Figure 24: Layyah RGB flood image, segments C-D. Each segment shows areas further investigated in S1 and S2 imagery results.*

Figures 25A-B shows the calculated NDWI for the reference and flood images of SA3. In the reference image, Indus River NDWI values range from -0.09 to 0.07, while in the flood image NDWI values have a larger range between -0.07 to 0.35. The highest NDWI values for the Indus could be found in the areas where the water changes from a mud brown to a blue colour, as seen in Figure 24C. Band ratio imagery maps a similar extent of the floodwater as the NDWI, and changing water properties is displayed with higher contrast from a dark blue to light purple. Ratio and NDWI displays a noteworthy variation in the pixel value range. Floodwater is not bound to a specific range, but changes as the turbidity and sediment concentration of the water changes. Figures 25 E and G display low backscatter values next to the Tiyar mountain range, with -20 to -27 dB in VH and -14 to -18dB in VV. This area is barren land with low amounts of vegetation and buildings. North of the Shangar River lies Taunsa city, showing high backscatter values in VH and VV. In 25 E and G, backscatter values of the Indus River range

between -25 and -20dB in VH and -17 and -13dB in VV. In 25F and H, the backscatter of the Indus River varied between -27 and -30dB in VH and -15 and -25dB in VV.

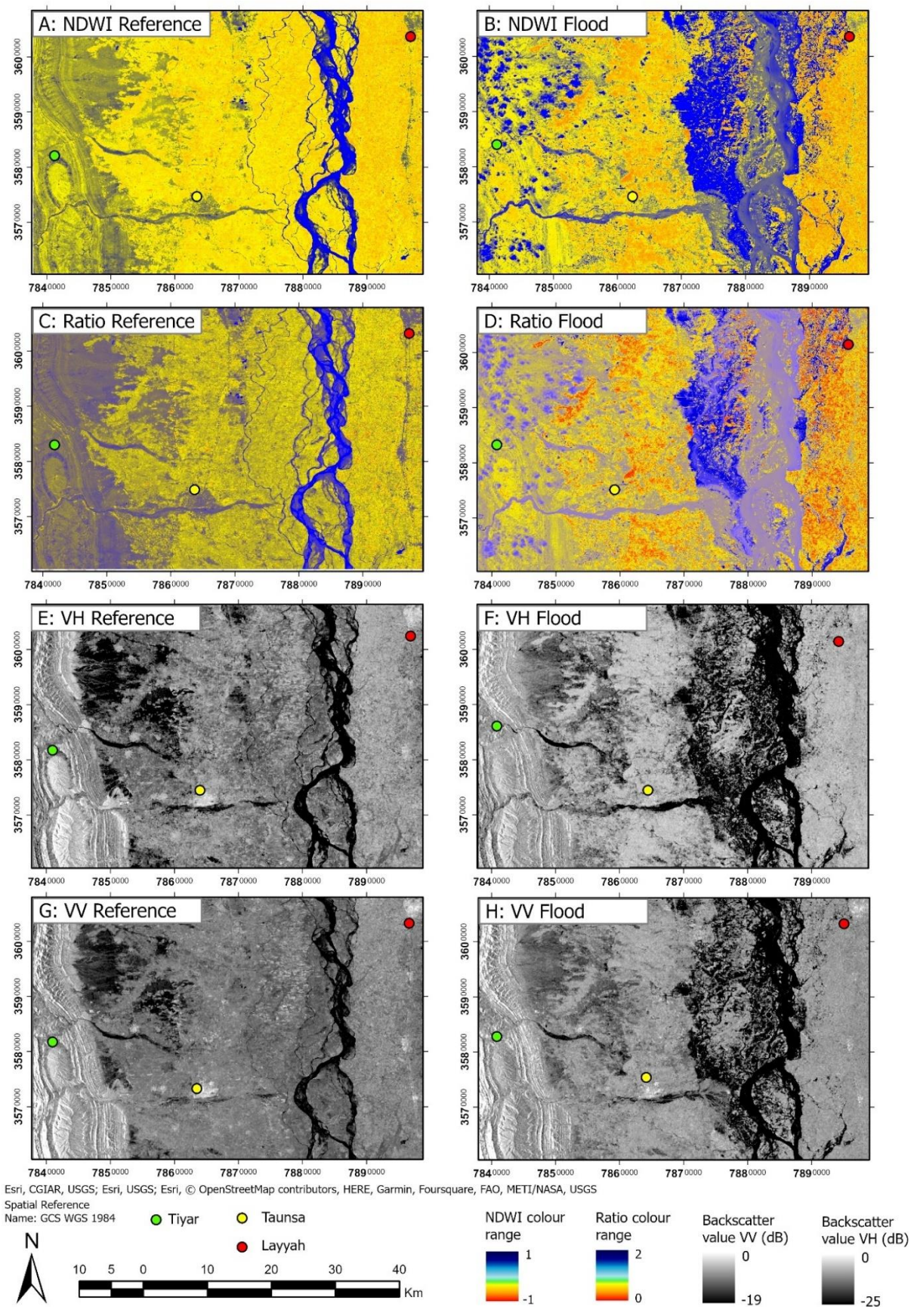


*Figure 25: SA3, Layyah Reference and Flood Images: A) NDWI reference image. B) NDWI flood image. C) Band ratio reference image. D) Band ratio flood image. E) Backscatter VH reference image. F) Backscatter VH flood image. G) Backscatter VV reference image H) Backscatter VV flood image.*

## 6.2: Flood Mask

To get as accurate results as possible for flood automatic detection, optical RGB imagery and DEM was used as a tool to help verify inundated areas with SAR and NDWI. In some areas, cloud cover would block view and limit the accuracy of optical detection methods. Inundated areas were calculated for each study area for S1 and S2 imagery and compared to each other. SA1 S2 flood image was covered by >70 % clouds. Due to the high amount of cloud cover, a NDWI flood threshold was not possible. Following, only thresholding with SAR imagery was possible. Thresholding was tested for values between -15 and -24dB for VH imagery and -6 and -15 for VV imagery. Table 4 shows the total calculated flooded areas with S1 for SA1, SA2, and SA3. Optimal threshold ranges in VV and VH and the resulting flood masks varied between -23 and -20 in VH and -15 and -12 in VV.

| Study Areas | Backscatter Threshold Values | | Total Inundated Area. Without SEM | | Total Inundated Area. With SEM | |
|---|---|---|---|---|---|---|
| | VH value (dB) | VV value (dB) | VH inundated area ($km^2$) | VV inundated area ($km^2$) | VH inundated area ($km^2$) | VV inundated area ($km^2$) |
| Study Area 1 | -15 | -6 | 8.25 | 2.14 | 2.09 | 0.30 |
| | -16 | -7 | 11.66 | 3.91 | 4.14 | 0.61 |
| | -17 | -8 | 12.88 | 7.34 | 5.55 | 1.91 |
| | -18 | -9 | 12.10 | 12.30 | 6.42 | 4.58 |
| | -19 | -10 | 10.38 | 16.20 | 6.49 | 7.34 |
| | -20 | -11 | 8.40 | 16.49 | 5.94 | 8.26 |
| | -21 | -12 | 6.28 | 12.68 | 4.97 | 6.80 |
| | -22 | -13 | 4.50 | 7.47 | 3.98 | 4.52 |
| | -23 | -14 | 3.30 | 3.95 | 3.11 | 2.84 |
| | -24 | -15 | 2.42 | 2.18 | 2.36 | 1.82 |
| Study Area 2 | -15 | -6 | 0.24 | 0.06 | 0.13 | 0.01 |
| | -16 | -7 | 0.26 | 0.07 | 0.10 | 0.02 |
| | -17 | -8 | 0.26 | 0.10 | 0.05 | 0.06 |
| | -18 | -9 | 0.26 | 0.13 | 0.05 | 0.09 |
| | -19 | -10 | 0.26 | 0.19 | 0.04 | 0.11 |
| | -20 | -11 | 0.29 | 0.26 | 0.05 | 0.13 |
| | -21 | -12 | 0.29 | 0.29 | 0.05 | 0.16 |
| | -22 | -13 | 0.37 | 0.31 | 0.07 | 0.14 |
| | -23 | -14 | 0.47 | 0.30 | 0.07 | 0.13 |
| | -24 | -15 | 0.57 | 0.34 | 0.05 | 0.13 |
| Study Area 3 | -15 | -6 | 15.01 | 5.08 | 4.98 | 1.25 |
| | -16 | -7 | 22.62 | 6.68 | 10.43 | 2.95 |
| | -17 | -8 | 33.39 | 13.65 | 22.69 | 8.61 |
| | -18 | -9 | 45.05 | 27.00 | 40.10 | 18.64 |

| | | | | | | |
|---|---|---|---|---|---|---|
| | -19 | -10 | 67.45 | 39.39 | 65.81 | 28.24 |
| | -20 | -11 | 107.82 | 48.58 | 107.26 | 40.76 |
| | -21 | -12 | 159.50 | 72.41 | 159.19 | 69.73 |
| | -22 | -13 | 200.94 | 125.85 | 200.80 | 125.41 |
| | -23 | -14 | 200.50 | 191.50 | 200.48 | 191.43 |
| | -24 | -15 | 180.63 | 210.58 | 180.63 | 210.57 |

*Table 5: Backscatter values of inundated areas. The total inundated area for VH and VV backscatter in SA1, SA2, and SA3 and the corresponding threshold values.*

### *6.2.1 SA1 Threshold*

The total inundated area of SA1 was found both with and without the SEM. The range of total inundated area was between minimum 0.3 $km^2$ and maximum 8.3 $km^2$ with SEM. Without SEM, total inundated area was between 2.1 $km^2$ and 16,5 $km^2$. Figure 26 displays flooded areas in VV and VH, including the SEM. VH threshold were set to -20 dB and VV threshold were set to -12 dB. The flood mask for VH and VV is displayed in red and blue respectively. Green colour shows areas where VH and VV masks overlap. Figure 27A and B shows flooded land around the river with more masked area in VH than VV. North of figure 27A, steeper hills are masked with the SEM. Figure 27B shows flooding further upstream in the east-part of the river. Dark green forests surround the river and display no inundation (Figures 27 A and B). Farmland and grasslands are partially covered by the flood mask both the VH and VV flood mask. 27 C shows a portion of the side valley north of the Stjørdal River, where the river Gråelva flows from north to south in to Stjørdalselva. At an elevation of 30 m.a.s.l, only the slope-part of the SEM is applied in this area, and steep parts of the river are masked, leaving out possible inundated areas from the mapping.

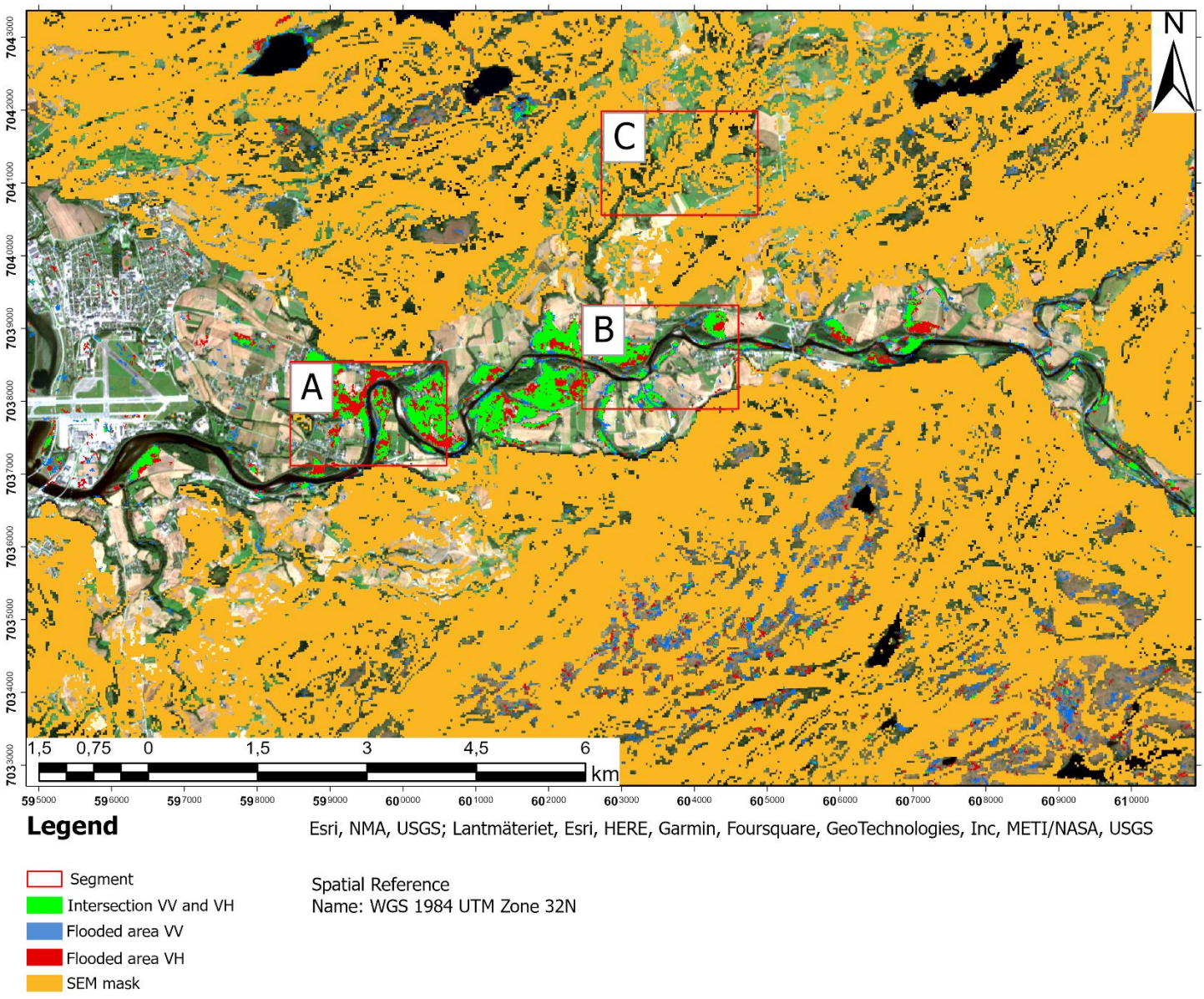


*Figure 26: Inundated areas SA1. Red areas show inundated areas detected in VH, blue areas show inundated areas detected in VV and green areas show areas where both VV and VH detects inundation. Orange areas are masked by the SEM.*

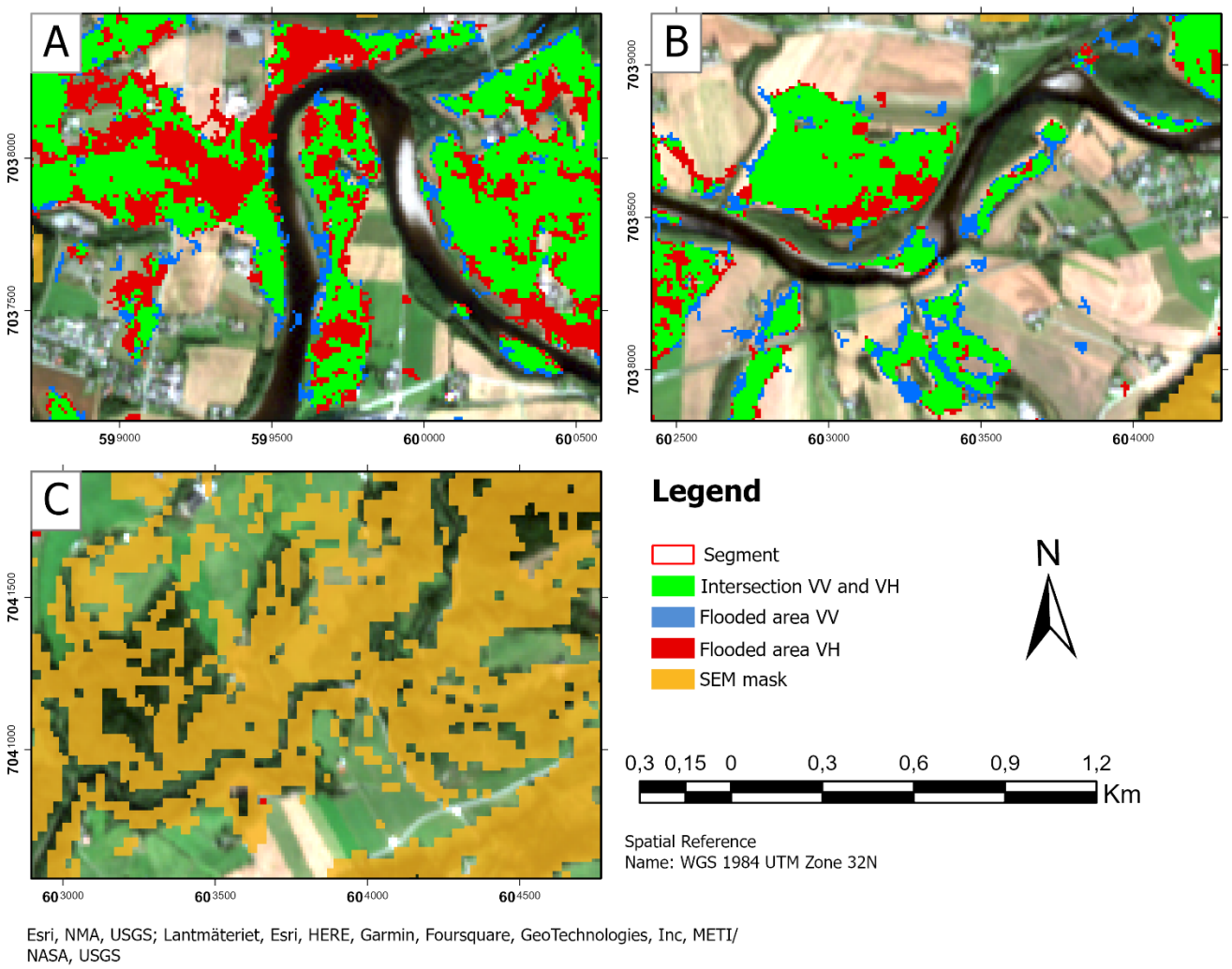


*Figure 27: SA1 Segments A-C.*

### *6.2.2 SA2 Threshold*

Calculation of inundated areas for SA2 were done with S1 backscatter imagery and S2 NDWI imagery. SEM was also used in the calculation. NDWI threshold of SA2 was set to 0 (Table 6), which corresponds well to the values seen in Figure 28. The flooded area calculated for NDWI mask was 0.44km$^2$ without SEM and 0.25km$^2$ with SEM. The flood mask for backscatter values ranged from 0.01km$^2$ to 0.16km$^2$ for VV mask without SEM and 0.06km$^2$ to 0.34km$^2$ for VV mask with SEM. The VH polarization showed overall larger inundated areas from 0.05km$^2$ to 0.13km$^2$ with SEM and 0.24km$^2$ to 0.57km$^2$ without SEM. The backscatter values with highest overlap with both the NDWI flood mask and the RGB image was -23dB for VH and -15dB for VV. Figures 28-30 displays the total area for different flood mapping methods used for SA2. VH threshold were set to -23dB and VV were set to -15dB. The orange-coloured SEM is also included in Figure 30 and covers the steep mountainsides in Sunndal. The elevation threshold for the SEM was 60 m in SA2 (Section 5.4) and the valley floor is below this limit, except for the western part in 30C, leaving slopes in and next to the river to be covered by the mask.

| Threshold | Flooded area (Km$^2$)<br>Without SEM | Flooded area (Km$^2$)<br>With SEM |
|---|---|---|
| 0 (NDWI) | 0.44 | 0.25 |

*Table 6: SA2 NDWI threshold and flooded area.*

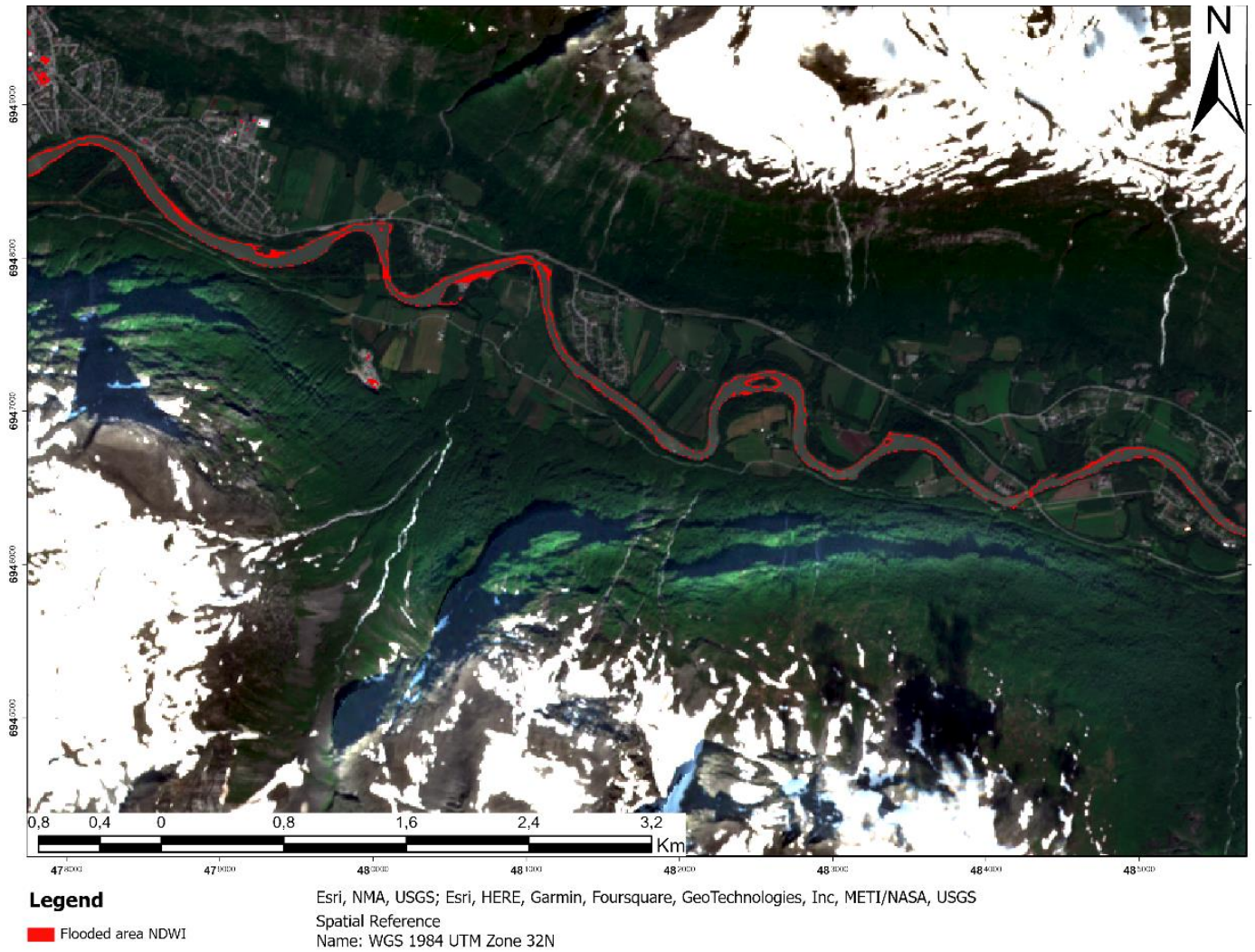


*Figure 28: SA2 NDWI flood mask.*

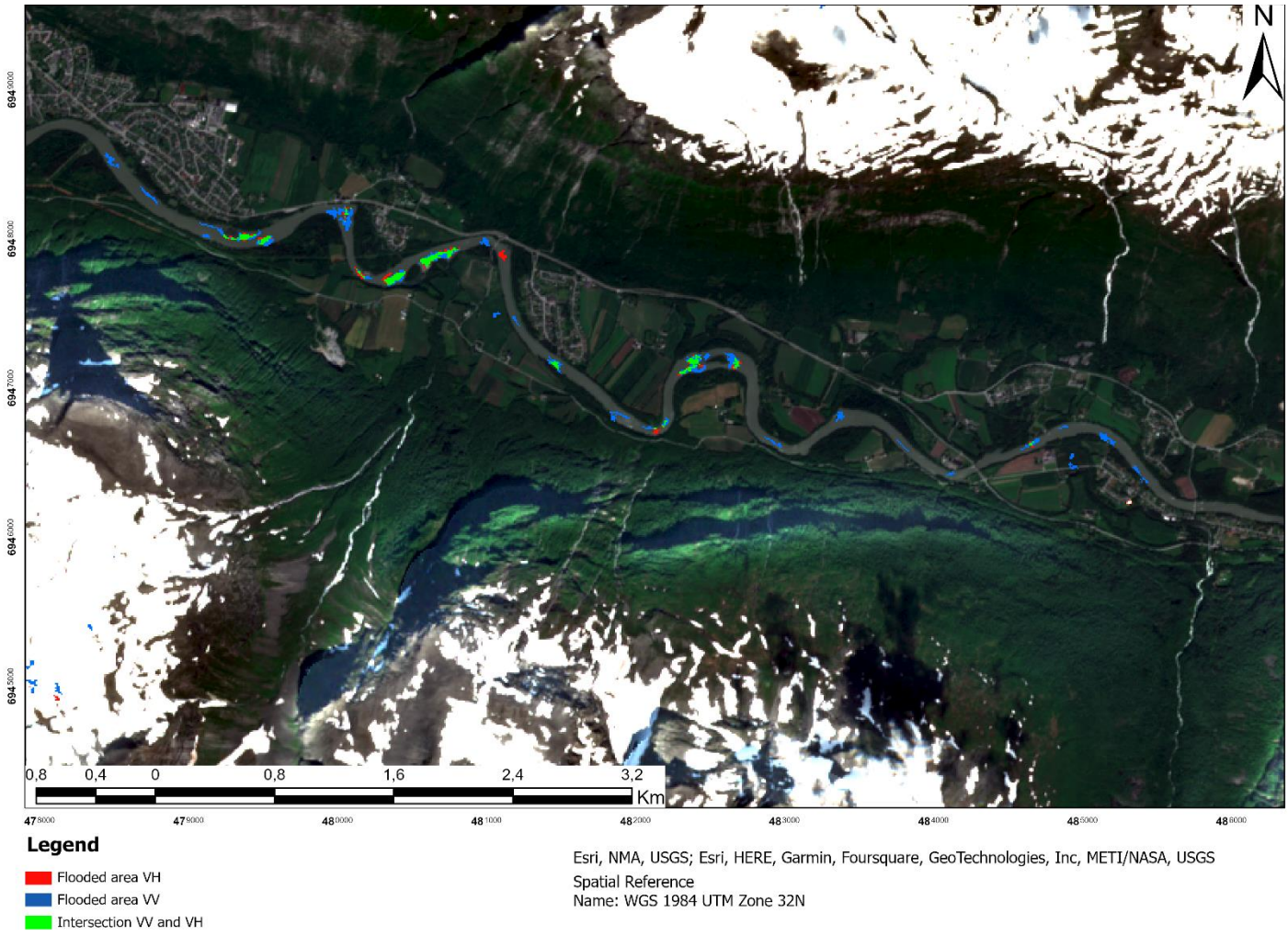


*Figure 29: SA2 SAR flood mask. Inundated areas are displayed in VH (red) and VV (blue). Overlapping areas are coloured green.*

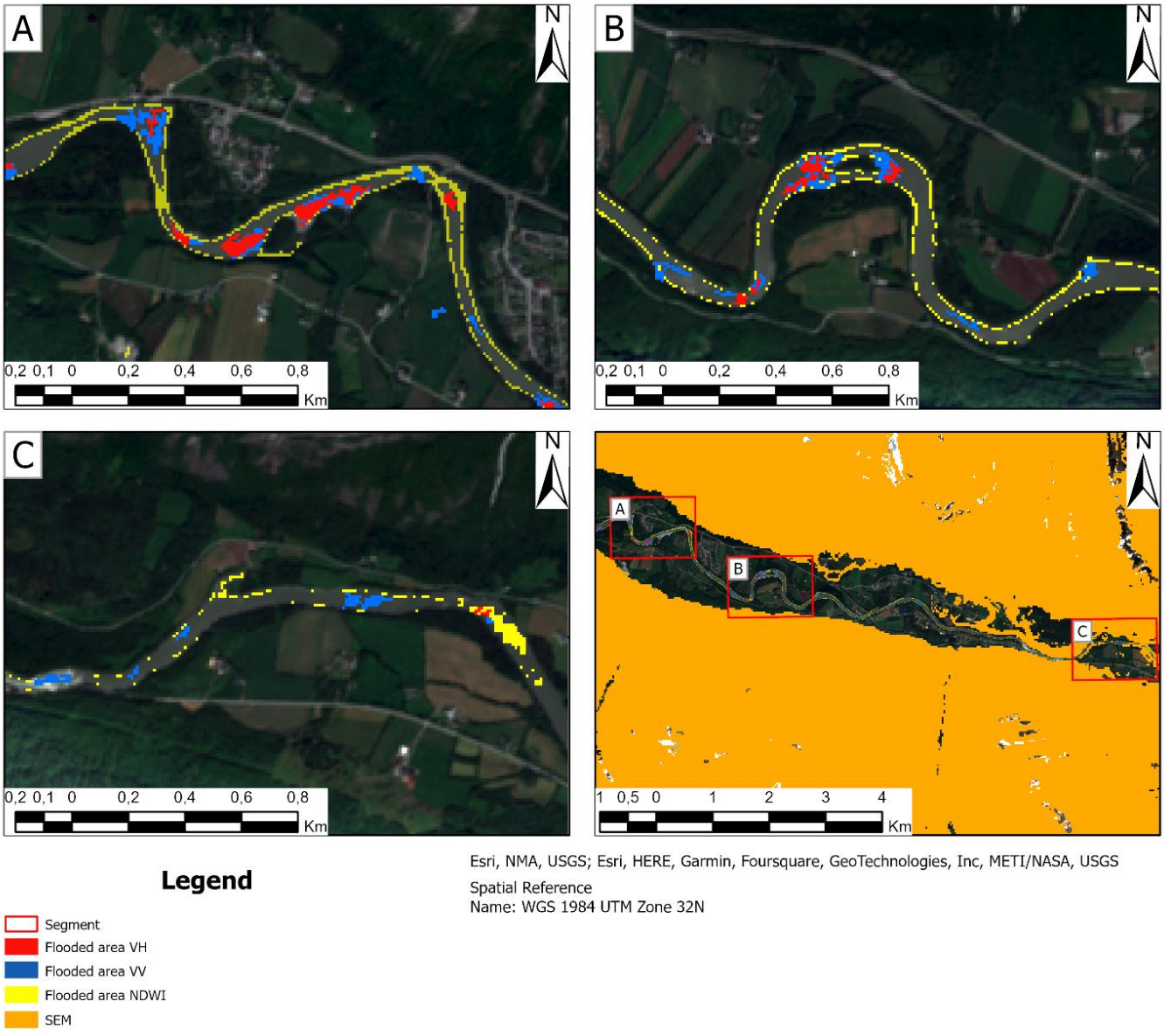


*Figure 30: Inundated areas SA2. Different colours correspond to the flood detection method. The orange mask shows the SEM.*

### *6.2.3 SA3 Threshold*

With an exception of the Tiyar mountain range on the western part of the map, SA3 shows little change in elevation and slope gradient. Flood thresholding with or without SEM shows minor changes in total inundated area. The area investigated in SA3 was much larger than SA1 and SA2. GEE was not able to calculate total flooded area of SA3 with 10m pixel size. Therefore, the calculations for total inundated areas in SA3 were done with 30m pixel size. This was done with the "scale" option, which allows pixel size of the output data to be changed. Overall, both NDWI and ratio flood mask results showed larger inundated areas. Capturing a total inundated area of over 200km$^2$ in S1 imagery, SA3 shows a noteworthy increase in scale compared to SA1 and SA2 (Table 7).

| Threshold<br>NDWI | Flooded area (km$^2$)<br>Without SEM | Flooded area (km$^2$)<br>With SEM |
|---|---|---|
| -0.1 (NDWI) | 536.26 | 479.4 |
| 0.79 (Ratio) | 565.73 | 505.39 |

*Table 7: SA3 S2 Threshold values and subsequent area sums.*

Figure 31 shows the backscatter flood mask and threshold of -23dB in VH and -15dB in VV. The RGB image was included as background. The mask covers areas around the Indus River. RGB and SAR imagery indicate different flood sizes, and some of the differences are likely a result of the images being captured on different dates. While S1 imagery was captured August 29$^{th}$, S2 imagery was captured on the 31$^{th}$, possibly closer to the flood peak.

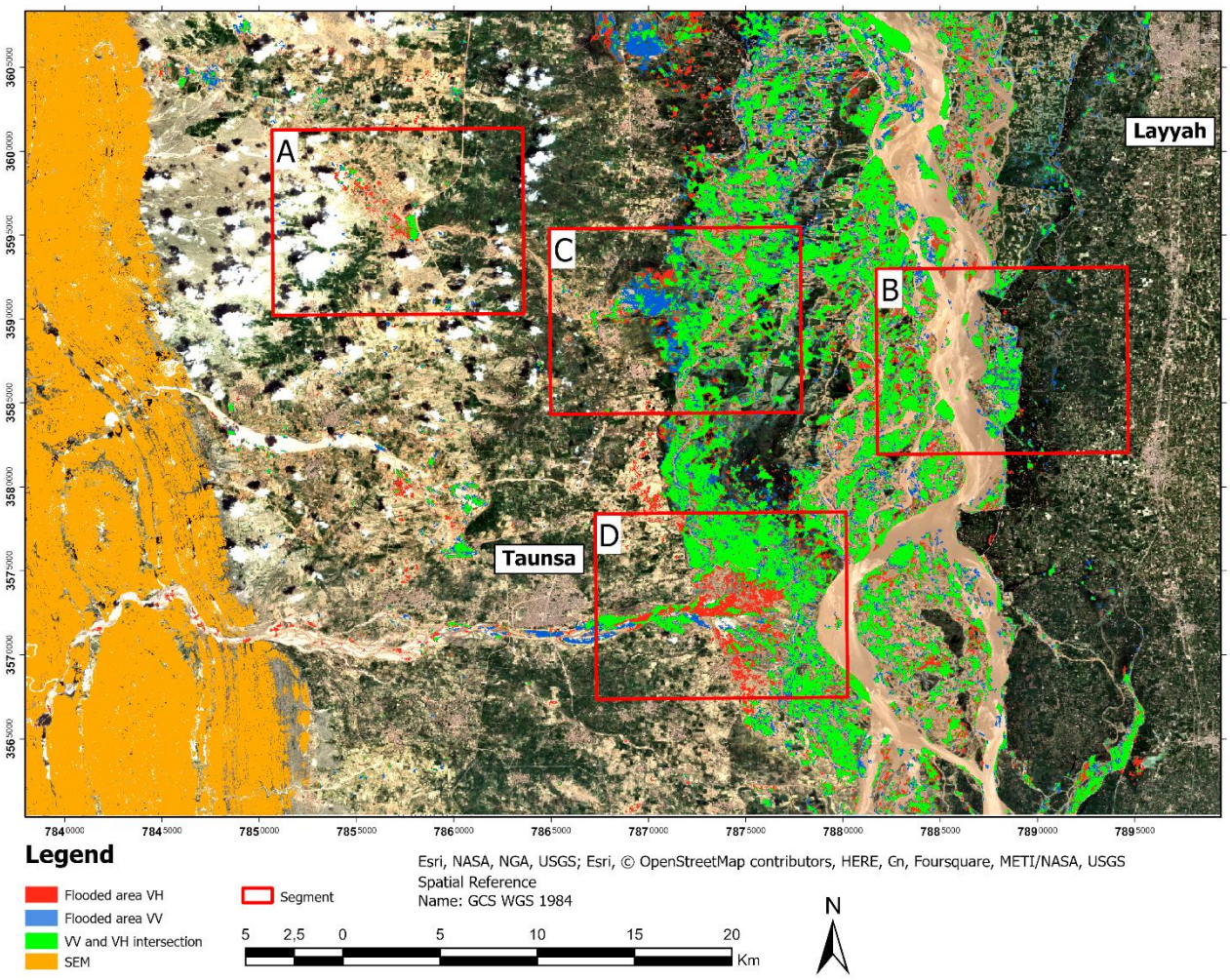


*Figure 31: Layyah backscatter flood mask. Total inundated areas in VH (red) and VV (blue). Overlapping areas are coloured green.*

Figure 32 displays the NDWI and Ratio flood mask. The Ratio mask covers an area of 505 $km^2$ and the NDWI covers 479 $km^2$. Showing the overlap where both methods detected floods, the green mask is dominant compared to the red and blue mask. Figure 33 displays segment A-D of Layyah and the NDWI and Ratio flood masks. Figure 33A shows flooding near the Chasma right bank channel, with clouds also covered by the flood mask. A noticeable difference between the optical and radar methods for mapping is displayed by the masked clouds shown in Figure 33A. The brown floodwater flows east from the Chasma River and overflows the city of Nari Shumali (Figure 33A and 33C). NDWI and Ratio flood mask were unable to detect flooding in this area. The flooding next to Nari Shumali were undetected, yet a larger area on the right-side of figure 33C were detected as flooded. Despite the colour difference of the water seen in Figure 24C, both the NDWI and Ratio managed to successfully detect flooding in the

area. Figure 33B displays the right-edge of the floodwater next to the Indus, where the road borders the final extent of the river eastward.

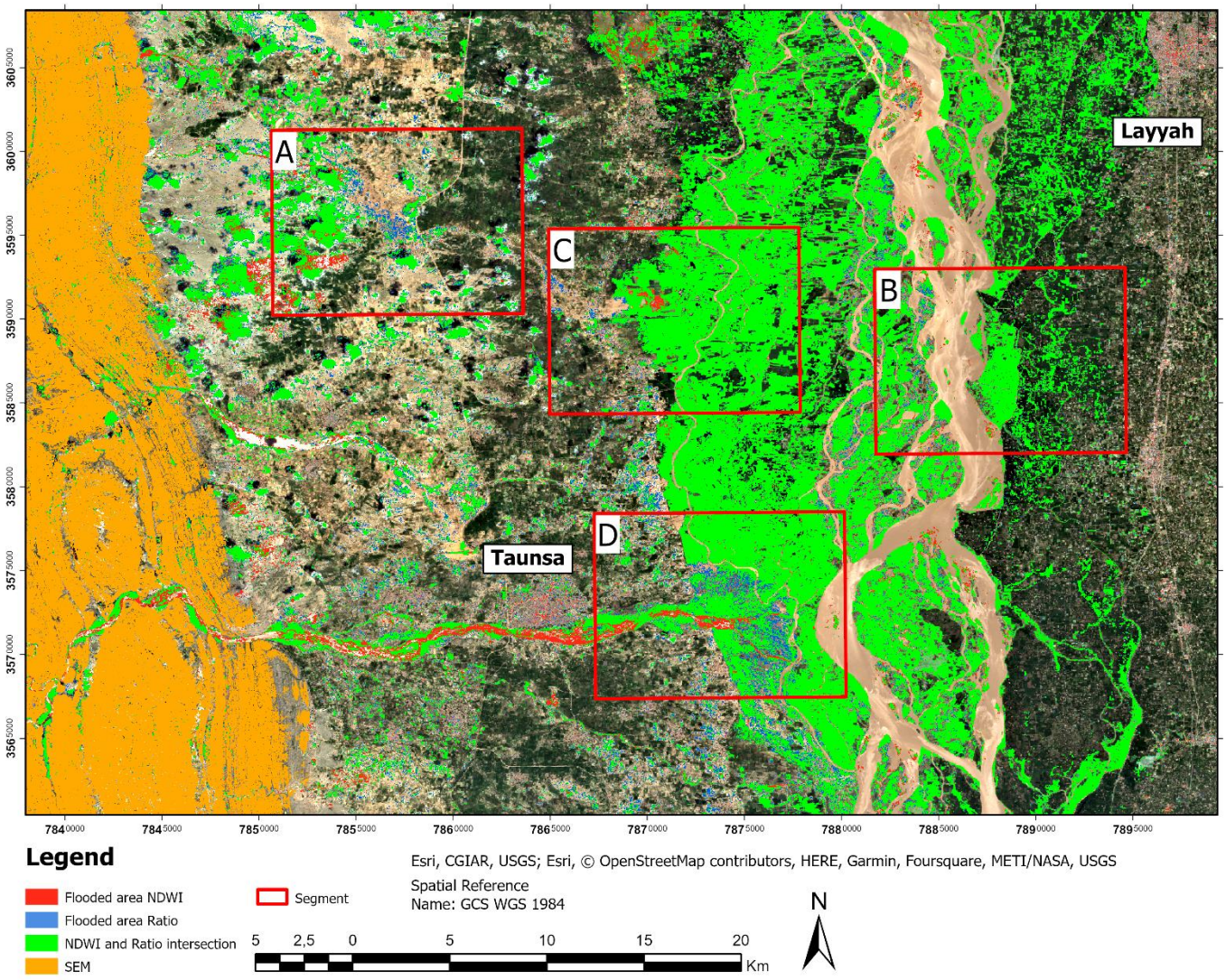


*Figure 32: NDWI and Ratio mask of SA3.*

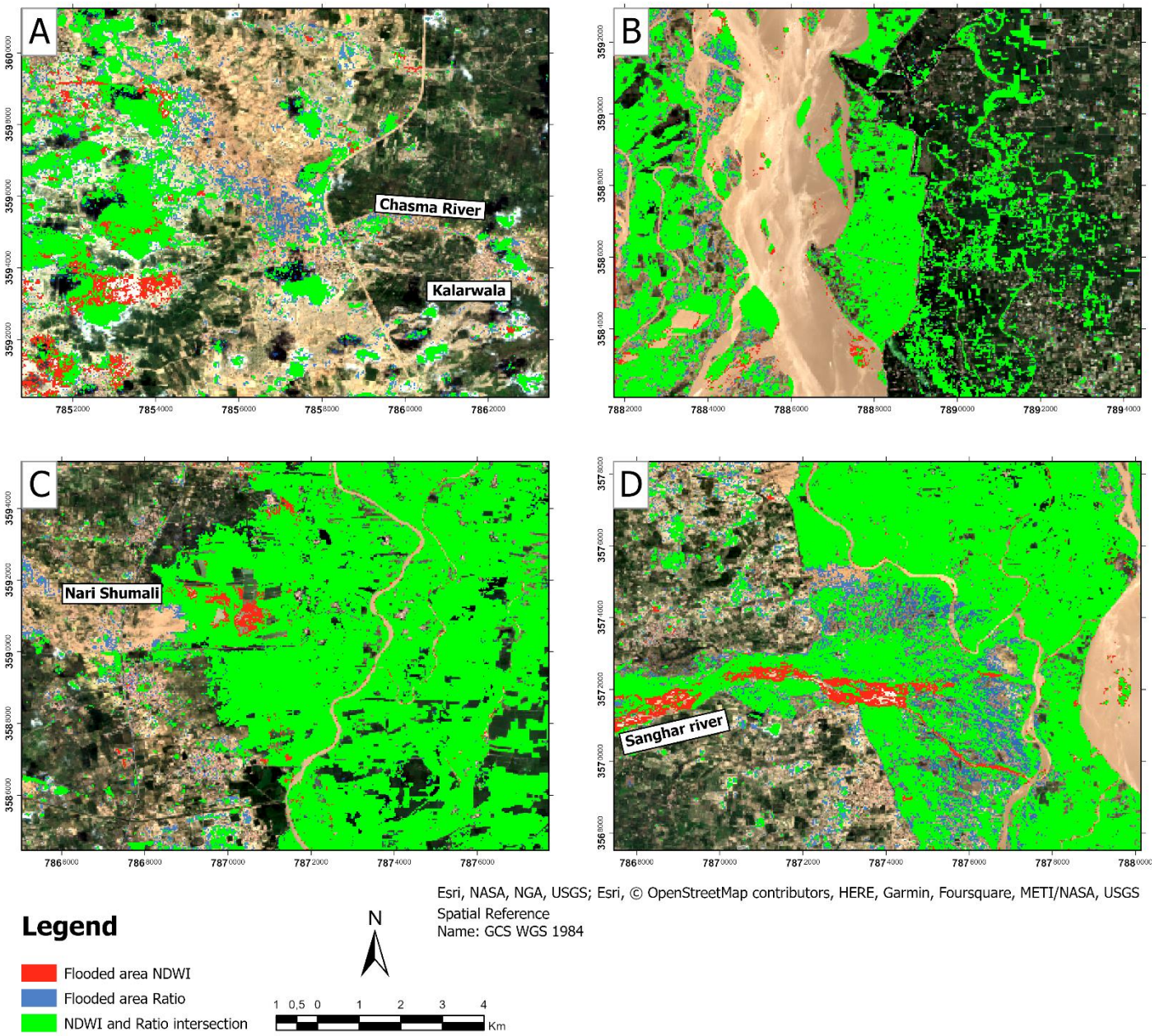


*Figure 33: Segments A-D with optical flood mask.*

The S1 flood mask is displayed in Figure 34A-D. Floodmask overlap in VV and VH were detected in each segment. 34A displays the S1 mask penetrating cloud cover. Little flooding was detected in the smaller east-flowing part of the Chasma channel. 34C shows contrast between the VV and VH masks. In the area where water colour changes from mud brown to blue (Section 6.1.3), VV successfully detects flood while a smaller part is detected in VH. In 34D, a large part of the Sanghar River is masked as flooded in VH.

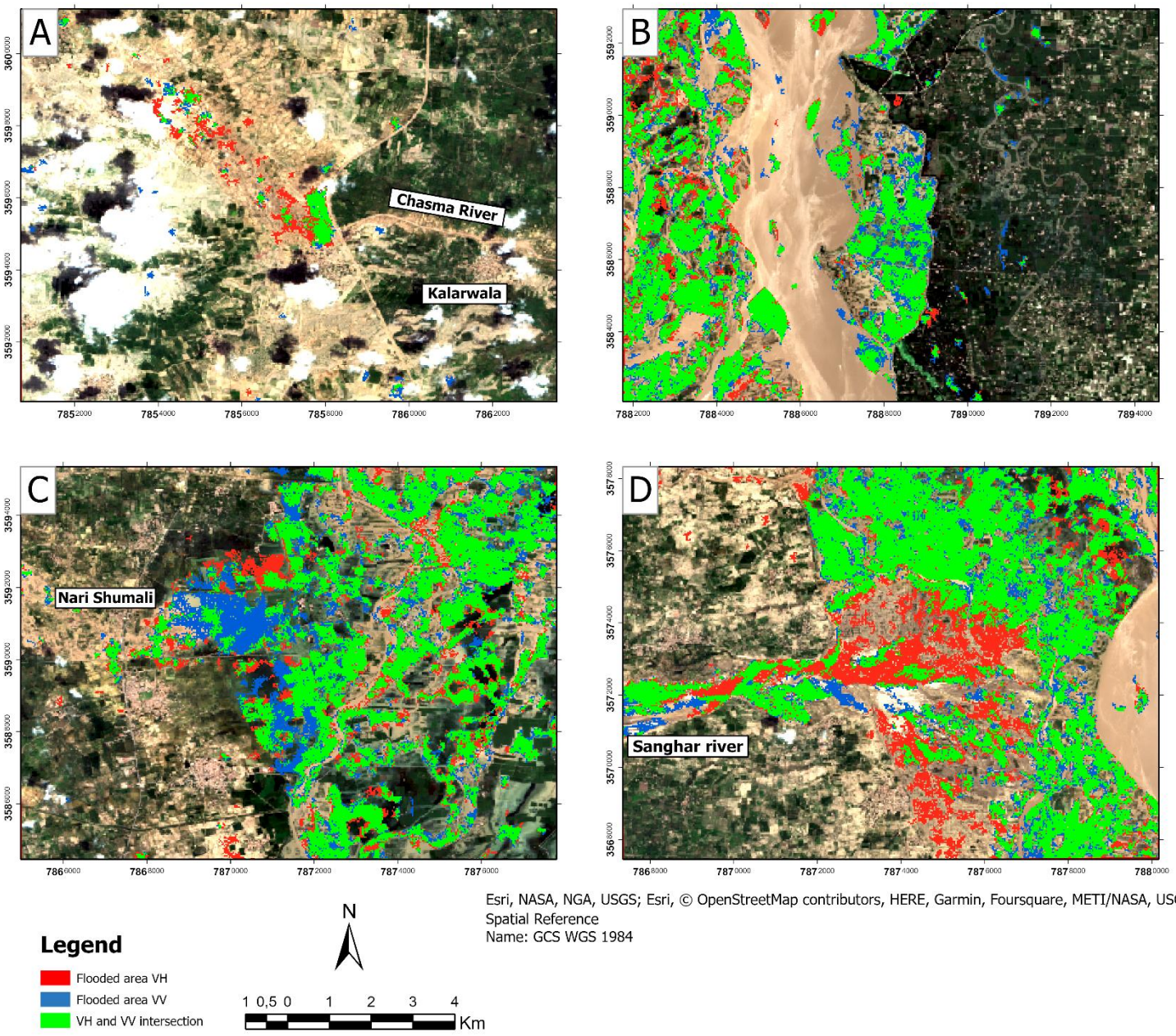


*Figure 34: Segments A-D with SAR flood mask.*

## 6.3 Method comparison

### *6.3.1 SEM Comparison*

In Table 8, the SEM coverage is presented as a percentage of the area initially classified as flooded, before being removed by the slope and elevation mask. Threshold values for S1 imagery are given respectively for VV and VH: -12dB and -20dB for SA1, -15dB and -23dB in SA2 and -15dB and -23dB in SA3. The value for NDWI was 0 for SA2 (Section 6.2.2). SA3 has a threshold value of -0.1 and a ratio threshold of 0.79 (Section 6.2.3). The highest percentage of 91.22% coverage in VV were found in SA2. SA3 displays the smallest changes between SEM and the total area, where VV and VH masks had negligible change. The comparisons for SA1, SA2 and SA3 are plotted in Figure 35.

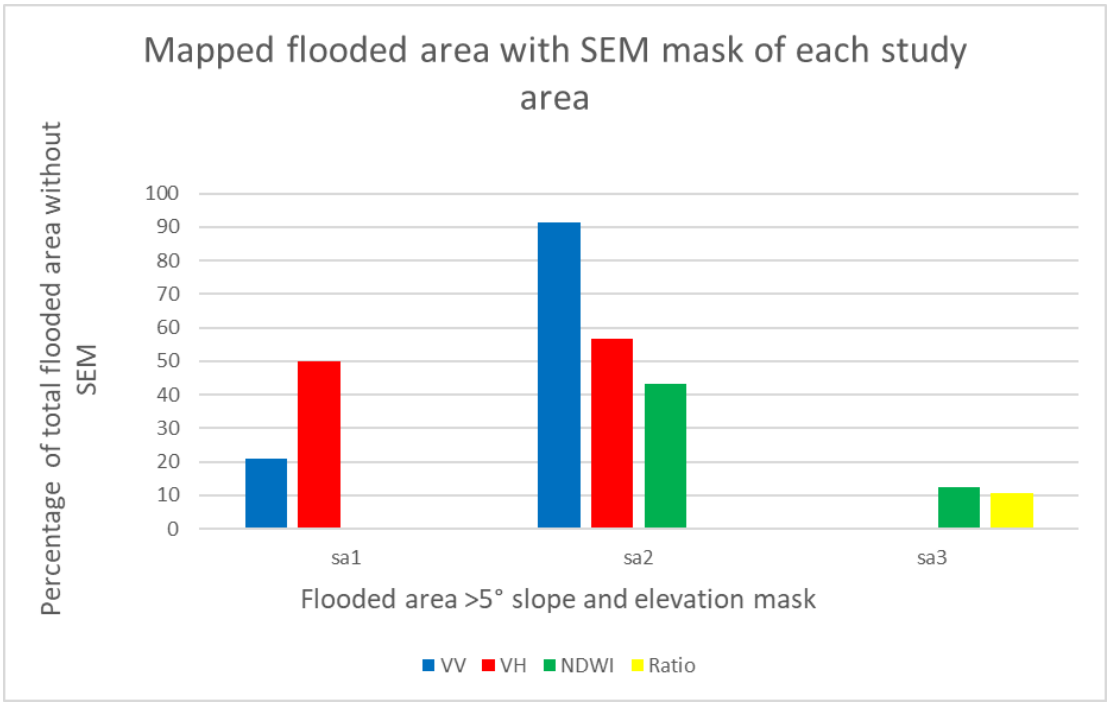


*Figure 35: Comparisons of flood detection method, SEM and the corresponding study area.*

| Detection method | SA1 | SA2 | SA3 |
|---|---|---|---|
| VV | 20.9 % | 91.2 % | 0 % |
| VH | 50 % | 57.7 % | 0 % |
| NDWI | | 43.2 % | 12.2 % |
| Ratio | | | 10.7% |

*Table 8: Mapped flooded area with >5° slope and elevation mask. Each value corresponds to the percentage of the total flooded area. Backscatter values are given respectively in VV and VH. - only one number after decimal*

### *6.3.2 Flood Mask Intersection*

For each study area, overlap between S1 VV, VH, and S2 flood masks, were calculated. Since SA1 did not include the NDWI flood mask, only VV and VH intersection were calculated for this area. For SA1, the intersection of VV and VH masks were 2.46 $km^2$, making up 36 % of the VV flood mask and 41 % of the VH flood mask.

In SA2, intersection of VH and VV were 0.002 $Km^2$, which is 2 % of VV and 3 % of VH. The VV and NDWI intersection mask were 0.03 $km^2$, 22 % of VV and 12 % of NDWI. Intersection of VH and NDWI mask were 0.01 $km^2$, making up 4 % of NDWI and 14 % of VH.

SA3 includes intersection of the ratio imagery also. Intersection of VH and NDWI mask was 479.4 $km^2$, making up 36 % of NDWI and 87 % of VH. Intersection of VV and NDWI mask was 179.44 $km^2$, amounting to 85 % of VV and 37 % of the NDWI. Intersection of Ratio and VV mask was 180 $km^2$, which is 86 % of VV and 35 % of Ratio. Intersection of Ratio and VH mask was 179 $km^2$, and 89 % of VH and 35 % of Ratio. Intersection of Ratio and NDWI mask was 444 $km^2$, which is 86 % of the Ratio mask and 93 % of the NDWI mask.

| Study area | VH and NDWI intersection ($Km^2$) | VV and NDWI intersection ($Km^2$) | VV and VH intersection ($Km^2$) | Ratio and NDWI | Ratio and VV | Ratio and VH |
|---|---|---|---|---|---|---|
| SA1 | | | 2.46 | | | |
| SA2 | 0.01 | 0.03 | 0.002 | | | |
| SA3 | 173.58 | 179.44 | 156.57 | 443.71 | 180.26 | 178.8 |

*Table 9: Flood mask intersections. Values show total area intersected between two detection methods, measured in square kilometre.*

### *6.3.3 Flood Mask and Vegetation*

Vegetation was found in each study area. Figure 36 displays combined flood masks of each study area and the surrounding land consisting of agricultural land and vegetation. Noticeable areas of dark green are likely dense forest where the detection methods are unable to detect flooding. Figures 36A-B display SA1, with VH and VV flood mask. Areas with dark green is found around the river, and is not covered by the mask. Figures 36C-D shows SA2 with S2 and S1 flood masks combined. Similarly to SA1, dark green forests are found around the river and free of any flood mask. Figures 36E-F shows SA3, with S1 and S2 flood masks. Figures 36E-F display agricultural land and vegetation, forming square and rectangular shapes within the flood mask.

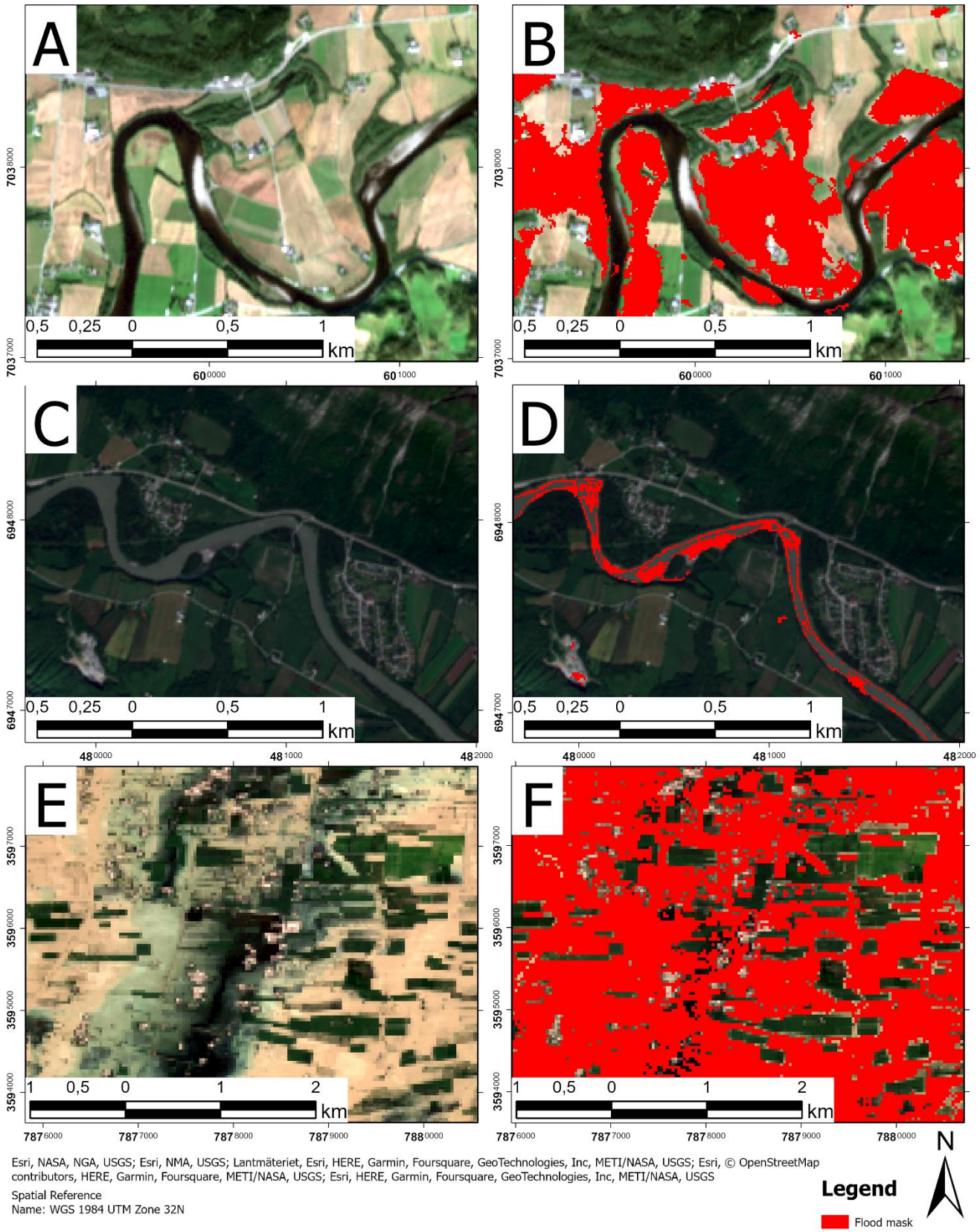


*Figure 36: Flood mask comparison of SA1, SA2, and SA3. Figure A: SA1, no mask. Figure B: SA1 with flood mask. Figure C: SA2, no mask. Figure D: SA2 with flood mask. Figure E: SA3, no mask. Figure F: SA3, with flood mask*

# 7. Discussion

In this chapter, the results of each study area and the implemented methods are discussed.

## 7.1 Filtering Options

### *7.1.1 Reference Stack*

Flood detection that relies on orbiting satellites are constrained to specific timeframes, where the time interval of the satellite matches the time interval in which the flood takes place. Additionally, flooding varies where upstream areas flood prior to the downstream. Peak floods for larger areas can be difficult to acquire, as the time and region of interest of the peak in one area might differ to the large-scale flood and other areas affected by the same weather event. SA1 and SA2 were flood events in Norway. Although a large flood in Norway, the Gyda flood only lasted for three days in Stjørdalen, and flooding in Sunndal lasted for five days. Floods that last five days or less are problematic as the S1 and S2 orbit times are 12 and 10 days respectively or six and five days if both satellites are included. Flood duration would be over 6 days to guarantee inclusion of both S1 and S2 imagery. Land surface that stays inundated over longer periods would contain several S2 images, leaving the option to choose between possible cloud-free or less cloud covered flood imagery. In Pakistan, the 2022 flood occurred because of monsoon and glacier melt that lasted for months. Long flood durations, such as the Pakistan flood allows for several coverages of the flood in S1 and S2 imagery.

Additional constraints of the reference stack were found in orbit filtering. Selecting single orbit track and number of the S1 reference stack, reduced the number of images used for reference. Consequently, this filtering reduced temporal resolution in the S1 reference stack.

### *7.1.2 Pixel Resolution*

The scale parameter in GEE is an important tool as it specifies the pixel resolution of the image. While spatial resolution explains the minimum pixel size available for the image, scale determines the level of detail applied to the image during processing (GEE Guides, 2021). This detail specification is important in investigations of pixels, such as flood area calculations.

Figure 37 display pyramiding of an image and subsampling by removing pixels until the desired scale is reached. In this study, the scale was determined when exporting and calculating inundated area extents. Pixel resolution captured on S1 and S2 imagery were initially 10x10 m, but later changed to 30x30 m for SA3, while SA1 and SA2 kept the original size. Pixel resolution were changed for SA3 due to processing problems on 10x10 m, and the image had

slow loading time. The resulting image and calculations of 30x30 m were less accurate with possible over or underestimations of flooded area. Further increase to e.g., 100x100 m would further reduce the accuracy of flood area sizes (GEE Guides, 2021).

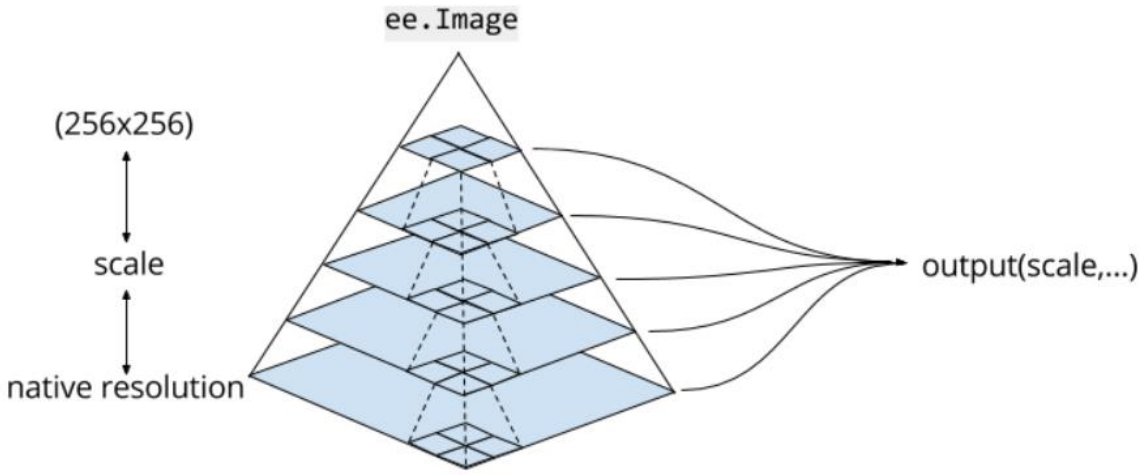


*Figure 37: Interpretation of pyramiding of four pixels on GEE. Scale is specified at the output. Source: GEE Guides, 2021.*

### *7.1.3 Separated Pixels and Pixel Filtering*

Pixels interpreted as flood were filtered by a pixel removal algorithm and flood pixels connected with less than 8 other flood pixels were removed (Section 5.5). The resulting images provided by the algorithm became less speckled, and most of the areas detected as flooded were larger inundated areas. For each of the study areas, separated pixels were found to a large extent around the entire image. Although the removal resulted in a less speckled image, SA2 lost valuable information. While the NDWI mask noticed the change in river width, SAR imagery lost most of this information (Figure 38). The lost information was highlighted by the low intersection between NDWI and S1 imagery (Section 7.1.3). Prior to the pixel removal, reference images in VV and VH were also filtered by the refined lee algorithm, which could further reduce details (Lemoine, 2018) (Section 5.1).

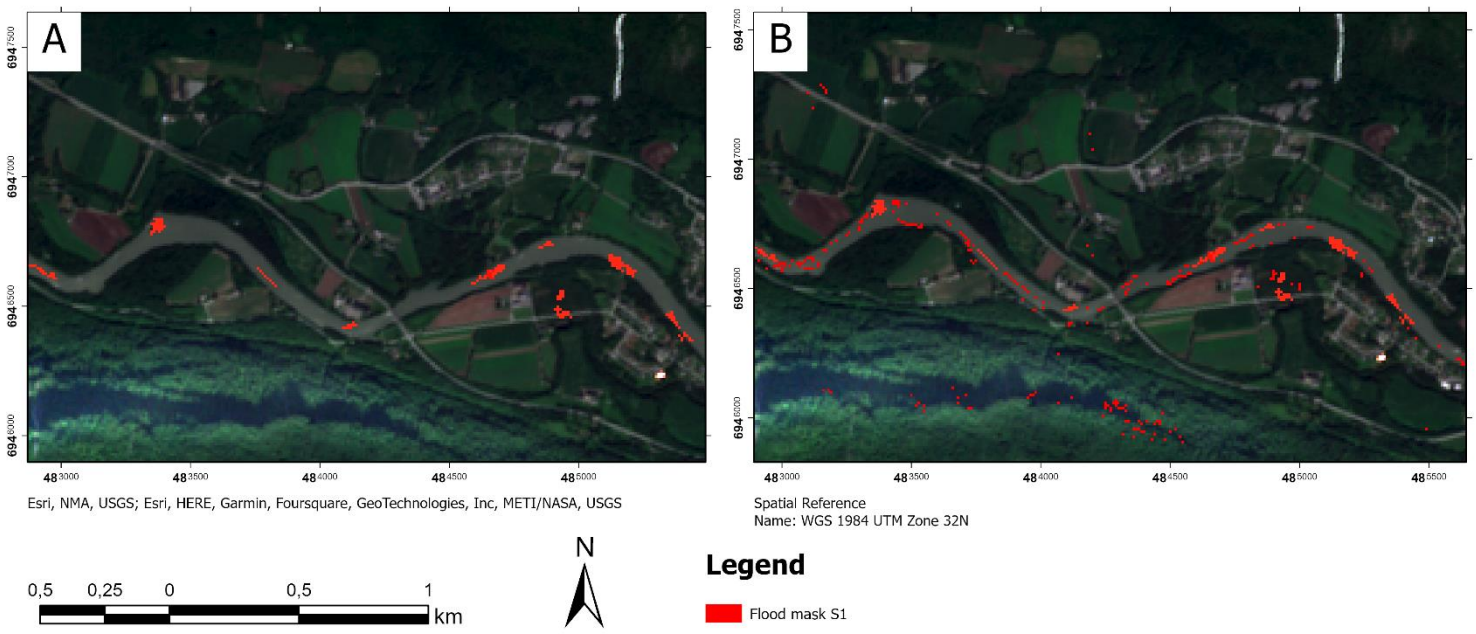


*Figure 38: differences between flood masks using A: no pixel removal and B: final product with pixel removal.*

## 7.2 Identifying Challenges and Effective Solutions

### *7.2.1 Incidence angle*

Floricioiu et al. (2001) found the backscatter coefficient of different surfaces to be affected by the incidence angle. For most natural surfaces, the VV and VH polarizations decrease as the incidence angle increases (Floricioiu et al. 2001). Changing incidence angles on the three study areas results in different backscatter on surfaces including water, vegetation, rocks, and snow (Section 3.2). The flood mask will also vary based on the changing incidence angle. When the scattering effects on water surfaces changes, the threshold will also change. The three study areas are located in different places with different orbit numbers. As the incidence angle varies depending on location, backscatter coefficient of the three areas is likely to differ. S1 has an incidence angle range of 29 - 46˚. The sensors used in the study by Floricioiu et al. (2001) has large range. However, backscatter coefficient will likely change as the incidence angle changes from 29˚ to 46˚.

### *7.2.2 Shadow effect and clouds*

Shadow effects appear in remote sensing often because of clouds or terrain. In MSI optical remote sensing, shadows could pose a problem, as clouds could misclassify or obscure different

land cover types (Bazilova et al. 2022; Fischer, 2015). In the case of flood mapping, if the cloud shadow is within a similar pixel threshold range as the water surface, the shadows are misclassified as flooded area. In SA3, misclassifications of inundated areas from cloud shadows were displayed in both the NDWI and Ratio mask. To reduce or remove these effects, this study used two different approaches in order to improve the data. The first approach was to include S1 imagery, in addition to the optical imagery. With long wavelength imagery, such as the C band, clouds, cloud shadow, and darkness during night has little to no interference with the inundation mapping (Pohl et al. 1998; Hall, 1996).

The second approach was to use the "CLOUDY_PIXEL_PERCENTAGE" property of S2 level 2A to reduce cloud cover to 30 %. With the use of S2 level 1C, cloud removal algorithms can create cloud-free and shadow-free reference images, increasing the accuracy of the detection methods (Chen et al. 2018). This was used for all images in the S2 reference stack. With the use of 30 % filter, some clouds could remain in the image, and inspections of the reference images were needed. In addition, level 2A is not able to remove all cloud pixels and some cloud types and atmospheric gases has lower accuracy in pixel removal (Chen et al. 2018).

### *7.2.3 Terrain Distortions*

Flood detection of SA1 demonstrates how SAR is an effective tool when the earth is covered by clouds. Although S1 outperforms S2 imagery in situations where clouds obstruct the earth's surface, it struggles to perform in rugged terrain where terrain distortions can appear. This problem is seen in SA2, where the steep mountainsides experience strong shadowing effects on the north- and east-side of the mountains. The south and west-facing sides experienced foreshortening and layover effects (Section 6.1.2 and 3.1). These distortions could cause misinterpretation or underestimations of the flooded area.

Reduction of these effects was done in two steps with ancillary data. The first step was done using S1 data for reference images acquired in corresponding orbit pass track as the flood images to avoid distortion effects caused by changing sensor view angles (Section 5.1, 5.2). The second step was the use of digital surface model AW3D and the thresholds set by the SEM (Section 5.5). Demonstrated in Section 6.2, both steps improved the quality of the flood detection, where shadowing in rugged areas were partly or fully removed in the calculation of the flood mask. Previous studies with the use of DEM to remove mountain shadow effects have been tested with the Shuttle Radar Topography Mission Digital Elevation database (SRTM) (Lin et al. 2019) and HydroSHEDS (Wang et al. 2022). In both studies, a threshold of 5-degree slope was used. HydroSHEDS is based off elevation data obtained from SRTM. While AW3D

uses the PRISM sensor for DSM mapping, AW3D includes SRTM as reference information in quality validation (Takaku et al. 2014). A study by Trisakti et al. (2010) showed that although PRISM has a higher spatial resolution, both elevation models have similar elevation and distribution patterns.

In a study comparing four different SAR-based flood mapping approaches, the TanDEM-X approach used STRM DEM to remove radar shadows and reduce misclassifications (Martinis et al. 2015). In this study, slope threshold of the SRTM DEM were set to 20 degrees, meaning slopes higher than this threshold was removed from the flood mask. The threshold was set to 20 on the account that smaller slope threshold would lead to higher misclassifications between two different water mapping products. Although the study by Martinis et al. (2015) concludes that 20 degrees gives the best results for slope threshold, it is worth noting that TanDEM-X comprises of an X-band sensor. The wavelengths of the X-band signal are smaller than the wavelengths of the C-band satellite used in this thesis and the study by Wang et al. (2022). Additionally, polarization of the X-band satellite was in HH, and with a different incidence angle, it would produce different results than S1 in mountainous terrain.

#### *7.2.4 Snow Cover*

A snowpack experiences scattering at different depths where boundaries between different layers appear, such as: surface scattering at the air-snow boundary, volume scattering inside the snowpack, snow-soil scattering and volume-surface scattering (Floricioiu et al. 2001) (Section 3.1). Additionally, the main scattering effect changes between wet and dry snow. For instance, the C band SAR can penetrate dry snow cover up to 20 m. However, this differs from wet snow with only around 3 cm penetration depth (Tsai et al. 2019). In these situations, the backscatter mechanisms will change from mainly volume scattering in dry-snow conditions, to single-bounce scattering. Given that such conditions could affect changes seen on surface backscatter, and captured images of SA1 and SA2 were snow covered (Section 6.1.1-6.1.2), the impacts snow could have on flood thresholding should be considered.

Section 6.1.1 details the potential misclassification that would occur if reference image were given over a period during winter. The alternative date range of November to January would include snow cover on the ground and some flooded areas could instead be misclassified as permanent water bodies. The misclassification would happen if backscatter values of the snow were similar or lower than the flood values. In such cases, the resulting flood mask would cover a smaller area. The flood imagery of SA1 were captured on January 13$^{th}$, and optical imagery was not obtainable in this period. However pictures and news articles of the Gyda flood in

Stjørdalen (Section 2.1) suggest backscatter interpreted as flood were unlikely to be wet snow misclassified as water surfaces.

SA2 went through melting in the form of summer heatwave and similar conditions were likely met for the snowpack in this area also. S2 imagery were also available for this area, and snow is seen on the mountaintops in both reference and flood imagery of SA2. The snow-covered mountaintops of SA2 were situated in steep areas and therefore removed by the SEM. Bazilova et al. (2022) tackled water mapping in snow covered areas by using optical band ratio imagery and min and max reflection values of annual reference stacks. In this study, neither ratio nor annual reference stacks were used to avoid snow cover misclassification. Instead, the SEM which were used to avoid backscatter misclassification of mountain shadow ended up being serendipitous in also removing large snow-covered areas of SA2 flood mask. Regarding SA1, flood detection using optical images was hindered by cloud cover, making it impossible to apply NDWI thresholding. However, if similar methods are used for mapping new study areas, the SEM may not be effective in handling snow cover. In such cases, the approach proposed by Bazilova et al. (2022), which uses ratio imagery instead, could be more suitable.

#### *7.2.5 Vegetation*

Vegetation can obscure or completely remove vision of the land surface, hiding potential flooded areas. Dense vegetation can be found near the rivers of SA1 and SA2, which blocks the visibility of water underneath the canopy. Several studies have found that the C-band were able to penetrate short branching and less dense vegetation, but it is unlikely to penetrate high density tree types, such as spruce and birch (Landuyt et al. 2020; Chiu et al. 2000).

Section 6.3.3 compares the different threshold methods for each study area where areas of dense vegetation are unable to be classified as flooded. For SA1 and SA2 these areas are likely to be dense vegetation of either spruce, pine or birch, which is some of Norway's most common tree types (NMCE, 2020). SA3 is in Pakistan which contains a large variety of tree types and biomes. In SA3, vegetation is in the form of both natural vegetation, such as trees and shrubs, in addition to agriculture and crop land. Vegetated areas in SA3 are found within the flooded region of the Indus where the flood mask is unable to penetrate. These areas are agricultural land, and they are displayed on the map with a rectangular or square outline within the flood mask. While some agricultural land is not detected as flooded areas, other areas around have been detected as flooded. Changes between areas mapped as flooded and not flooded agricultural land could

be the result of different vegetation planted for each area or different growth stages of the similar plant. While different bands experience different levels of scattering on vegetation, common mechanisms in each band (X, C, L, etc.) results in increased backscatter signal (Huang et al. 2022).

Possible ways to detect open waterbodies with SAR have been proposed by Martinis et al. (2015). Martinis et al. (2015) proposed the use of X band, instead of longer wavelengths, creating a higher contrast between land and open water. Features on land that could appear smooth, such as deserts or flat uncultivated land, would experience more diffuse scattering in comparison to water features. Such contrast would not be seen for longer wavelengths, such as the C band. In shallow water with partially submerged vegetation, long wavelengths produced in the L band could effectively detect flooded areas (Martinis et al. 2015). Although L band appears to be better choice, other bands such as VV polarization in C band have been found to identify partially submerged features (Manjusree et al. 2012).

In this study, only the C band were available for use in flood detection and the option between VV and VH polarization left different results. Twele et al. (2016) found that the contrast between vegetation and water surfaces were greater in the VV polarization than VH, due to strong backscatter signals, such as double bounce. The study also found a higher penetration depth into vegetation in VV than VH. VH were also found to have more variability of backscatter when the signal encountered vegetation. The study also found that VH were more sensitive to volume scattering on vegetation, and it experienced lower backscatter values for open areas, such as agricultural land. This led to more misclassifications between water surfaces and other low-value surfaces such as agricultural land, in VH than in VV.

Given the amount of agricultural land found in each study area of this thesis, and similar conditions were found in the study by Twele et al. (2016), results of this thesis could experience similar misclassification problems. Although most agricultural land in this thesis saw little change in backscatter value between reference image and flood image, ideal VH and VV threshold had to be chosen carefully.

#### *7.2.6 Water Colour, and Contrast*

In areas where water has large changes in spectral reflectivity, the detection methods of both S1 and S2 struggles. This was seen in several areas in SA3, where changes between brown and green water were frequent. The contrasts where NDWI values changes from negative to positive

(Section 6.1.3) represents change from turbulent to calmer waters and a change in concentration of suspended sediments (Meena et al. 2021). Recommended NDWI interpretations of flooded land by EOS, (2021) were poor for SA3. Consequently, the NDWI threshold value was set to -0.1 and made the flood mask capable of detecting some muddy water. Still, areas such as flooding near the Chasma canal were not detected. Similar results were found in Ratio imagery, and lowering threshold values more lead to dry land being misclassified as flooded areas.

As stated by Bazilova et al. (2022) (Section 3.2), NDWI could be replaced by Ratio imagery to enhance differences between dry land and water. However, Ratio would also make the image coarser and less detailed. Several studies have proposed to use SWIR in different indices, such as NDWI and Ratio imagery in turbid water (Amarnath, 2014; Bazilova et al. 2022). Meena et al. (2021) used the NDTI, and Normalized Difference Chlorophyll Index (NDCL), in addition to NDWI, to detect turbulence and debris filled waters.

SAR flood detection does not experience this problem, but problems arise where differences between turbulent water and still water are found (Section 3.1). Choosing between polarization could affect results when detecting turbulent flood water (Section 3.1). Still, small differences seen on water bodies mapped over large areas brings problems in the mapping as this study uses one simple threshold for the entire area. Choosing the correct threshold to mask flooded areas under these circumstances are crucial and small changes would likely bring out large differences in the results.

## 7.3 Flood Detection Method Comparisons

Threshold values of S1 flood masks were based on VV and VH ranges found on different incidence angles by Manjusree et al. (2012) (section 5.2). Results of VH backscatter showed generally higher contrasts between dry land and water bodies than in VV. Differences between the polarizations have been found in other studies (Huang et al. 2022). While VV have been found to give stronger return signals in specular and double bounce scattering, VH have been found to give stronger return signals in volume scattering (Jo et al. 2018). Intersections between VV and VH showed large differences between the two flood masking methods (Section 6.3.2). In SA1, VH showed greater contrast on flooded areas and dry land. VV showed a large backscatter range on the floodwater, which could be from higher sensitivity to turbulent water than VH (Manjusree et al. 2012).

Setting correct threshold for the VH and VV mask proved to be difficult. Only small changes were seen between certain ranges. In SA1, small changes were seen between -12 and -11 dB in VV and -19 and -20 dB in VH. In SA2, small changes were seen between -22 and -23 dB in VH and -14 and -15 dB in VV. In SA3, small changes were seen between -22 and -23 dB in VH and -14 to -16 dB in VV. In those instances, the optical detection methods were a great supplement. Since optical data were not available for SA1, correct threshold range was uncertain and could either be -19 or -20 dB in VH and -12 to -11 dB in VV.

Optical detection methods displayed turbulence and changing sediment concentrations. Small scale details seen in SA3 such as the changing river width were also seen with optical but not at same level of detail in SAR imagery. Setting the most suitable threshold value for NDWI and Ratio proved to be difficult because of the changing reflective properties of the water seen in SA3.

For some areas, such as the Chasma right bank channel (Section 6.2.3), neither SAR nor optical detection methods were able to detect flooding. Normalized difference indices usually range between -1 and 1 (Grover et al. 2015). This study used threshold values above 0 detected as water surfaces, and values between 0 and 2 were by standards of Table 4, Section 5.2, interpreted as floods. However, in SA3 these ranges were not suitable for interpreting different water surface conditions.

In all study areas, partially submerged areas with dense or sparse vegetation, the SAR flood mask struggled to detect floods. Similar results are found in built-up or urban areas, where roads and buildings create double bounce effects, leading to strong return signals (Jo et al. 2018).

In comparison to SA1 and SA2, the SEM for SA3 brought little change to the area calculation in flood masking. With the exception of clouds removed over the Tiyar mountain, each detection method had little to no change with or without SEM in SA3. Overall, the SEM had the largest impact on SA2, and 91% of the total flood mask in VV were removed. The smallest changes were seen in SA3, where the only steep and high elevated areas were found on the west side at the Tiyar mountain. SA1 were also affected by the SEM, however the side valley seen north of Stjørdalselva were above the 30m threshold and also masked (Section 6.2.1). Consequently, the SEM could underestimate flooding in pools and steep river sides in the side valley. Recognizing all removed areas by the SEM (section 6.3.1) as “flood misclassifications” would be inaccurate.

## 8. Conclusion

In this thesis, flood mapping in optical and radar imagery of three different areas subjected to different flood types have been studied. The first processing steps taken in this study used different filtering options and indices calculations of S1 and S2 imagery to highlight flooded areas. The second part tried automatic thresholding method, where flooded area extent was calculated for each study area. Results were validated using reference images, RGB imagery during flood, and the digital elevation model AW3D.

The methods used in this thesis followed processing steps, where filtering and calculations of indices were handed out on Google Earth Engine. The platform provided high resolution and quick processing of data. The platform allowed for comparisons and combinations of the different satellite instruments: Sentinel 1, Sentinel 2 and ALOS World 3D Surface Model. Results from S1 and S2 data were acquired successfully in SA2 and SA3, while SA1 lacked the results from S2 due to complete cloud cover.

Results of this thesis can be concluded as follows, where strengths were found in:

- The use of two satellite sensors, Sentinel 1 and Sentinel 2, allowed for more flood imagery and detail limitations or strengths seen in backscatter and optical indices
- Orbit filtering and the SEM allowed for less misclassifications seen mainly in mountainous areas and steep terrain. Misclassifications from shadows, foreshortening and layover were reduced because of these methods
- Reference stacks as opposed to single images, allowed for a representation of average pixel backscatter. Outliers such as snow, other non-permanent water bodies and sudden changes to the landscape prior to the flood were removed or lessened as a result. This allowed for smaller chances of misclassifications of flooded areas
- Pixel filtering options allowed for less noise and misclassification on the flood mask
- The elevation threshold of the SEM, in addition to the orbit filtering were sufficient in misclassification removal created by shadow, layover and foreshortening effects

Still, the methods faced constraints which affected the results:

- Clouds obscure flooded areas in S2 imagery
- SEM requires an elevation and slope threshold. Although water flows from high to low, areas with 5-degree slopes could be inundated, as water levels increase and pools up steep river banks and pits

- Orbit filtering worked well in steep and mountainous areas such as SA2, but also reduced number of images in the reference stack
- Cold regions such as Norway experience snow in the winter. As snow becomes wet, backscatter values are reduced and snow-covered areas could be misclassified as water bodies in flood imagery
- Optical and SAR detection methods of this study struggled to capture total extent of floods carrying high amounts of debris or sediments
- Although reference stacks allow for a better representation of what the "average" terrain looks like, it also makes the image smoother. Consequently, the stacks could potentially remove valuable details

In closing, this study highlights the wide varying problems seen in different floods and different terrain. SA1 struggled mapping flooded area due to cloud obscuring the optical imagery. SA2 experienced distortions in the terrain and pixel resolution that could lead to misclassifications in S1 flood mask. SA3 struggled with changing flood water properties, such as turbulent water and suspended sediments. Results of the three study areas show detection methods and their accuracy will vary based on flood type and the terrain. Where the terrain is mountainous, SEM could improve the detection of floods. In flatter terrain, improvements to detection of changing water quality such as suspended sediments and turbulence are more important. For rain floods, optical imagery might not be available, while snowmelt floods could benefit with the use of optical imagery as it could improve the results. The timing of the flood and the temporal interval of images due to orbit time is crucial in order to require images during the flood. Consequently, either S1 or S2 imagery could be the better of the two depending on the image capture date and the date of the flood. Therefore, both should be considered in mapping of flooded areas.

# 9. Recommendations and Opportunities for Further Research

This study found valuable use of S1 and S2 imagery in addition to AW3D for floods in varied terrain types. Gaps in the research were found as snow, vegetation, clouds and water turbulence affected the accuracy of the detection methods. This study focused only on the sentinel missions and their advantages in flood mapping with high spatial resolution and frequent revisit time. Other SAR datasets exists with different wavelength bands such as PALSAR-2 which senses in L-band, TerraSAR-X and COSMO-SkyMed with X-band sensor.

The L band have been suggested in flood detection with its ability to detect water bodies in vegetated areas (Chiu et al, 2000; Martinis et al. 2015). Martinis et al. (2015) proposed the use of X-band in order to create higher contrasts between water bodies and land. Either of these bands could be accessed in TerraSAR-X, COSMO-SkyMed and PALSAR-2 and possibly improve results of the study areas. In SA3, indices were created following McFeeters, (1996) suggestion with GREEN and NIR bands (section 5.2). Different options of bands have been suggested to detect water bodies with Ratio using SWIR and NDTI, NDCL (Meena et al, 2021; Bazilova et al, 2022). These methods could improve the flood detection in Layyah.

This thesis does not consider water inundation around built-up land. The detection methods proposed by McFeeters. (1996) struggles in and around built-up land (Xu, 2006). Xu, (2006) proposed to use MIR band instead of NIR to enhance open water features of NDWI imagery. This index was called MNDWI or Modified Normalized Difference Water Index. This index does also have the potential of reducing shadow noise (Xu, 2006).

The flood detection method with S1 and S2 data were improved with use of the AW3D SEM for mountainous areas, however clouds remained a problem which could only be partially removed in optical imagery. While the S2 2A product allows for good cloud removal with the "CLOUDY_PIXEL_PERCENTAGE" image property, its accuracy for detailed land analysis can still be improved (Chen et al. 2018). A solution for cloud removal could be use of custom cloud masking directly from the S2 level 1C product. The cloud removal algorithm s2cloudless is used on the 2A product, and the algorithm is provided by Braaten, (2023). With this product, users can customize, or change parts of the script, such as threshold ranges and bands. If a unique cloud condition leaves pixels undetected by the 2A product, users could perform their own cloud masking. It is important to note that this would require a good understanding of the s2cloudless algorithm. Furthermore, this algorithm uses long computation time and may struggle for larger areas such as SA3.

Considering the potential increase in floods of different sizes and origins around the world, further studies on flood detection in SAR could be valuable. In Norway, studies on snowmelt floods could be valuable as climate change affect earlier melting seasons (Hanssen-Bauer et al. 2017). In areas impacted by large monsoon floods such as Pakistan and India, improvements on detection methods for turbulent floods could be a valuable asset for rescue operations and damage assessment.

## Reproducibility of Methodology

The JavaScript code created in this thesis is provided in GEE under user mikael_raunig/master_thesis and can be found here: https://code.earthengine.google.com/?accept_repo=users/mikael_raunig/master_thesis. The code is also openly available on GitHub: https://github.com/MikaelRaunig/Master_Thesis

Sentinel 1 SAR GRD, Sentinel 2 level 2A and ALOS DSM: Global 30m v3.2 are all open source and available on GEE.

## References


- AA. (2022). *UN chief urges global community to help flood-affected Pakistan*. Anadolu Agency https://www.aa.com.tr/en/asia-pacific/un-chief-urges-global-community-to-help-flood-affected-pakistan/2672690

- Acharya, T., & Yang, I. (2015). Exploring Landsat 8. *International Journal of IT, Engineering and Applied Sciences Research*, *4*, 4–10.

- AFP & Web Desk. (2022). *Pakistan needs worlds help: UN launches 160m flash appeal for flood victims.*

- Ahmed, K., Shahid, S., & Nawaz, N. (2018). Impacts of climate variability and change on seasonal drought characteristics of Pakistan. *Atmospheric Research*, *214*, 364–374.

- Alfieri, L., Bisselink, B., Dottori, F., Naumann, G., de Roo, A., Salamon, P., Wyser, K., & Feyen, L. (2017). Global projections of river flood risk in a warmer world. *Earth's Future*, *5*(2), 171–182. https://doi.org/10.1002/2016EF000485
- Amarnath, G. (2014). An algorithm for rapid flood inundation mapping from optical data using a reflectance differencing technique. *Journal of Flood Risk Management*, *7*(3), 239–250. https://doi.org/10.1111/jfr3.12045

- Bai, Y., Adriano, B., Mas, E., & Koshimura, S. (2017). Building Damage Assessment in the 2015 Gorkha, Nepal, Earthquake Using Only Post-Event Dual Polarization Synthetic Aperture Radar Imagery. *Earthquake Spectra*, *33*. https://doi.org/10.1193/121516EQS232M

- Baloch, S. M., & Carrington, D. (2022). Pakistan not to blame for climate crisis-fuelled flooding, says PM Shehbaz Sharif. *The Guardian*. https://www.theguardian.com/world/2022/aug/30/pakistan-monsoon-on-steroids-flooding-warning-antonio-guterres

- Bayanudin, A. A., & Jatmiko, R. H. (2016). Orthorectification of Sentinel-1 SAR (Synthetic Aperture Radar) Data in Some Parts of South-eastern Sulawesi Using Sentinel-1 Toolbox. *IOP Conference Series: Earth and Environmental Science*, *47*(1), 012007. https://doi.org/10.1088/1755-1315/47/1/012007

- Bazilova, V., & Kääb, A. (2022). Mapping Area Changes of Glacial Lakes Using Stacks of Optical Satellite Images. *Remote Sensing*, *14*(23), Art. 23. https://doi.org/10.3390/rs14235973

- Belba. P., Kucaj. S., Thanas. J. (2022). *Monitoring of Water Bodies and Non-vegetated Areas in Selenica-Albania with Sar and Optical Images*. Geomatics and Enviromental Engineering. Vol 16. Nr 3. https://doi.org/10.7494/geom.2022.16.3.5

- Bogen, J., Bønsnes, T., Moquet-Stenback, A., Xu, M., Elster, M.C. (2016). *Gudbrnadsdalslågen Sedimentkilder og sedimenttransport. Som bakgrunn for tiltak i forvaltningsplanen.* Norges Vassdrag og Energidirektorat. NVE Rapport nr 89-2016.

- Bondhus, Ø. H. (2022). *Slik forbereder kommunen seg på flom—Og dette bør du gjøre*. driva.no. https://www.driva.no/nyheter/i/Wjr72Q/slik-forbereder-kommunen-seg-paa-flom-og-dette-boer-du-gjoere

- Braaten. J. (2023). *Sentinel-2 Cloud Masking with s2cloudless*. Google Earth Engine. https://developers.google.com/earth-engine/tutorials/community/sentinel-2-s2cloudless

- Buchhorn, M., Lesiv, M., Tsendbazar, N.-E., Herold, M., Bertels, L., & Smets, B. (2020). Copernicus Global Land Cover Layers—Collection 2. *Remote Sensing*, *12*(6), Art. 6. https://doi.org/10.3390/rs12061044

- Chen, J., Li, Y., Ma, Q., Shen, X., Zhao, A., & Li, J. (2018). *Preliminary Evaluation of Sentinel-2 Bottom of Atmosphere Reflectance Using the 6Sv Code in Beijing Area*. *IGARSS 2018 - 2018 IEEE International Geoscience and Remote Sensing Symposium*, 7760–7763. https://doi.org/10.1109/IGARSS.2018.8517598
- Chiu, T., & Sarabandi, K. (2000). Electromagnetic scattering from short branching vegetation. *IEEE Transactions on Geoscience and Remote Sensing*, *38*(2), 911–925. https://doi.org/10.1109/36.841974

- Clarke, B., Otto, F., & Harrington, L. (2022). *Pakistan floods: What role did climate change play?* The Conversation. http://theconversation.com/pakistan-floods-what-role-did-climate-change-play-189833

- Dalen, S. W., Jesper Nordahl Finsveen, Emma Thingstad. (2022). *Ble evakuert: - Alvorlig*. Dagbladet. https://www.dagbladet.no/nyheter/ble-evakuert---alvorlig/75132737

- De Zan, F., & Monti Guarnieri, A. (2006). TOPSAR: Terrain Observation by Progressive Scans. IEEE Transactions on Geoscience and Remote Sensing, 44(9), 2352–2360.

- du Preez, J., & Sinha, S. (2016). *Millimeter-Wave Antennas: Configurations and Applications*. Springer International Publishing. https://doi.org/10.1007/978-3-319-35068-4

- Earth Engine. (2022). *Ee.ImageCollection.mean*. Google Developers. https://developers.google.com/earth-engine/apidocs/ee-imagecollection-mean

- EOS. (2021). *Normalized Difference Water Index: NDWI Formula And Calculations*. https://eos.com/make-an-analysis/ndwi/

- ESA. (2022). *Sentinel-1 Algorithms*. Google Developers. Hentet 12. mai 2023, fra https://developers.google.com/earth-engine/guides/sentinel1

- Ferro-Famil. L., Pottier. E. (2016). Synthetic Aperture Radar Imaging. Microwave Remote Sensing of Land Surface: Techniques and Methods. 2016, p. 1-65. https://www.sciencedirect.com/topics/earth-and-planetary-sciences/p-band

- Fischer. (2015). *Cloud and Cloud-Shadow Detection in SPOT5 HRG Imagery with Automated Morphological Feature Extraction.* Remote Sensing, 6, 776-800. doi:10.3390/rs6010776

- Floricioiu, D., & Rott, H. (2001). Seasonal and short-term variability of multifrequency, polarimetric radar backscatter of Alpine terrain from SIR-C/X-SAR and AIRSAR data. *IEEE Transactions on Geoscience and Remote Sensing*, *39*(12), 2634–2648. https://doi.org/10.1109/36.974998

- Fouad, M., Elbohy, A., Mashaly, A., Abosekeen, A., Abdalla, A., & Azouz, A. (2022). Spaceborne SAR image formation enhancement using MOCO techniques. *The Egyptian Journal of Remote Sensing and Space Science*, *25*(3), 659–671. https://doi.org/10.1016/j.ejrs.2022.06.001
- Freeman, A., & Durden, S. L. (1998). A three-component scattering model for polarimetric SAR data. *IEEE Transactions on Geoscience and Remote Sensing*, *36*(3), 963–973. https://doi.org/10.1109/36.673687

- Gao. Bo-Cai. (1996). *NDWI-A Normalized Difference Water Index for Remote Sensing of Vegetation Liquid for Remote Sensing of Vegetation Liquid Water From Space*. Remote Sensing of Environment. doi:10.1016/S0034-4257(96)00067-3.

- GEE Guides. (2021). *Scale | Google Earth Engine*. Google Developers. https://developers.google.com/earth-engine/guides/scale

- Gorelick, N., Hancher, M., Dixon, M., Ilyushchenko, S., Thau, D., & Moore, R. (2017). Google Earth Engine: Planetary-scale geospatial analysis for everyone. *Remote Sensing of Environment*.

- Goswami, B. N., Lau, W., & Waliser, D. (2007). *South Asian Monsoon* (ss. 19–61). https://doi.org/10.1007/3-540-27250-X_2

- Grover, A., & Singh, R. B. (2015). Analysis of Urban Heat Island (UHI) in Relation to Normalized Difference Vegetation Index (NDVI): A Comparative Study of Delhi and Mumbai. *Environments*, *2*(2), Art. 2. https://doi.org/10.3390/environments2020125

- Gu, Y., Hunt, E., Wardlow, B., Basara, J. B., Brown, J. F., & Verdin, J. P. (2008). Evaluation of MODIS NDVI and NDWI for vegetation drought monitoring using Oklahoma Mesonet soil moisture data. *Geophysical Research Letters*, *35*(22). https://doi.org/10.1029/2008GL035772

- Guardian. (2022). *Pakistan floods cause devastation – in pictures*. *The Guardian*. https://www.theguardian.com/world/gallery/2022/aug/30/pakistan-floods-cause-devastation-in-pictures

- Hagen, N. A., & Kudenov, M. W. (2013). Review of snapshot spectral imaging technologies. *Optical Engineering*, *52*(9), 090901. https://doi.org/10.1117/1.OE.52.9.090901

- Hall. D. (1996). *Remote sensing applications to hydrology; imaging radar*. Hydrological Sciences – Journal des Sciences Hydrologiques https://doi.org/10.1080/02626669609491528

- Hanssen-Bauer, I., Førland, E.J., Haddeland, I., Hisdal, H., Mayer, S., Nesje, A., Nilsen, J., Sandven, S., Sandø, A., Ådlandsvik, B. (2017). *Climate in Norway 2100 – A knowledge base for climate adaptation.* Miljødirektoratet. NCCS report no. 1/2017

- Hofmeister, F., Arias-Rodriguez, L. F., Premier, V., Marin, C., Notarnicola, C., Disse, M., & Chiogna, G. (2022). Intercomparison of Sentinel-2 and modelled snow cover maps in a high-elevation Alpine catchment. *Journal of Hydrology X*, *15*, 100123. https://doi.org/10.1016/j.hydroa.2022.100123
- Hofstad, S. (2022). *Gyda: Se bildene fra ekstremværet i Trøndelag*. NRK. https://www.nrk.no/trondelag/gyda_-se-bildene-fra-ekstremvaeret-i-trondelag-1.15808835

- Huang, M., & Jin, S. (2022). Backscatter Characteristics Analysis for Flood Mapping Using Multi-Temporal Sentinel-1 Images. *Remote Sensing*, *14*(15), Art. 15. https://doi.org/10.3390/rs14153838

- Hussain, I. (2022). *Layyah's riverine belt ravaged by flood*. The Express Tribune. https://tribune.com.pk/story/2376364/layyahs-riverine-belt-ravaged-by-flood

- Jain, P., Schoen, B., Ross, R .(2020). *Automatic Flood Detection in Sentinel-2 Images Using Deep Convolutional Neural Networks.* InThe35thACM/SIGAPP Symposium on Applied Computing. https://doi.org/10.1145/3341105.3374023

- Jo, M. J., Osmanoglu, B., Zhang, B., & Wdowinski, S. (2018). *Flood extent mapping using dual-polarimetric Sentinel-1 synthetic aperture radar imagery*. Florida International University

- *K, Fletcher*. 2012. *Sentinel-1:ESA's Radar Observatory Mission for GMES Operational Services.* European Space Agency. *https://sentinel.esa.int/documents/247904/349449/s1_sp-1322_1.pdf*

- Fletcher. 2012. *Sentinel-2: ESA's Optical High-Resolution Mission for GMES Operational Services.* European Space Agency. https://sentinel.esa.int/documents/247904/349490/s2_sp-1322_2.pdf

- Klemas, V., Finkl, C., Makowski, C. (2014). *Remote Sensing and Modelling: Advances in Coastal and Marine Resources.* Coastal Research Library. Vol 9. DOI 10.1007/978-3-319-06326-3_1

- Kääb, A. (2004). *Global Change Impacts in Mountain Biosphere Reserves.* UNESCO – Division of Ecological and Earth Sciences. https://unesdoc.unesco.org/ark:/48223/pf0000142482?posInSet=1&queryId=28e8041e-1399-448a-b4e6-73cf2b3cfd66

- Kääb, A., Huggel, C., Paul, F., Wessels, R., Raup, B., Kieffer, H., & Kargel, J. (2002). *GLACIER MONITORING FROM ASTER IMAGERY: ACCURACY AND APPLICATIONS*. Proceedings of EARSeL-LISSIG-Workshop Observing Our Cryosphere from Space. EARSeL Proceedings, v. 2, p. 43-53, http://folk.uio.no/kaeaeb/publications/kaeaeb_earsel.pdf

- Landuyt, L., Verhoest, N. E. C., & Van Coillie, F. M. B. (2020). Flood Mapping in Vegetated Areas Using an Unsupervised Clustering Approach on Sentinel-1 and -2 Imagery. *Remote Sensing*, *12*(21), Artikkel 21. https://doi.org/10.3390/rs12213611

- Langsholt, E., Holmqvist, E. (2017). *Høstflom på Sørlandet 30.9-3.10.2017*. Norges Vassdrag og Energidirektorat. Rapport nr 80-2017.

- Lemoine, G. Refined Lee GEE Implementation. 2018. Available online: https://code.earthengine.google.com/5d1ed0a0f0417f098fdfd2fa137c3d0c

- Liang, H., Xu, W., Ding, X., Zhang, L., & Songbo, W. (2021). *Urban Sensing with Spaceborne Interferometric Synthetic Aperture Radar* (s. 345–365). https://doi.org/10.1007/978-981-15-8983-6_21

- Liang, J., & Liu, D. (2020). A local thresholding approach to flood water delineation using Sentinel-1 SAR imagery. *ISPRS Journal of Photogrammetry and Remote Sensing*, *159*, 53–62. https://doi.org/10.1016/j.isprsjprs.2019.10.017

- Li, J., & Chen, B. (2020). Global Revisit Interval Analysis of Landsat-8 -9 and Sentinel-2A -2B Data for Terrestrial Monitoring. *Sensors*, *20*(22), Art. 22. https://doi.org/10.3390/s20226631

- Lin, L., Di, L., Tang, J., Yu, E., Zhang, C., Rahman, M., Shrestha, R., & Kang, L. (2019). Improvement and validation of NASA/MODIS NRT global flood mapping. *Remote Sensing*, *11*, 205. https://doi.org/10.3390/rs11020205

- Liu, C.-C., Shieh, M.-C., Ke, M.-S., & Wang, K.-H. (2018*). Flood Prevention and Emergency Response System Powered by Google Earth Engine. Remote Sensing*, *10*(8), Art. 8. https://doi.org/10.3390/rs10081283

- Lucas, R. M., Mitchell, A. L., Rosenqvist, A., Proisy, C., Melius, A., & Ticehurst, C. (2007). The potential of L-band SAR for quantifying mangrove characteristics and change: Case studies from the tropics. *Aquatic Conservation: Marine and Freshwater Ecosystems*, *17*(3), 245–264. https://doi.org/10.1002/aqc.833

- Manjusree, P., Prasanna Kumar, L., Bhatt, C. M., Rao, G. S., & Bhanumurthy, V. (2012). Optimization of threshold ranges for rapid flood inundation mapping by evaluating backscatter profiles of high incidence angle SAR images. *International Journal of Disaster Risk Science*, *3*, 113-122.

- Martinis, S., Kuenzer, C., Wendleder, A., Huth, J., Twele, A., Roth, A., & Dech, S. (2015). Comparing four operational SAR-based water and flood detection approaches. *International Journal of Remote Sensing*, *36*(13), 3519-3543.

- Meena, S. R., Chauhan, A., Bhuyan, K., & Singh, R. P. (2021). Chamoli disaster: Pronounced changes in water quality and flood plains using Sentinel data. *Environmental Earth Sciences*, *80*(17), 601. https://doi.org/10.1007/s12665-021-09904-z

- Merz, R., Blöschl, G. (2003). *A process typology of regional floods.* Water Resources Research, 39 (12), article number 1340. https://www.academia.edu/6060165/Merz_R_and_G_Bl%C3%B6schl_2003_A_proce

ss_typology_of_regional_floods_Water_Resources_Research_39_12_article_number_1340

- Michel, C., Sorteberg, A., Eckhardt, S., Weijenborg, C., Stohl, A., & Cassiani, M. (2021). Characterization of the atmospheric environment during extreme precipitation events associated with atmospheric rivers in Norway—Seasonal and regional aspects. *Weather and Climate Extremes*, *34*, 100370. https://doi.org/10.1016/j.wace.2021.100370

- Mizutori, M., & Guha-Sapir, D. (2020). *Human cost of disasters. An overview of the last 20 years 2000-2019.* Centre for Research on the Epidemiology of Disasters United Nations Office for Disasters Risk Reduction. https://www.undrr.org/quick/50922

- Moghaddam, M., & Saatchi, S. (1995). Analysis of scattering mechanisms in SAR imagery over boreal forest: Results from BOREAS '93. *IEEE Transactions on Geoscience and Remote Sensing*, *33*(5), 1290–1296. https://doi.org/10.1109/36.469495

- Moharrami, M., Javanbakht, M., & Attarchi, S. (2021). Automatic flood detection using sentinel-1 images on the google earth engine. *Environmental Monitoring and Assessment*, *193*(5), 248. https://doi.org/10.1007/s10661-021-09037-7

- Moreira, A., Prats-Iraola, P., Younis, M., Krieger, G., Hajnsek, I., & Papathanassiou, K. P. (2013). A tutorial on synthetic aperture radar. *IEEE Geoscience and Remote Sensing Magazine*, *1*(1), 6–43. https://doi.org/10.1109/MGRS.2013.2248301

- Moser, G., & Zerubia, J. (Red.). (2018). *Mathematical Models for Remote Sensing Image Processing*. Springer International Publishing. https://doi.org/10.1007/978-3-319-66330-2

- Moskolai. W., Abdou. W., Dipanda., Kolyang. (2022). *A Workflow for Collecting and Preprocessing Sentinel-1 Images for Time Series Prediction Suitable for Deep Learning Algorithms*. Geomatics, 2, 435-456. https://doi.org/10.3390/geomatics2040024

- Mullissa, A., Vollrath, A., Odongo-Braun, C., Slagter, B., Balling, J., Gou, Y., Gorelick, N., & Reiche, J. (2021). Sentinel-1 SAR Backscatter Analysis Ready Data Preparation in Google Earth Engine. *Remote Sensing*, *13*(10), 1954. https://doi.org/10.3390/rs13101954

- NASA. (2006). *High and Low Tides in Bay of Fundy*. NASA Earth Observatory. https://earthobservatory.nasa.gov/images/6650/high-and-low-tides-in-bay-of-fundy

- NASA. (2014). *Gonzalo Stirs Up Sediment and the Carbon Cycle*. NASA Earth Observatory. https://earthobservatory.nasa.gov/images/84595/gonzalo-stirs-up-sediment-and-the-carbon-cycle
- Nicolis, O., Gonzalez, C. (2021). Wavelet-based fractal and multifractal analysis for detecting mineral deposits using multispectral images taken by drones. *Methods Appl. Pet. Miner. Explor. Eng. Geol.* 295–307.

- NMCE. (2020). *National Forestry Accounting Plan for Norway, including forest reference level for the first commitment period 2021-2025.* Norwegian Ministry of Climate and Environment. nor198934.pdf (fao.org)

- NVE Atlas. (2022). *Norges Vassdrag og Energidirektorat.* https://atlas.nve.no/html5Viewer/?viewer=nveatlas

- OCHA Humanitaria Advisory Team, (HAT). (2022). *Pakistan: 2022 Monsoon Floods.* Situation Report No.03. www.unocha.org

- Ottinger, M., & Kuenzer, C. (2020). Spaceborne L-Band Synthetic Aperture Radar Data for Geoscientific Analyses in Coastal Land Applications: A Review. *Remote Sensing*, *12*, 2228. https://doi.org/10.3390/rs12142228

- Pakistan Meteorological Department, PMD. (2022). *Pakistan's monthly climate summary, August 2022.* Government of Pakistan. https://www.pmd.gov.pk/cdpc/Pakistan_Monthly_Climate_Summary_August_2022.pdf

- Peebles, Peyton Z. *1998. Radar Principles.* John Wiley and Sons, Inc. page 20.

- Pettersen, J. (2022). *Uværet i Midt-Norge: Kraftig vind gir strømbrudd og stengte veier*. NRK. https://www.nrk.no/trondelag/etter-ekstremvaeret-_gyda__-fjellbygden-meraker-i-trondelag-er-isolert-1.15810260

- Pohl, C., & Van Genderen, J. L. (1998). Review article Multisensor image fusion in remote sensing: Concepts, methods and applications. *International Journal of Remote Sensing*, *19*(5), 823–854. https://doi.org/10.1080/014311698215748

- Prats-Iraola, Pau & Nannini, Matteo & Scheiber, Rolf & De Zan, Francesco & Wollstadt, Steffen & Minati, F. & Costantini, Marine & Bucarelli, Andrea & Borgstrom, Sven & Walter, Thomas R. & Foumelis, Michael & Desnos, Yves-Louis. (2015). Sentinel-1 Assessment of the Interferometric Wide-Swath Mode. 1-4. https://doi.org/10.1109/IGARSS.2015.7327018.

- Roald, L. (2021). *Floods in Norway*. Norges vassdrags- og energidirektorat. NVE Rapport nr 1/2021.

- Roaldseth, S. L. (2022). *Tror «Gyda» vil koste over 100 millioner kroner*. NRK. https://www.nrk.no/mr/tror-_gyda_-vil-koste-over-100-millioner-kroner-1.15814493

- Schinasi, L. H., Benmarhnia, T., & De Roos, A. J. (2018). Modification of the association between high ambient temperature and health by urban microclimate indicators: A systematic review and meta-analysis. *Environmental Research*, *161*, 168–180. https://doi.org/10.1016/j.envres.2017.11.004

- Shreshta. AB., Agrawal. NK., Afthan. B., Bajracharya. SR., Maréchal. J., van Oort. B. (2015). *The Himalayan Climate and Water Atlas; Impact of Climate Change on Water Resources in Five of Asia's Major River Basins.* ICIMOD, GRID-Arendal and CICERO. P 35-69 https://lib.icimod.org/record/31180

- Singha, M., Dong, J., Sarmah, S., You, N., Zhou, Y., Zhang, G., Doughty, R., & Xiao, X. (2020). Identifying floods and flood-affected paddy rice fields in Bangladesh based on Sentinel-1 imagery and Google Earth Engine. *ISPRS Journal of Photogrammetry and Remote Sensing*, *166*, 278–293. https://doi.org/10.1016/j.isprsjprs.2020.06.011

- Singh, M., Singh, I. B., & Müller, G. (2007). Sediment characteristics and transportation dynamics of the Ganga River. *Geomorphology*, *86*(1), 144–175. https://doi.org/10.1016/j.geomorph.2006.08.011

- Skjerdal, M., Hagen, B., Mamen, J., Rudberg, J., Fagerlid, G. (2022). *Ekstremværet Gyda 12.-13. januar 2022.* Meteorologisk Institutt. No. 14/2022.

- Song, X.-P., Huang, W., Hansen, M. C., & Potapov, P. (2021). An evaluation of Landsat, Sentinel-2, Sentinel-1 and MODIS data for crop type mapping. *Science of Remote Sensing*, *3*, 100018. https://doi.org/10.1016/j.srs.2021.100018

- Smith, K. (2013). *Enviromental Hazards. Assessing Risk and Reducing Disaster.* Sixth edition. Routledge.

- Spoto, F., Sy, O., Laberinti, P., Martimort, P., Fernandez, V., Colin, O., Hoersch, B., & Meygret, A. (2012). Overview Of Sentinel-2. *2012 IEEE International Geoscience and Remote Sensing Symposium*, 1707–1710. https://doi.org/10.1109/IGARSS.2012.6351195

- Stavang, A., Kolberg, S. (2022). Varsom *Status for vårflom pr. 10. Juni 2022. Varsom.no*. https://varsom.no/nyheter/nyheter-flom-og-jordskred/status-for-varflom-pr-10-juni-2022/

- Stohl, A., Forster, C., & Sodemann, H. (2008). Remote sources of water vapor forming precipitation on the Norwegian west coast at 60°N–a tale of hurricanes and an atmospheric river. *Journal of Geophysical Research: Atmospheres*, *113*(D5). https://doi.org/10.1029/2007JD009006

- Strzelczyk, S., Strzelczyk, J., Szostek, K., Dwornik, M., Leśniak, A., Bała, J., & Franczyk, A. (2021). Information Extraction from Satellite-Based Polarimetric SAR Data Using Simulated Annealing and SIRT Methods and GPU Processing. *Energies*, *15*, 72. https://doi.org/10.3390/en15010072
- Svendsen, M. (2022). *Ekstremvêret «Gyda»: Då dei ikkje blei henta måtte dei evakuere i eigen båt*. NRK. https://www.nrk.no/trondelag/nve_-ekstremveret-_gyda_-har-ikkje-nadd-toppen-_-stor-vassforing-i-fleire-elver-i-trondelag-1.15808253

- Tadono, T., Ishida, H., Oda, F., Naito, S., Minakawa, K., & Iwamoto, H. (2014). "Precise Global DEM Generation by ALOS PRISM." ISPRS Annals of the Photogrammetry, Remote Sensing and Spatial Information Sciences, Vol.II-4. pp.71-76, 2014

- Takaku, J., Tadono, Doutsu, M., Ohgushi, F., & Kai, H. (2020). "Updates of 'AW3D30' ALOS Global Digital Surface Model with Other Open Access Datasets". The International Archives of the Photogrammetry. Remote Sensing and Spatial Information Sciences.

- Takaku, J., Tadono, T., & Tsutsui, K. (2014). "Generation of High Resolution Global DSM from ALOS PRISM," The International Archives of the Photogrammetry, Remote Sensing and Spatial Information Sciences, ISPRS, Vol.XL-4. pp.243-248

- Tan, S.-L. (2022). *Pakistan is bearing the brunt of the climate crisis despite «small carbon footprint,» minister says*. CNBC. https://www.cnbc.com/2022/09/06/pakistan-finmin-on-floods-country-is-bearing-brunt-of-climate-change.html

- Tarpanelli, A., Mondini, A. C., & Camici, S. (2022). Effectiveness of Sentinel-1 and Sentinel-2 for flood detection assessment in Europe. *Natural Hazards and Earth System Sciences*, *22*(8), 2473–2489. https://doi.org/10.5194/nhess-22-2473-2022

- Tiwari. V., Kumar. V., Matin. MA., Thapa. A., Ellenburg. WL., Gupta. N., Thapa. S. (2020). *Flood inundation mapping- Kerala 2018; Harnessing the power of SAR, automatic threshold detection method and Google Earth Engine*. PLOS One https://doi.org/10.1371/journal.pone.0237324

- Torres, R., Snoeij, P., Geudtner, D., Bibby, D., Davidson, M., Attema, E., Potin, P., Rommen, B., Floury, N., Brown, M., Traver, I. N., Deghaye, P., Duesmann, B., Rosich,

B., Miranda, N., Bruno, C., L'Abbate, M., Croci, R., Pietropaolo, A., … Rostan, F. (2012). GMES Sentinel-1 mission. *Remote Sensing of Environment, 120*, 9–24. https://doi.org/10.1016/j.rse.2011.05.028

- Trisakti, B., Carolita, I., & Pradana, A. (2010). Digital Elevation Model From Prism-Also and Aster Stereoscopic Data. *International Journal of Remote Sensing and Earth Sciences (IJReSES), 6*. https://doi.org/10.30536/j.ijreses.2009.v6.a1236

- Tsai, Y.-L. S., Dietz, A., Oppelt, N., & Kuenzer, C. (2019). Remote Sensing of Snow Cover Using Spaceborne SAR: A Review. *Remote Sensing*, *11*(12), Artikkel 12. https://doi.org/10.3390/rs11121456

- Tulbure, M. G., Broich, M., Perin, V., Gaines, M., Ju, J., Stehman, S. V., Pavelsky, T., Masek, J. G., Yin, S., Mai, J., & Betbeder-Matibet, L. (2022). Can we detect more ephemeral floods with higher density harmonized Landsat Sentinel 2 data compared to Landsat 8 alone? *ISPRS Journal of Photogrammetry and Remote Sensing*, *185*. 232–246. https://doi.org/10.1016/j.isprsjprs.2022.01.021

- Twele, A., Cao, W., Plank, S., & Martinis, S. (2016). Sentinel-1-based flood mapping: A fully automated processing chain. *International Journal of Remote Sensing*. https://www.tandfonline.com/doi/full/10.1080/01431161.2016.1192304

- USAID, Bureau for Humanitarian Assistance. (2022). *USG Pakistan Floods Fact Sheet*. https://www.usaid.gov/sites/default/files/2022-12/2022-09-30_USG_Pakistan_Floods_Fact_Sheet_8.pdf

- Varsom (2022). *Flomfare på rødt nivå i deler av Nord-Vestlandet*. Varsom.no https://varsom.no/nyheter/nyheter-flom-og-jordskred/flomfare-pa-rodt-niva-i-deler-av-nord-vestlandet/

- Wang, Z., Zhang, C., & Atkinson, P. M. (2022). Combining SAR images with land cover products for rapid urban flood mapping. *Frontiers in Environmental Science*, *10*. https://www.frontiersin.org/articles/10.3389/fenvs.2022.973192

- Wangchuk. S., Bolch. T. & Robson. B. (2022). *Monitoring glacial lake outburst food susceptibility using Sentinel-1 SAR data, Google Earth Engine, and persistent scatterer interferometry*. Department of Geography & Sustainable Development, University of St Andrews, St Andrews, UK. 1-s2.0-S0034425722000244-main.pdf

- Wasser. L. (2017). *Introduction to Spatial and Spectral Resolution: Multispectral Imagery*. Earth Data Science - Earth Lab. https://www.earthdatascience.org/courses/earth-analytics/multispectral-remote-sensing-data/introduction-multispectral-imagery-r/

- Xu. H. (2006). *Modification of normalised difference water index (NDWI) to enhance open water features in remotely sensed imagery*. International Journal of Remote Sensing. Vol 27, No. 14. https://doi.org/10.1080/01431160600589179

# Appendix I: Study area 1, Stjørdalen

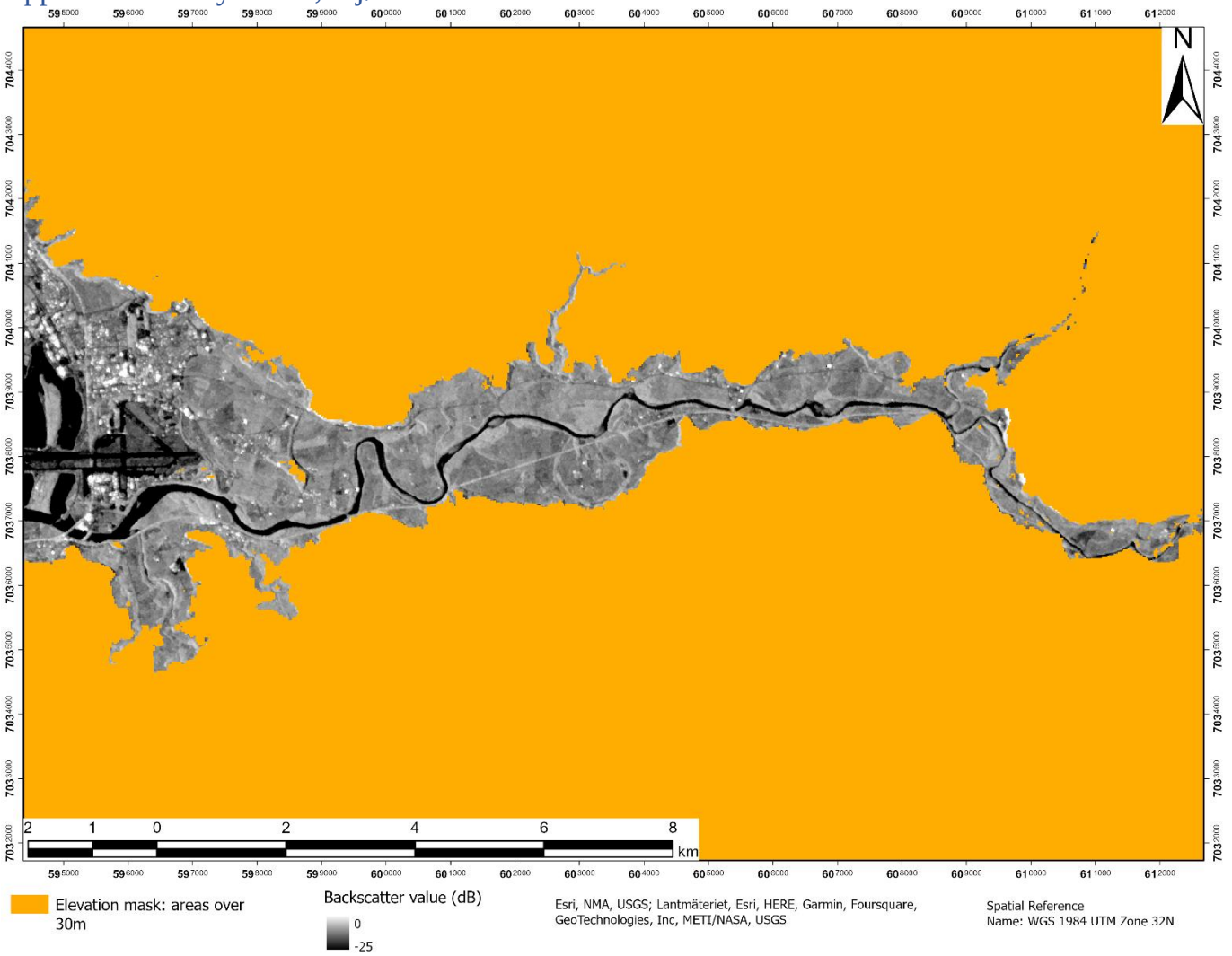


*Appendix 1A: Elevation mask of SA1. Background map is the VH reference image of SA1.*

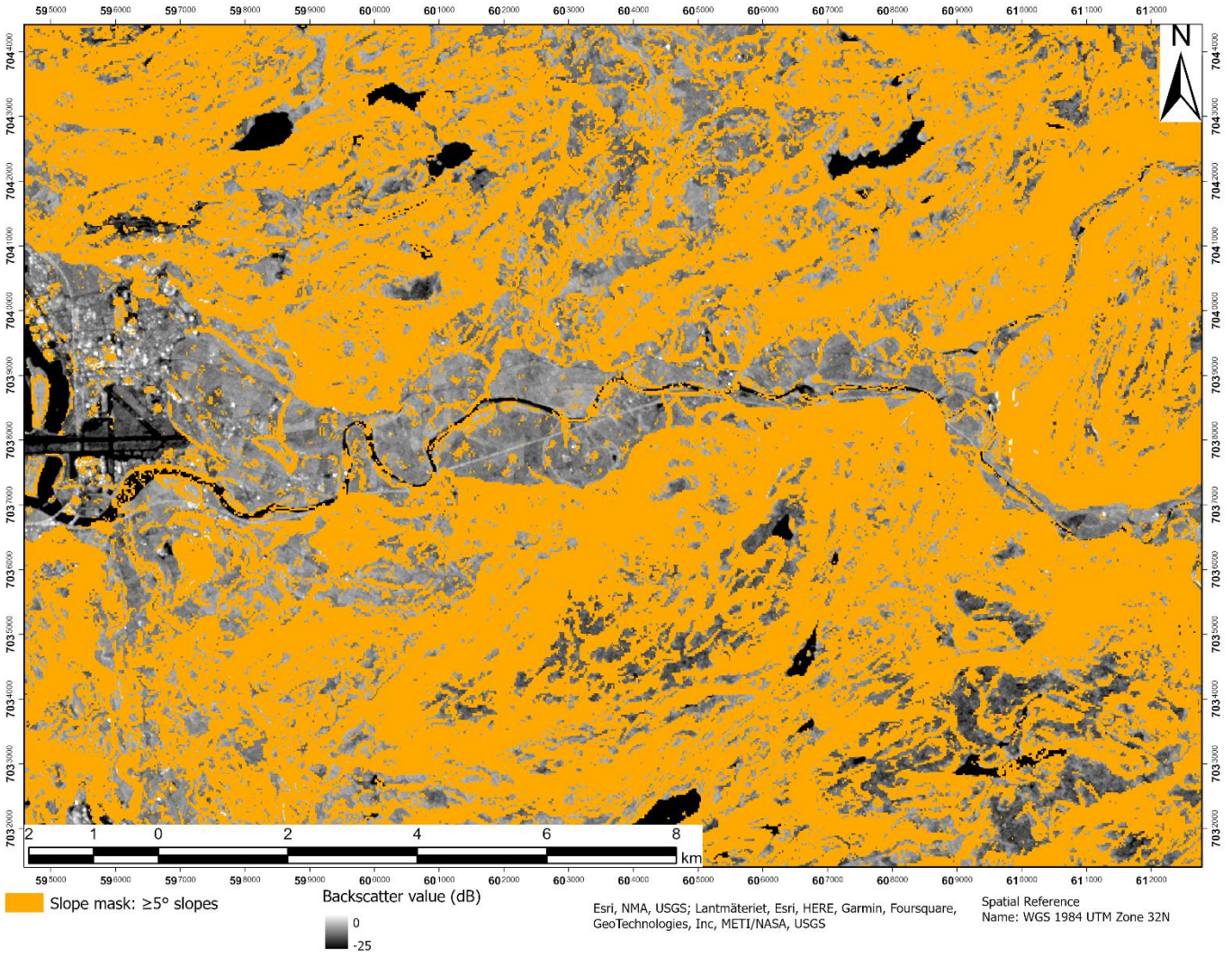


*Appendix 1B: Slope mask of SA1. Background map is the VH reference image of SA1.*

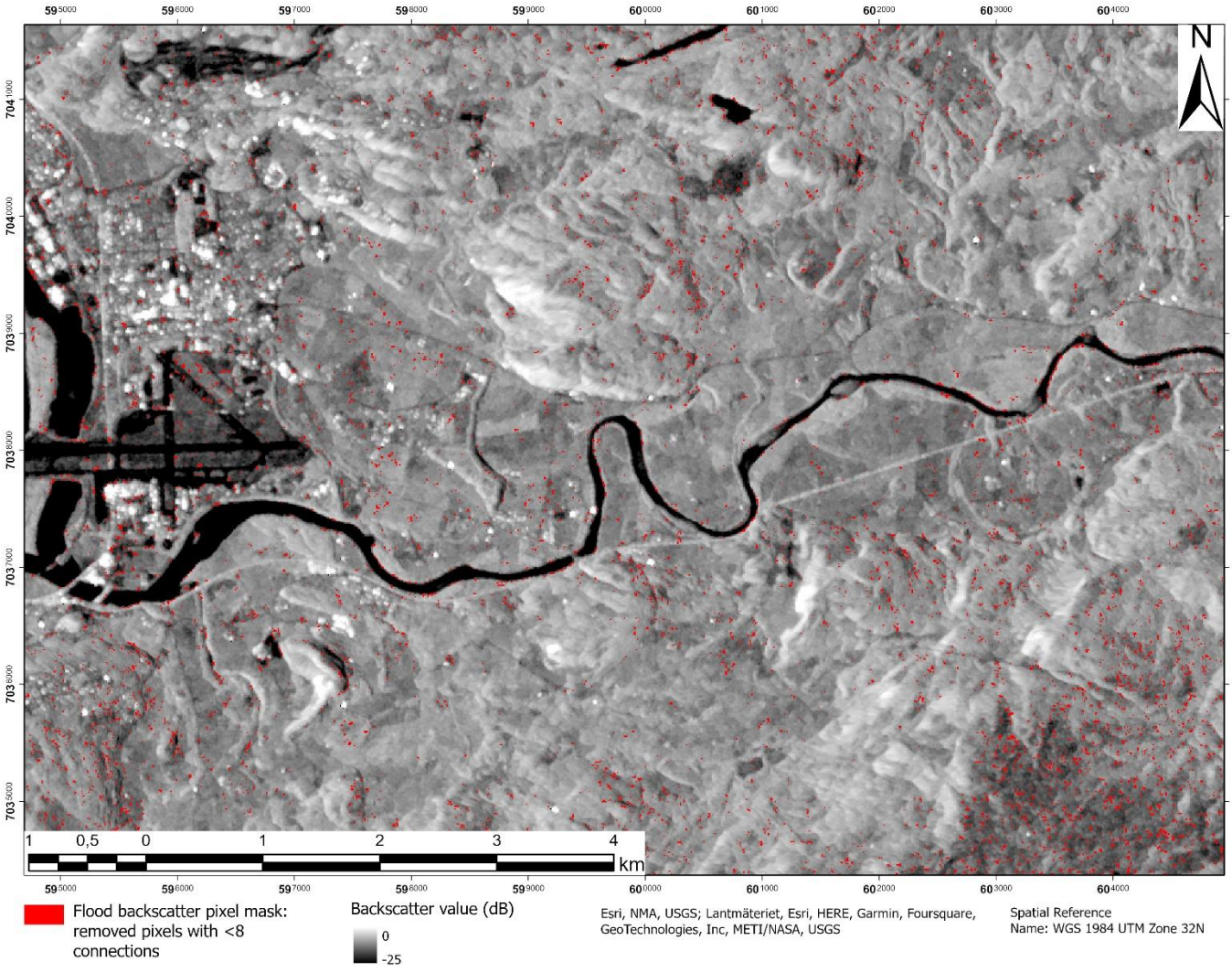


*Appendix 1C: Pixel mask of SA1. Background map is the VH reference image of SA1. Projection is 1:40 000 for a higher exaggeration of pixels.*

# Appendix II: Study area 2, Sunndal

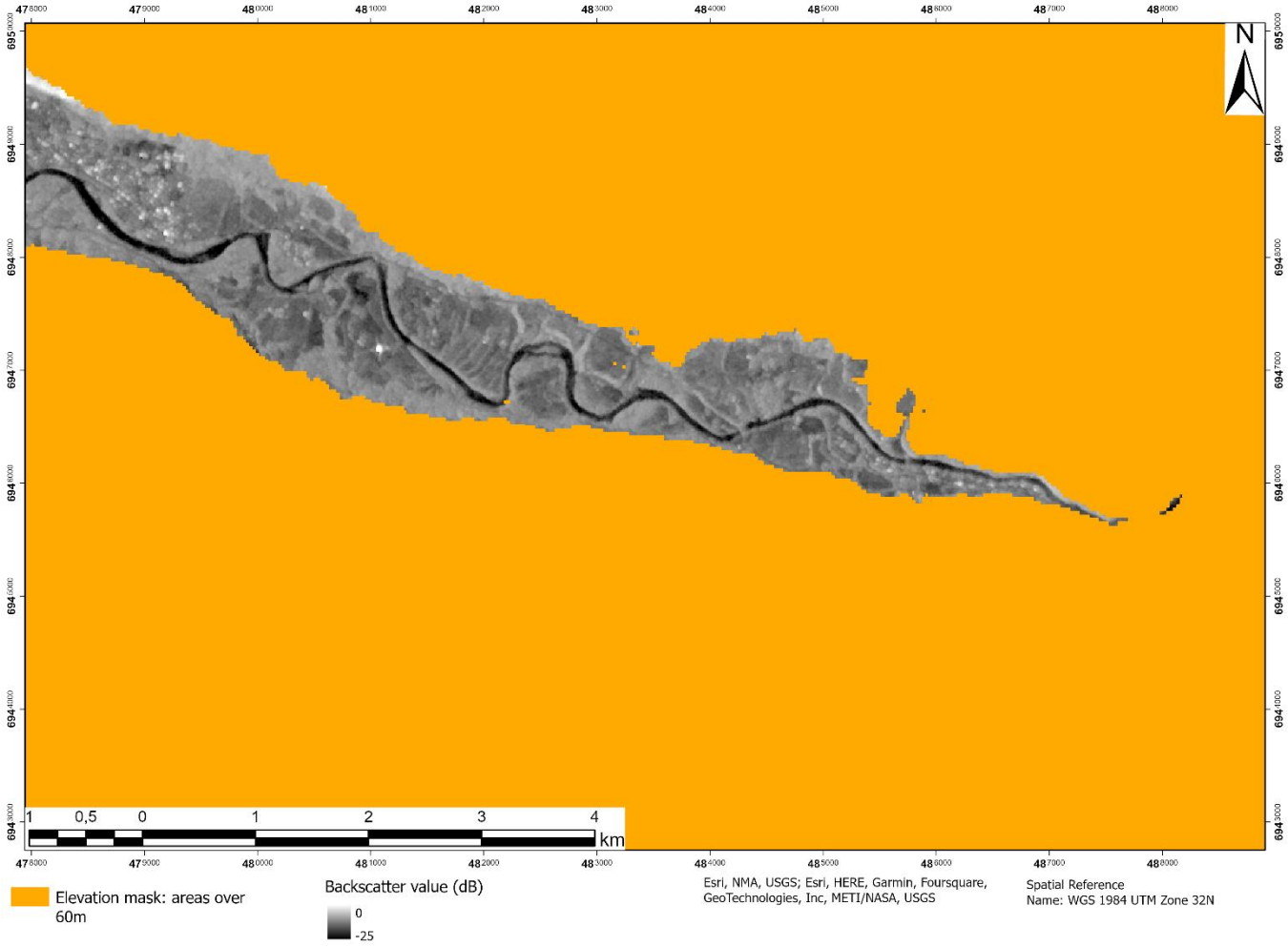


*Appendix 2A: Elevation mask of SA2. Background map is the VH reference image of SA2.*

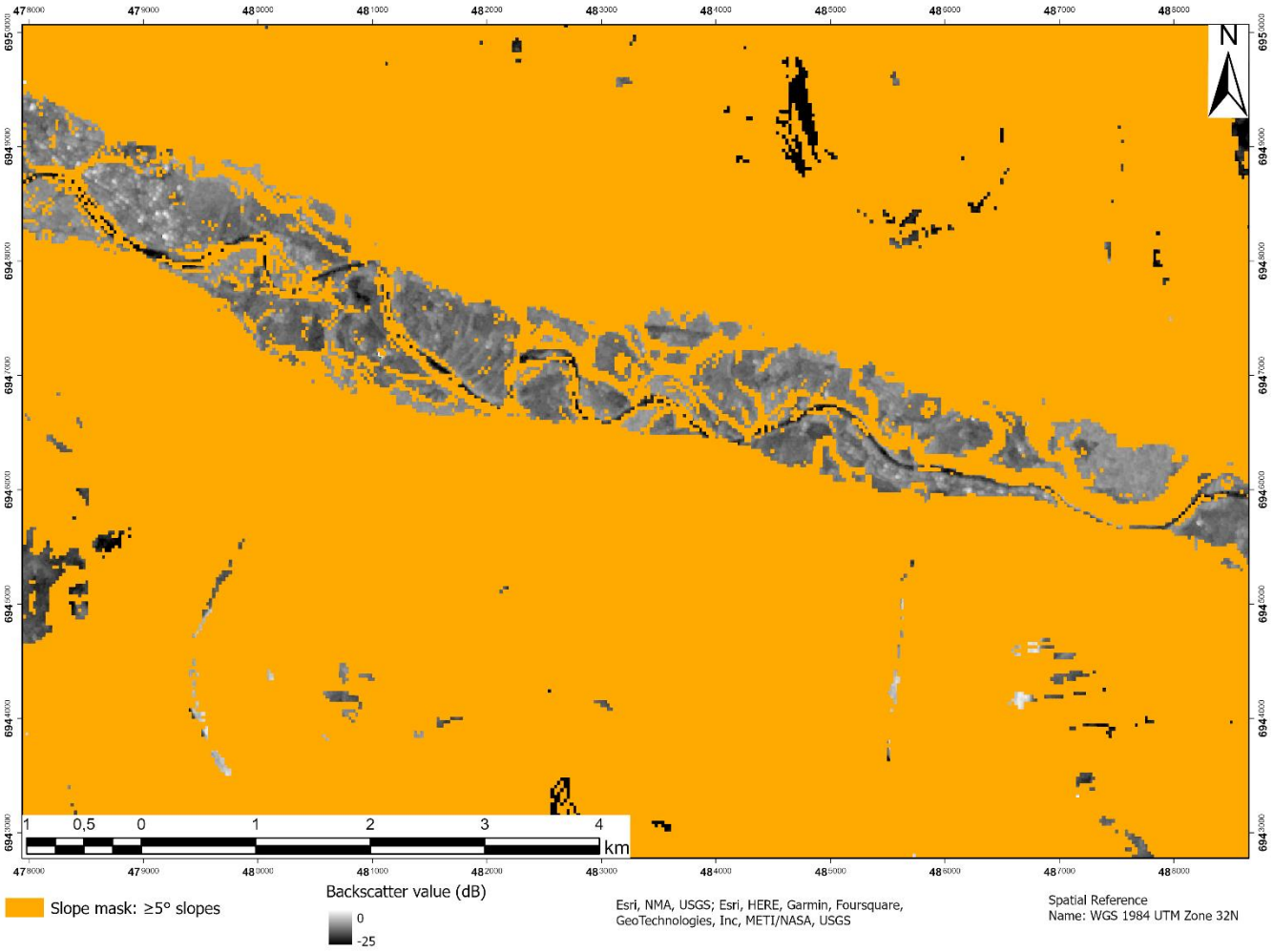


*Appendix 2B: Slope mask of SA2. Background map is the VH reference image of SA2.*

E

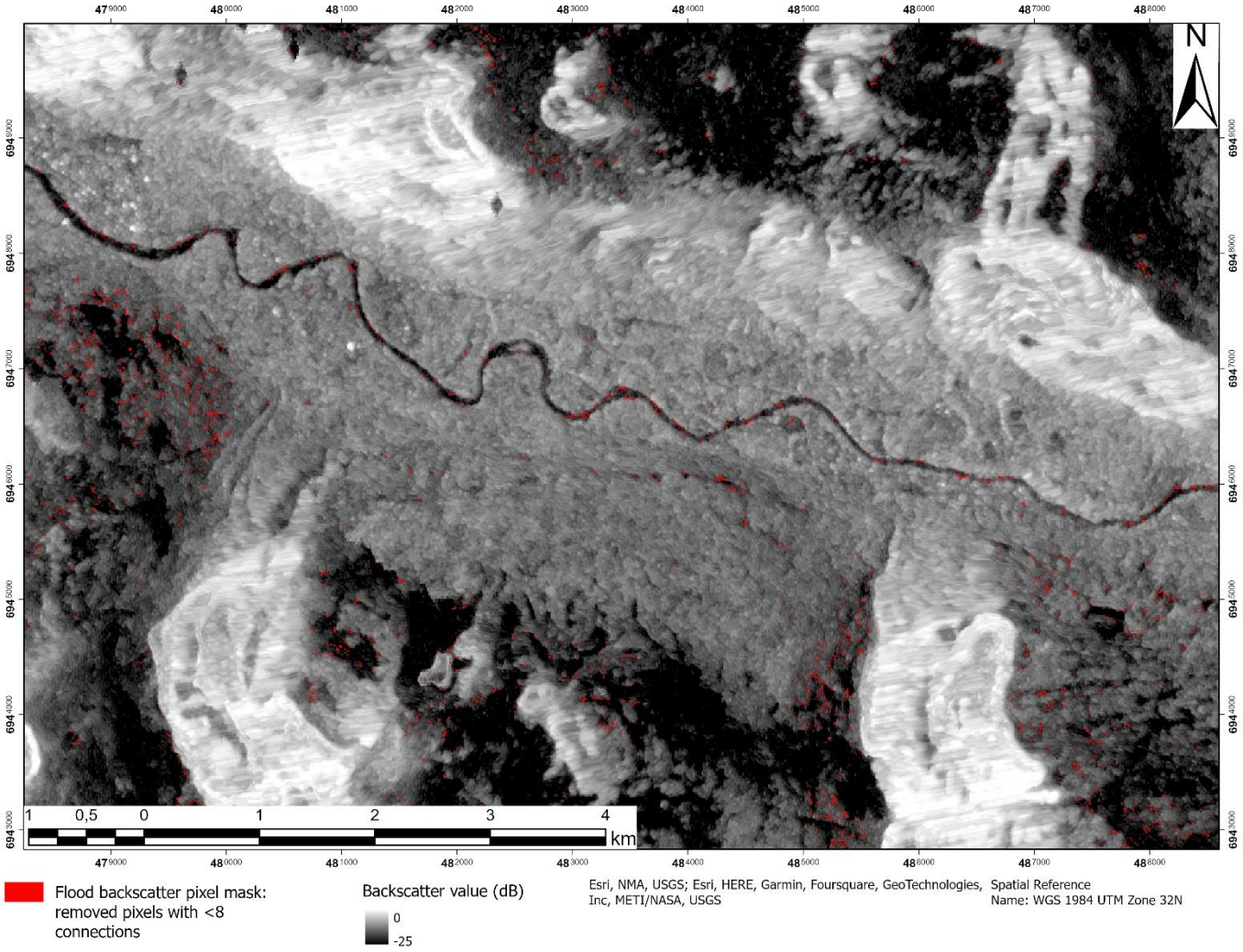


*Appendix 2C: Pixel mask of SA2. Background map is the VH reference image of SA2. Projection is 1:40 000 for a higher exaggeration of pixels.*

# Appendix III: Study area 3, Layyah

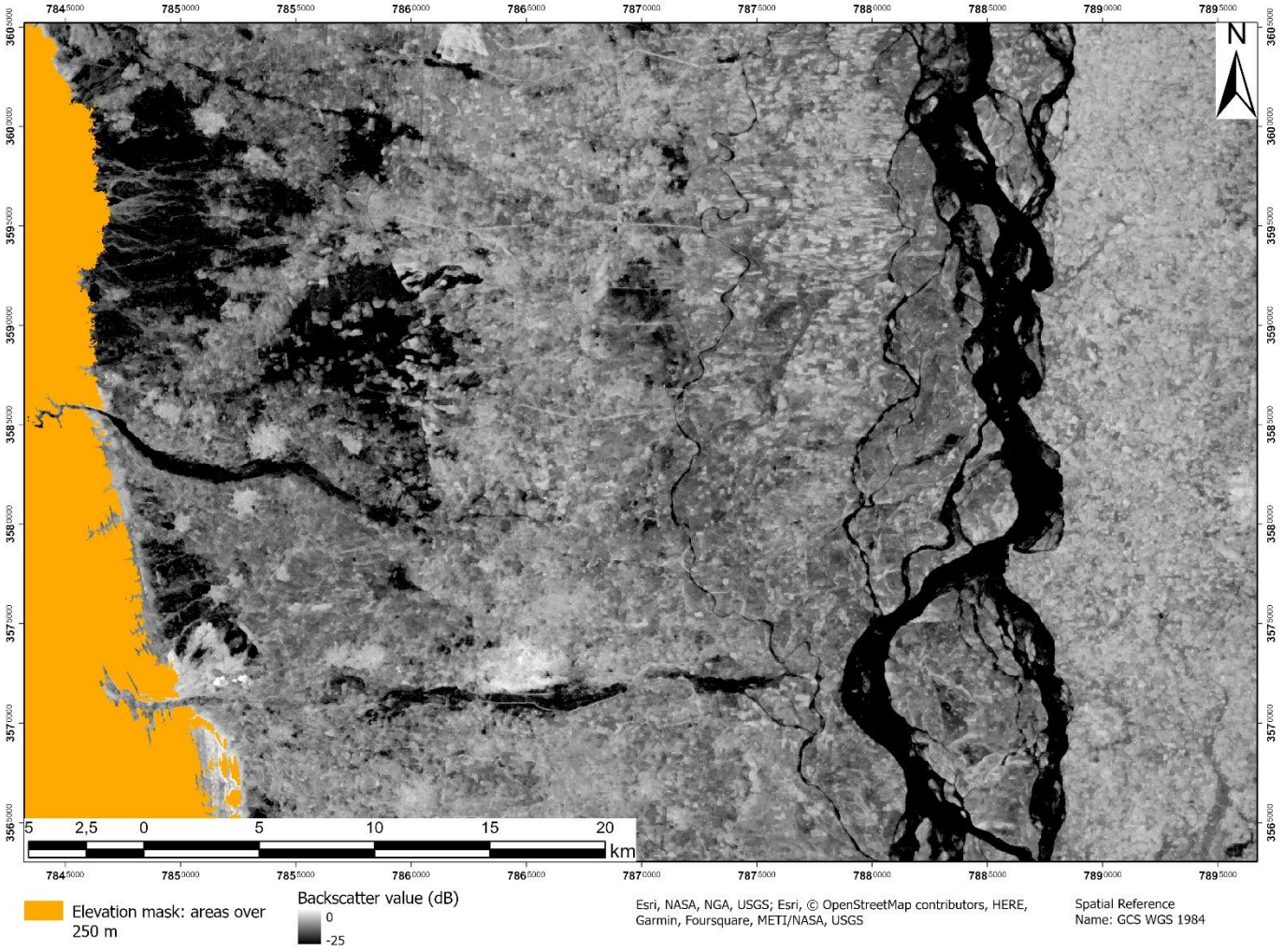


*Appendix 3A: Elevation mask of SA3. Background map is the VH reference image of SA3.*

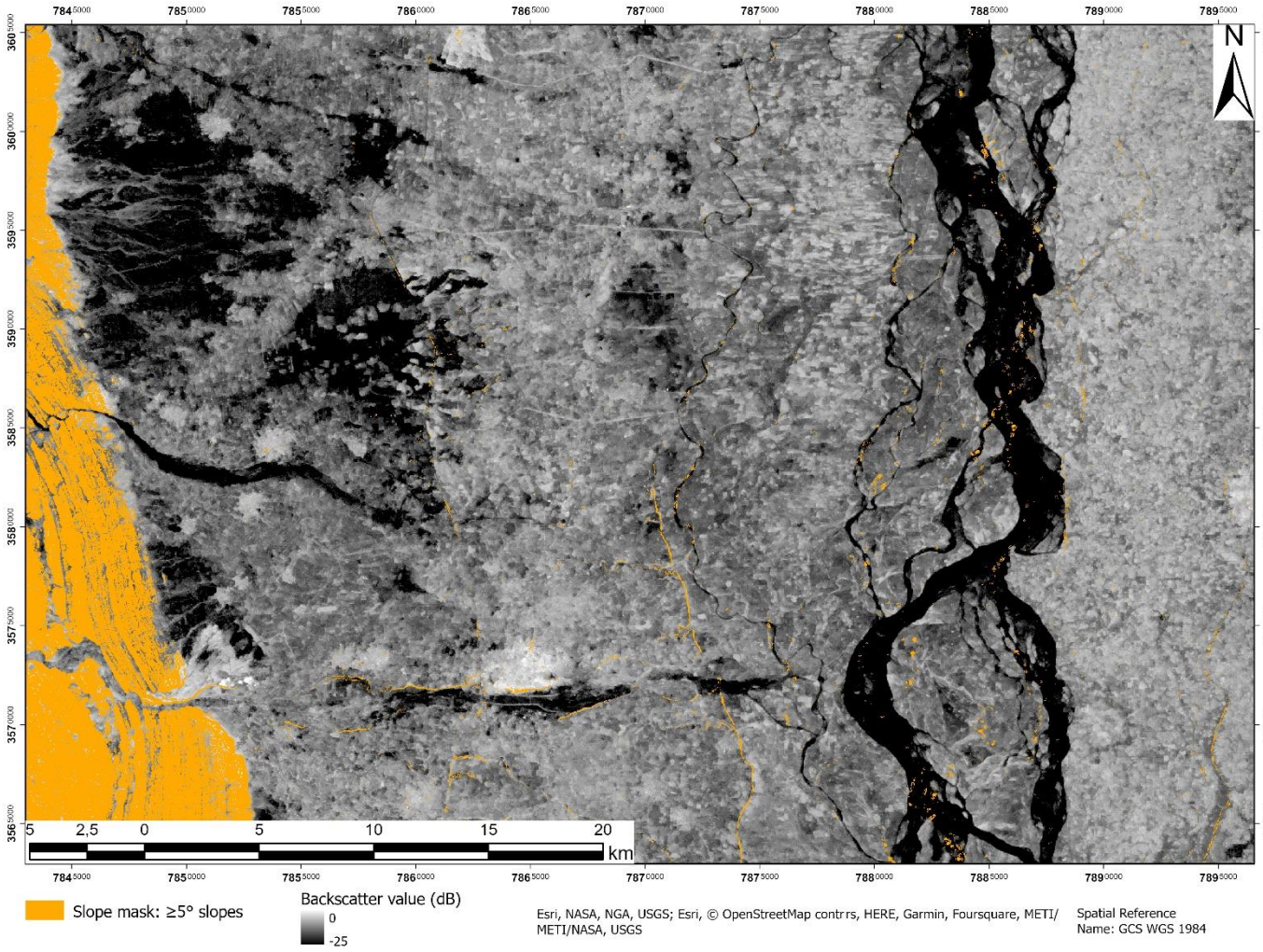


*Appendix 3A: Slope mask of SA3. Background map is the VH reference image of SA3.*

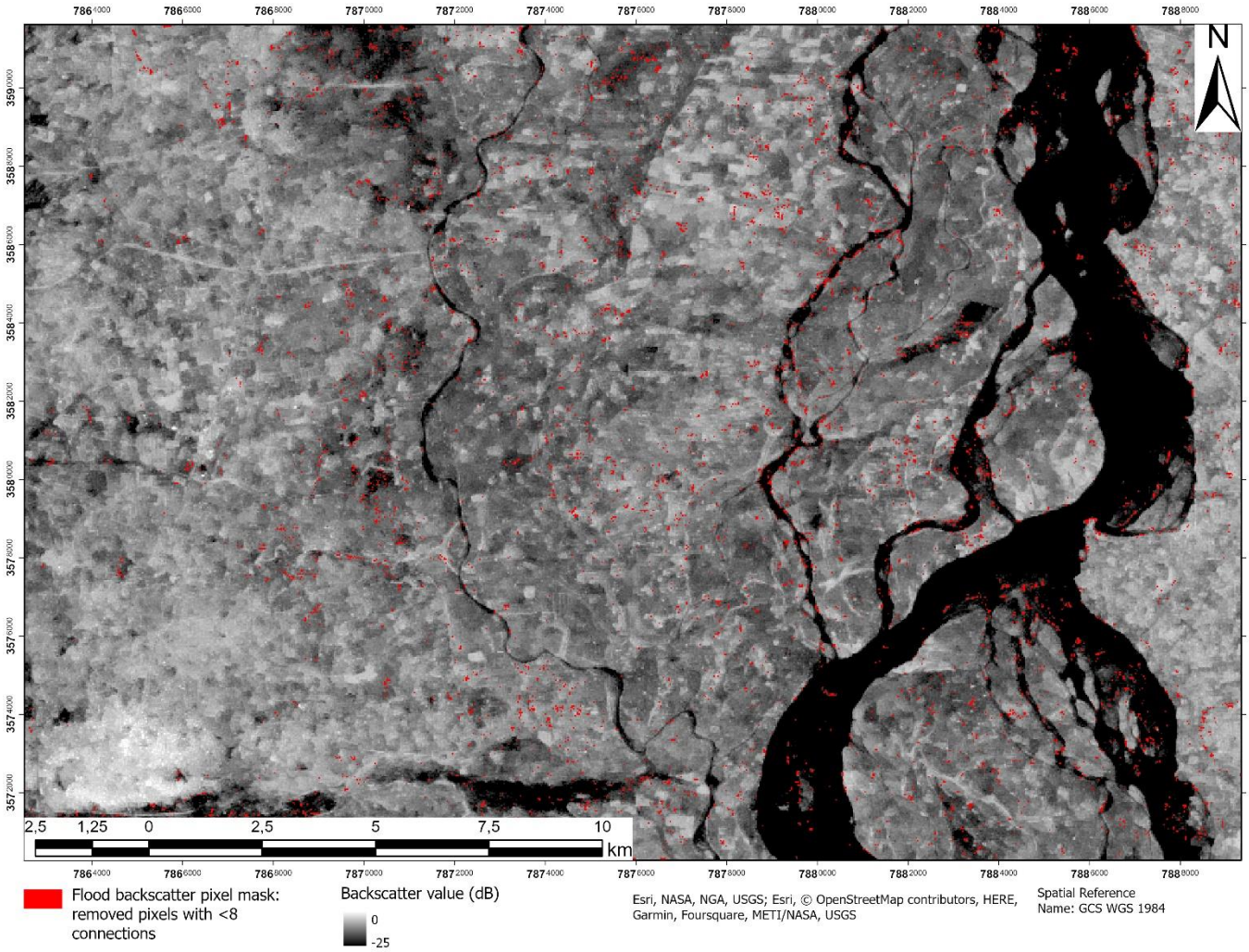


*Appendix 3C: Pixel mask of SA3. Background map is the VH reference image of SA3. Projection is 1:100 000 for a higher exaggeration of pixels.*